NOTE TO USERS

VOLCANO SEISMOLOGY FROM AROUND THE WORLD: CASE STUDIES FROM MOUNT PINATUBO (PHILIPPINES) GALERAS (COLOMBIA), MOUNT WRANGELL AND MOUNT VENIAMINOF (ALASKA)

A

THESIS

Presented to the Faculty

of the University of Alaska Fairbanks

in Partial Fulfillment of the Requirements

for the Degree of

DOCTOR OF PHILOSOPHY

By

John Jairo Sánchez-Aguilar, B.S., M.S.

Fairbanks, Alaska

May 2005

VOLCANO SEISMOLOGY FROM AROUND THE WORLD:

CASE STUDIES FROM MOUNT PINATUBO (PHILIPPINES), GALERAS (COLOMBIA), MOUNT WRANGELL AND MOUNT VENIAMINOF (ALASKA)

By

John Jairo Sánchez-Aguilar

Recommended:

Dr. John Eichelberger

Dr. Douglas Christensen

Dr. Jeffrey T. Freymueller

Dr. John A. Power

Dr. Stephen R. McNutt, Advisory Committee Chair

Dr. Michael Whalen, Chair, Department of Geology and Geophysics

Approved:

Dr. Joan Braddock, Dean, College of Natural Science and Mathematics

Dr. Susan Henrichs, Dean of the Graduate School

February 28, 2005
Date

ABSTRACT

A compilation of research papers in volcano seismology is presented: 1) to study the configuration of magma systems beneath volcanoes, 2) to describe unexpected effects of the shaking from a regional earthquake on volcanic systems, and 3) to integrate seismicity investigations into a conceptual model for the magma system of a volcano. This work was undertaken because much research in volcano seismology is needed to help in hazard assessment. The possible configuration of magma systems beneath Mount Pinatubo, Philippines, and Galeras Volcano, Colombia, is studied with *b*-value mapping. We suggest models for earthquake-volcanoes interactions by studying the declines in local seismicity at Mt. Wrangell and Mt. Veniaminof, Alaska, following the 3 November 2002 Denali Fault Earthquake (DFE). Finally, a model for the magmatic-hydrothermal system beneath Mt. Veniaminof is proposed by deriving a velocity model and relocating the earthquakes, and by studying the temporal changes of frequencies and attenuation (Q) at the source of long-period (LP) events. Results from *b*-value mapping confirm that volcanoes are characterized by localized zones of high *b*-values, and also indicate that the internal structure of volcanoes is variable. Analyses of the background seismicity at Mt. Veniaminof suggest that earthquakes result from locally-induced stresses and that LP events may represent the response of a shallow hydrothermal system to heat input from below. The study of declines in seismicity at Mt. Wrangell and Mt. Veniaminof volcanoes following the DFE indicates that the dynamic shaking from regional shocks can physically damage a volcano and together with the static stress changes can affect the local seismicity for extended periods. We conclude that the use of simple methods allows a better understanding of the seismicity at volcanoes in Alaska, but most importantly in developing countries where the small number of seismograph stations puts challenging limitations for research.

Table of Contents

List of Figures

List of Tables

ACKNOWLEDGEMENTS

A large number of people have contributed in different ways to this work. First I would like to thank my advisor, Stephen R. McNutt, who patiently dedicated countless hours of work during my stay in Alaska. His constant encouragement, criticism, profound understanding of science, and support for his students have made a deep impression on me. I am also very thankful to the other members of my advisory committee: John Eichelberger, Jeff T. Freymueller, John A. Power, and Douglas Christensen, I have learned a great deal from them and they never failed to provide support, encouragement and advice. Max Wyss co-authored one of the papers of this thesis and also provided much helpful advice.

I had the fortune to share experiences with a great group of students at the Geophysical Institute. They were all great peers and helped in keeping an enjoyable study and work atmospheres. Many thanks to the University of Alaska Fairbanks, Geophysical Institute, U.S. Geological Survey, Alaska Volcano Observatory, Alaska Division of Geological and Geophysical Surveys, Alaska Earthquake Information Center, and The International Association of Volcanology and Chemistry of the Earth's Interior. They provided financial and technical support for all the work done during my stay in Alaska

Last, but not least, I thank my loving wife, Indira, and my wonderful son, Mateo. They accompanied me during every single step of the way and deserve all credit for my success. This thesis is dedicated to them and in the memory of my father Rodrigo Sánchez.

Chapter 1. Introduction

1.1. Research in Volcano Seismology

Volcano seismology is a relatively young science that encompasses the study of seismic signals originated at volcanoes and makes use of theory and methods from traditional earthquake seismology to model the likely complex volcanic structure. Progress in volcano seismology in recent decades has been achieved largely because of improvements in instrumentation (e.g. Broadband seismometers, multiparameter stations, permanent GPS stations, borehole instruments) and increase in computing capabilities (e.g. Faster computers with large storage capacity). In many regions of the world, however, it will be difficult to gain access to modern and expensive technology for volcano monitoring and research during many years to come. Thus we should think about simple techniques to carry out research using data acquired with older instrumentation (e.g. Catalogs of located earthquakes, listings of routine event counts, waveforms from short-period stations). In this thesis I would like to argue that if a rigorous statistical analysis is provided, cutting-edge research is still possible in areas where logistics place challenging limitations to science.

This thesis presents various papers in volcano seismology that investigate the internal structure of volcanoes and the effects of earthquakes-volcanoes interactions. The thesis is divided into eight chapters: general introduction, six papers, and general conclusions. At the time of this writing (December 2004) two of the chapters are already published (chapters 2 and 4), one is in press (chapter 5) and the remainder (chapters 3, 6 and 7) are either submitted or ready for submission. Chapters 2 and 3 present the mapping of the relative distribution of sizes of earthquakes (*b*-value) at Mount Pinatubo, Philippines, and Galeras Volcano, Colombia. Chapters 4 and 5 document the

unprecedented observation of drops in seismicity at Mount Wrangell and Mount Veniaminof Volcanoes, Alaska, following the 3 November 2002 Mw 7.9 Denali Fault Earthquake. Chapter 5 investigates the internal structure of Mount Veniaminof through the modeling of velocity distribution, relocation of volcano-tectonic earthquakes (VT) and spatial changes in stress. In chapter 6 we look at the volcano from the point of view of the complex frequencies of long-period (LP) events.

1.2. Overview of the Chapters

Chapter 2 presents the results of *b*-value mapping at Mount Pinatubo, Philippines, using earthquakes recorded following the 15 June 1991 eruption. Following the work by former researchers (Mori et al., 1996; Wiemer and McNutt, 1997; Wiemer et al., 1998; Power et al., 1998; Wyss et al., 2001) we confirmed the presence of two distinct high *b*-value regions beneath Mount Pinatubo: A shallow anomaly that may be related to increased pore pressure, as well as high material heterogeneity, and a deeper anomaly possibly related to stresses and thermal effects surrounding the magma reservoir.

Chapter 3 will give some more insight into the possible configuration of the plumbing system beneath volcanoes, this time by mapping the *b*-values beneath and around Galeras Volcano, Colombia, using earthquakes located during a background-like period of VT seismicity between mid 1995 and mid 2002. Just as Mount Pinatubo, Galeras is an active stratovolcano. They both also share a similar configuration and characteristics in their seismograph networks. Surprisingly, we found that at Galeras the dominant feature is a high *b*-value anomaly, vertically elongated and located beneath the active cone. This observation leads to the suggestion that a region adjacent to a conduit or the

remnants of a volume of unextruded magma may be illuminated with this technique.

Chapter 4 takes the reader into the realm of interactions between large tectonic earthquakes and volcanoes. Here we document for the first time the intermediate-term declines of volcanic seismicity at Mount Wrangell and Mount Veniaminof, following the Denali Fault Earthquake (DFE) on November 3, 2002. We observed that seismicity at Mount Wrangell, the closest volcano to the epicenter, was anomalously low during at least five months following the DFE, whereas seismicity at Mount Veniaminof, distant 1400 km from the epicenter, seismicity decreased for a shorter period of two weeks after the DFE. These two Alaskan volcanoes with ongoing high seismicity rates at the time of the DFE are similar in that most seismicity is of the LP type, they are both located in a perpendicular direction in relation to the DFE rupture, and their responses to the DFE were relatively long-lasting, all of which are in strong contrast to well documented cases of triggering of seismicity elsewhere in the United States. We then suggest that fundamentally different mechanisms act to modify seismicity at volcanoes.

In Chapter 5 we focus on Mount Wrangell and take a closer look at the drop in seismicity following the DFE. We make use of more data and various sources of information to estimate the seismicity rates and apply rigorous statistics to find the negative change in seismicity and to explain some interesting features of the data, such as the position of the strongest rate change in time, and a possible cumulative or combined effect of the stress changes produced by the DFE sequence, which includes the 23 October Mw 6.7 Nenana Mountain Earthquake. Perhaps the most interesting result of this analysis is the tantalizing observation that the seismicity rates at Mount Wrangell did not fully recover to

pre-DFE values, implying that the strong shaking from the DFE may have physically damaged the volcano.

Chapter 6 presents a study of the volcano-tectonic earthquakes at Mount Veniaminof. Based on preliminary locations and a set of initial velocity models (Ellsworth, 1977., Roecker, 1981; Kradolfer, 1989; Kissling, 1995) we devise a minimum 1D velocity model with station corrections to relocate the earthquakes, compute preliminary fault-plane solutions and study the state of stress around the volcano. By using a simple method (Wadati, 1933; Riznichenko, 1958) we also constrain the focal depths of earthquakes to within a few kilometers, or less, and find possible variations in the ratio of P to S-wave velocity (Vp/Vs). All of our observations support the conclusions that the magmatic system of Mount Veniaminof strongly influences the distribution of seismicity, and that the caldera region exhibits variable behavior.

In Chapter 7 we look at the most prominent seismic signals recorded at Mount Veniaminof: LP events. Applying the Sompi method, a high-resolution method for spectral analysis (Kumazawa et al., 1990; Hori, et al., 1989; Kumagai and Chouet, 1999) we study the complex frequencies of LP events during two enhanced periods of seismicity between September 2002 and August 2004. We found that during late 2002-early 2003 the values of frequency and Q (a measure of attenuation at the source of the LP events) are lower than during February-August 2004 and that this result correlates well with changes in surface activity at the volcano. During the early study period ground reports and Satellite observations are mostly consistent with an active hydrothermal system (more water vapor) whereas during the later period a more phreatomagmatic phase is observed, evidenced by frequent ash bursts through the active cone. We conclude that the study of complex frequencies of

LP events may be used as a good indicator of changes in the volcano's behavior and help in the assessment of hazard from eruptions.

The final chapter 8 presents the conclusions to summarize the relevant observations and to make suggestions regarding future research.

1.3. References

Ellsworth, W. L., 1977. Three-dimensional structure of the crust and mantle beneath the island of Hawaii. Ph.D. thesis, Mass. Inst. of Technol., Cambridge.

Hori, S. Y. Fukao, M. Kumazawa, M. Furumoto, A. Yamamoto (1989) A new method of spectral analysis and its application to the earth's free oscillations: the ``Sompi'' method, J. Geophys. Res., 94, 7535-7553.

Kissling, E., 1988. Geotomography with local earthquake data. Rev. Geophys. 26, 659-698.

Kradolfer, U., 1989. Seismische tomographie in der Schweiz mittels lokaler Erdbeben. Ph.D. thesis, Eidg. Techn. Hochschule (ETH), Zürich.

Kumagai, H. and B.A. Chouet (1999). The complex frequencies of long-period seismic events as probes of fluid composition beneath volcanoes, Geophys. J. Int., 138, F7-F12.

Kumazawa, M., Y. Imanishi, Y. Fukao, M. Furumoto, and A. Yamamoto (1990) A theory of spectral analysis based on the characteristic property of a linear dynamic system, Geophys. J. Int., 101, 613-630.

Mori, J., D. Eberhart-Phillips, and D. H. Harlow (1996). Three-dimensional velocity structure at Mount Pinatubo: resolving magma bodies and earthquake hypocenters, in Fire and Mud: Eruptions and Lahars of Mount Pinatubo, Philippines, C. G. Newhall and R. S. Punongbayan (Editors), PHIVOLCS and University of Washington, Seattle, 371–382.

Power, J. A., M. Wyss, and J. L. Latchman (1998). Spatial variations in the frequency–magnitude distribution of earthquakes at Soufriere Hills volcano, Montserrat, West Indies, Geophys. Res. Lett. 25, 3653–3656.

Riznichenko, Y., 1958. The mass determination of the coordinates of local earthquakes and of the velocities of seismic waves in the source areas. Izv. Geophys. Ser. 425-437.

Roecker, S.W., 1981. Seismicity and tectonics of the Pamir-Hindu Kush region in central Asia. Ph.D. thesis, Mass. Inst. of Technol. Cambridge.

Wadati, K., Sagisaka, K., Masuda, K., 1933. On the travel time of earthquake waves (part II). Geophys. Mag. 7, 101-111.

Wiemer, S., and S. R. McNutt (1997). Variations in the frequency–magnitude distribution with depth in two volcanic areas: Mount St. Helens, Washington, and Mount Spurr, Alaska, Geophys. Res. Lett. 24, 189–192.

Wiemer, S., S. R. McNutt, and M. Wyss (1998). Temporal and three-dimensional spatial analysis of the frequency–magnitude distribution near Long Valley caldera, California, Geophys. J. Int. 134, 409–421.

Wyss, M., F. Klein, K. Nagamine, and S. Wiemer (2001). Anomalously high b-values in the south flank of Kilauea Volcano, Hawaii: evidence for the distribution of magma below Kilauea's east rift zone, J. Volcanol. Geotherm. Res. 106, 23–37.

Chapter 2. Spatial Variations in the Frequency-Magnitude Distribution of Earthquakes at Mount Pinatubo Volcano[1]

2.1. Abstract

The frequency–magnitude distribution of earthquakes measured by the *b*-value is mapped in two and three dimensions at Mount Pinatubo, Philippines, to a depth of 14 km below the summit. We analyzed 1406 well-located earthquakes with magnitudes $M_D \geq 0.73$, recorded from late June through August 1991, using the maximum likelihood method. We found that *b*-values are higher than normal ($b = 1.0$) and range between $b = 1.0$ and $b = 1.8$. The computed *b*-values are lower in the areas adjacent to and west-southwest of the vent, whereas two prominent regions of anomalously high *b*-values ($b \sim 1.7$) are resolved, one located 2 km northeast of the vent between 0 and 4 km depth and a second located 5 km southeast of the vent below 8 km depth. The statistical differences between selected regions of low and high *b*-values are established at the 99% confidence level. The high *b*-value anomalies are spatially well correlated with low-velocity anomalies derived from earlier P-wave travel-time tomography studies. Our dataset was not suitable for analyzing changes in *b*-values as a function of time. We infer that the high *b*-value anomalies around Mount Pinatubo are regions of increased crack density, and/or high pore pressure, related to the presence of nearby magma bodies.

[1] Sánchez, J.J., S. R. McNutt, J. A. Power, and M. Wyss (2004): Spatial Variations in the Frequency-Magnitude Distribution of Earthquakes at Mount Pinatubo Volcano, *Bull. Seism. Soc. Am.*, Vol 94, No. 2, pp. 430–438.

2.2. Introduction

On 15 June 1991, Mount Pinatubo produced the world's largest eruption in more than half a century and probably the second largest of the century, devastating more than 400 km^2 in Central Luzon, Philippines. It's roughly 5 km^3 of erupted magma is an order of magnitude greater than the volume of magma erupted in 1980 from Mount St. Helens. Even more remarkable than the volume and area of impact is that this was the first eruption of this size to be monitored in detail (Newhall and Punongbayan, 1996).

Although many seismological studies have been carried out with data recorded before and after the Pinatubo eruptions, the study of *b*-values has not been attempted previously. Many other volcanoes around the world have been studied using *b*-value mapping (e.g., Mount St. Helens and Mount Spurr [Wiemer and McNutt, 1997]; Long Valley caldera [Wiemer et al., 1998]; Montserrat [Power et al., 1998]; and Kilauea [Wyss et al., 2001]). In these studies, small volumes of anomalously high *b*-values were used to identify magma bodies. The large number of well-located earthquakes during the pre- and post-eruption periods at Mount Pinatubo offers the possibility of mapping *b* in two and three dimensions at this important volcano.

The size distribution of earthquakes in a region can be described by a power-law relationship, first recognized in Japan by Ishimoto and Iida (1939) and later in California by Gutenberg and Richter (1944), given as

$$log\ N = a - bM, \qquad (1)$$

where N is the cumulative number of earthquakes with magnitude $\geq M$ and a and b are constants. The parameter b is the slope of the best-fit line to the

frequency–magnitude distribution (FMD); *b* is inversely proportional to the average fault length that ruptures in an earthquake (equation 2, Aki, 1965). Values of *b* are in general close to 1 in the Earth's crust (Morgan et al., 1988; Frolich and Davis, 1993), but in volcanic regions *b* is often found to be closer to 2 (Wiemer and McNutt, 1997; Wyss et al., 2001). High *b*-values beneath volcanoes have been attributed to greater-than-normal heterogeneity (Mogi, 1962), decrease in either effective stress (high pore pressures) (Wyss, 1973) or applied stress (Scholz, 1968), or alternatively, to elevated thermal gradients (Warren and Latham, 1970).

In this work, we study spatial differences in *b*-values at Mount Pinatubo volcano, Philippines (15.13° N, 120.35° E, pre-eruption summit elevation 1745 m) using earthquakes occurring between May and August 1991 (Fig. 2.1). Most of the earthquakes before the eruption occurred in two clusters (all depths in this article are referenced to sea level, with negative depths referring to elevation above sea level), one located beneath the vent, with depths between -1.7 and 2 km, and a second cluster located 5 km northwest of the vent with depths between 0 and 4 km (Harlow et al., 1996). After the 15 June 1991 cataclysmic eruption, earthquakes occurred in a greater volume, with seismicity located mostly in four clusters: the first beneath the vent with depths between -1.5 and 3 km, a second group 5 km northwest of the vent at depths between 3 and 18 km, a third group north of the vent with depths between -1 and 6 km, and a fourth cluster east of the vent at depths between 8 and 15 km (Mori et al., 1996a, b).

The eruptions, which were apparently triggered by injection of basaltic magma into a reservoir of dacitic magma (Pallister et al., 1996), evolved in stages beginning with felt earthquakes and phreatic explosions and culminating in a 9-hr climactic eruption (Wolfe and Hoblitt, 1996).

Because anomalously high *b*-values near conduits or magma chambers can result from higher-than-normal material heterogeneity, from decreased effective stress (high pore pressure) or applied stresses, and from elevated thermal gradients, we expect to find more small earthquakes, relative to large ones, near active volcanoes. We use a catalog of relocated volcano-tectonic earthquakes (Mori et al., 1996b) beneath Mount Pinatubo to find the relative distribution of earthquake sizes and to map the *b*-value in two and three dimensions to find the areas in which the production of small shocks is higher or lower than average.

2.3. Data

From 14 May through 11 June 1991, seismic activity at Mount Pinatubo was monitored with a seven-station, nine-component seismograph network with signals telemetered to the observatory at Clark Air Force Base (Lockhart et al., 1996). All but one of the seven stations were destroyed by the eruptions, and a second network of seven stations was installed after 15 June, with only two station sites common to both periods: BUG and CAB (Fig. 2.1). Because it is known that changes in the technology and configuration of networks can introduce artificial changes in earthquake reporting (e.g., Wyss, 1991), we believe that at Mount Pinatubo the damage to the pre-eruption stations and the change in configuration of the network makes it difficult to use the full dataset, with pre-eruption and post-eruption earthquakes, in a temporal or spatial analysis of *b*-values. Therefore, we confine our study to the higher quality data recorded after 29 June 1991.

Using a three-dimensional velocity structure derived from P-wave tomography, Mori et al. (1996a) relocated all earthquakes used in this study.

Magnitudes were calculated using coda measurements (M_D, duration magnitude) and the standard values established for California.

The catalog originally contained 2851 relocated earthquakes that covered the period 7 May to 19 August 1991. The estimated location accuracies of these earthquakes are 0.9 and 1.9 km in the horizontal and vertical directions, respectively. By analyzing a plot of cumulative number of events versus time, we discovered that before the 15 June eruption the rate of located earthquakes was not constant. We suspect that this may be an artifact caused by changes or damage to the seismograph network. Several problems were encountered during the operation of the pre-eruption stations. Also, during times of increased volcanic activity, especially the last few days before 15 June, the utility of the data was reduced because high signal amplitudes made the identification of small earthquakes impossible (Lockhart et al., 1996).

After the eruptions, the rate of located earthquakes was approximately constant with time, which may suggest more homogeneity in the reporting from 29 June onward, when the new seismograph network was fully operational. Figure 2.2a shows the cumulative number of events versus time. The histogram of magnitudes (upper part of inset in Fig. 2.2a) shows no bimodal distributions, which are sometimes caused by families of earthquakes. Also, the data are not contaminated by quarry blasts. A histogram of the number of events located per hour of the day (lower part of inset in Fig. 2.2a) shows that there are no excess events during daytime hours, as would be expected for blasts (e.g., Wiemer and Wyss, 2002).

For all earthquake catalogs, there is a minimum magnitude below which there is little chance of complete detection. This is called the magnitude of completeness (M_c). We analyzed M_c for the Mount Pinatubo catalog in the

following fashion. First we plotted M_c as a function of time (Fig. 2.2b) using a moving window of n = 200 events and stepping 5 events each time. We see that M_c shows some variation but in general is in the range 0.6–0.9. Also, from the maximum in the number of earthquakes in the magnitude histogram plot (upper part of inset in Fig. 2.2a); we see that the M_c is close to 0.7. An automatic estimate using the computer program ZMAP (Wiemer, 2001) yields M_c = 0.73 for the whole catalog (inset in Fig. 2.2b). Before the eruption, M_c appears to be constant, but the amount of data for this period is fairly small and does not allow us to draw conclusions regarding stability of M_c with time. We prefer to restrict our attention to spatial variations of *b* by checking for uniformity of M_c in space. Analysis of *b* as a function of time requires a higher quality catalog and also a larger number of events. Some preliminary tests of possible variations in *b* over time were performed, but such variations were unresolvable because of insufficient numbers of earthquakes for differential *b* mapping. We therefore focus solely on spatial variations. By using a catalog of 1406 earthquakes with $M_D \geq 0.73$ recorded after 29 June, we avoid possible artifacts in earthquake reporting introduced by the different network geometries before and after the eruption and ensure that most parts of the catalog are complete, thus adding to the robustness of our data.

2.4. Method

To compute b-values, we used the maximum likelihood (ML) method of Aki (1965),

$$b = 2.3/(M_{mean} - M_o) \qquad (2)$$

where M_{mean} is the mean magnitude and $M_o = M_c$ - 0.05 (0.05 is one-half the magnitude bin unit of 0.1). Because M_{mean} and *b* are inversely proportional,

whenever we measure b, we are also measuring M_{mean}. One advantage in expressing the results in terms of b is that they can be compared with results from other areas, whereas the particular value of M_{mean} depends on M_o.

To map b, we used the method by Wiemer and Benoit (1996), Wyss et al. (1997), and Wiemer et al. (1998). The b-values were computed on two- and three-dimensional grids with nodal points separated 1 km horizontally and 2 km vertically, using a fixed number of earthquakes (n_i = 100) without limiting the size of the sampling volumes. The radii of the sample volumes varied between 1 and 4 km. In cross sections, the nearest n_i earthquakes were selected according to their distance in the projections of hypocenters onto a vertical plane, with sampling volumes that have the shape of cylinders with horizontal axes. In three-dimensional grids, the sampling volumes are spheres. To verify that the results are independent of the method used, we mapped b-values calculated using both the ML and the weighted least-squares (WLS) methods. We note that the spatial patterns observed were the same using the ML and WLS methods. The b-value maps shown in Figures 2.4a and 2.5 are those calculated using the ML method.

2.5. Results

The average b-value of earthquakes ($M_D \geq 0.73$) between 29 June and 19 August 1991 starts at b = 1.2 at shallow depths, increases to b = 1.5 at 2 km depth, reaches a low value of b = 1.2 at ~ 6 km depth, and increases again to ~b = 1.4 between 10 and 12 km below the summit (Fig. 2.3). In east–west and north–south cross sections through the vent (Fig. 2.4), low b-values (blue regions) are common. Two high b-value regions stand out: one northeast of the vent, extending from 0 to 4 km depth, and the other southeast of the vent, between 8 and 12 km depth.

The same spatial patterns were observed by mapping *b* under three different scenarios: (1) by assuming that M_c is constant and equal to $M_{min} = 0.73$; (2) by assuming that M_c varies spatially, computing it locally at each grid node; and (3) by keeping a constant sampling radius, *R*, of 2 km, allowing the number of events to vary. In scenario 2, we constructed east–west and north–south cross sections showing the variation of M_c and observed that most areas beneath the volcano showed M_c in the range 0.8–0.9. Because of this spatial variation of M_c, we also performed our mapping using higher values, in the range 0.73–0.9, and the results did not vary greatly. Thus we chose to use the value of $M_c \sim 0.73$ that maximizes the number of usable earthquakes, while still preserving the spatial pattern of observed *b*-value anomalies.

Figure 2.4b shows the FMD for samples selected from two contrasting regions in each cross section. The *p*-values, the probabilities that both samples are drawn from the same population (Utsu, 1992), indicate there is little chance that they are the same ($p << 0.01$). We note that the assumption underlying Utsu's test is that the samples are drawn randomly from a given population. This is not the case here, where we intentionally select samples from two contrasting regions. This is done to show that the two regions chosen have different FMDs. To make the test as fair as possible, we compared a region of anomalously high *b*-value with several surrounding regions of low *b*-values, and the results did not vary. In the three-dimensional map of *b*-values beneath Mount Pinatubo (Fig. 2.5a), the two high *b*-value anomalies detected previously by linearly computing *b*-values as a function of depth (Fig. 2.3), and by two-dimensional mapping (Fig. 2.4a), are found again.

We also performed the same analysis as described earlier, using a catalog of 3000 non-relocated earthquakes (uncertainties in locations on the order of 8 km). The spatial pattern of *b*-value anomalies was the same. This dataset

included earthquakes recorded before and after the eruptions. The mixing of two periods with non uniform reporting of earthquakes did not change the results. This indicates that the signal we attempt to map is robust.

2.6. Discussion

The *b*-values calculated in this study are on average higher than in many other areas, where *b* has been found to range between 0.5 and 1.5. Because the absolute value of *b* depends on the magnitude scale used (Zúñiga and Wyss, 2001), we regard the *b*-values found here as relative values and use them only for comparison purposes at Mount Pinatubo.

The contrasts between *b*-values in different volumes we documented are real and robust, we believe, for the following reasons. The statistical probabilities that samples taken from contrasting regions come from the same population are less than 0.1% in all cases, based on Utsu's (1992) test. The anomalies are revealed independent of the method for the *b* value computation, spatial estimation of M_c, and sampling of events. Also, the accuracy of earthquake locations does not influence the result.

Wiemer (1996) proposed that at volcanoes, anomalously high *b*-value pockets exist embedded in an otherwise normal crust. High *b*-value anomalies have been reported at numerous other volcanoes: Mount St. Helens, Washington, and Mount Spurr, Alaska (Wiemer and McNutt, 1997); off-Ito, Japan (Wyss *et al.*, 1997); Long Valley caldera, California (Wiemer *et al.*, 1998); Soufriere Hills, Montserrat (Power *et al.*, 1998); Katmai area, Alaska (Jolly and McNutt, 1999); Mount Etna, Italy (Murru *et al.*, 1999); and Kilauea, Hawaii (Wyss *et al.*, 2001). Evidently, high *b*-value anomalies are persistent features regardless of the type of volcano, configuration of the seismograph network, or

quality of the dataset. The pattern of the anomalies varies from place to place, however (Wyss *et al.*, 1997).

Several factors can account for high *b*-value anomalies: low effective stress (high pore pressures) (Wyss, 1973), low applied stress (Scholz, 1968), high material heterogeneity (Mogi, 1962), and high thermal gradients (Warren and Latham, 1970). Low effective stresses can be obtained when the pore pressure in the host rock increases, for example because of interaction of magma and groundwater (Wiemer and McNutt, 1997). Also, if an aquifer adjacent to an intrusion is compressed as a result of an intrusion, its pore pressure will rise and may produce hydrofracturing (e.g., Newhall *et al.*, 2001).

High material heterogeneity (many cracks with different orientations) is likely at volcanoes not only because of their structure, which is formed by layers of ash and lava, dikes, and sills, but also because many processes take place. For example, pressurization by a magma intrusion, and the buoyancy caused by exolution and expansion of volatiles, can cause stresses around the tip of intruding bodies and thus new cracking. Also the disruption of host rocks by repeated intrusions into reservoirs (Wyss *et al.*, 2001) and hydrofracturing can also lead to new cracking. Yet another cause of material heterogeneity at volcanoes can be the fracturing of a semibrittle crystalline mush. These bodies, if strained rapidly enough, will fracture, similar to the carapace of a cooling lava dome. These magma fracturing earthquakes tend to be small (C. Newhall, personal comm., 2003). In the case of laboratory tests, cracking can be caused by the thermal stresses generated by high thermal gradients (Warren and Latham, 1970). At volcanoes, it is not possible, with the information we have, to identify the factors that cause the observed *b*-value differences.

From our results of *b*-value mapping in two (Fig. 2.4a) and three dimensions (Fig. 2.5a, b), we see that areas of relatively higher *b*-values ($b \sim 1.7$) occur northeast of the vent at shallow levels (0–4 km) and southeast of the vent, below 8 km depth. These two features are robust; they also appeared when we plotted the average *b*-value versus depth (Fig. 2.3), a linear approach that smoothes variations. We therefore feel that the existence of the anomalies and their positions are well established.

The shallow *b*-value anomaly (Figs. 2.3, 2.4a, and 2.5a) may indicate that the upper portion of Mount Pinatubo's plumbing system has (1) cracks that are smaller than those in the surrounding medium, (2) higher-than-average pore pressures, or (3) weaker-than-average, hot rock. Geological and petrological evidence indicates that many eruptions similar to the 1991 activity have taken place over the last 35,000 yr (Newhall *et al.*, 1996; Pallister *et al.*, 1996), suggesting repeated use of the shallow plumbing system and repeated caldera collapse. In the upper parts of the volcanic system, processes such as vesiculation and fragmentation of ascending magmas occur (e.g., Eichelberger, 1995). It has been suggested (Wiemer and McNutt, 1997) that exsolution of gas and vesiculation may play a role in stress-induced fracturing. Pre-eruption magmas at Mount Pinatubo are thought to have been volatile rich with 5.1% to 6.4% weight H_2O (Rutherford and Devine, 1996), suggesting a vesiculation depth of about 6 km. At Mount Spurr and Mount St. Helens, where 4% weight H2O were observed, the *b*-value anomalies coincided also with the inferred vesiculation depth (Wiemer and McNutt, 1997). However, it seems that there is no single depth at which gas can suddenly become a major contributor to stress-induced rock fracturing; rather, this process develops gradually. Our mapping shows that a shallow *b*-value anomaly at Mount Pinatubo only appears to extend to 4 km. This suggests that vesiculation alone is not the cause of the extensive cracking.

Another potential contribution to the high *b*-values found in the upper 4 km beneath Mount Pinatubo is increased pore pressure arising from magma–groundwater interaction. The associated reduction of normal stress would permit slip on faults and fractures, generating relatively more small earthquakes. It is likely that a combination of vesiculation–fragmentation effects and elevated pore pressure in the vicinity of the conduit may contribute to the smaller average size of earthquakes in the shallow anomaly.

The two-dimensional mapping shows that low *b*-values ($b \sim 1$) are common west of the vent, to a depth of 14 km. Bautista *et al.* (1996) suggested that the earthquakes located northwest of Mount Pinatubo occurred as a result of left-lateral movement along the Maraunot fault (Newhall *et al.*, 1996). The normal *b*-values along this fault imply that the distribution of crack lengths activated in earthquakes conforms to that generally found along developed faults and suggest that no magma exists in the vicinity. Because these earthquakes occurred near the time of the 15 June eruption, it seems most likely that their occurrence was due to adjustment of stresses caused by intrusion at Mount Pinatubo.

At levels below 8 km, high material heterogeneity induced by a nearby magma reservoir may produce higher-than-normal *b*-values. Wiemer and McNutt (1997) suggested that such material heterogeneity may arise from a combination of thermal cracking and high stresses. This theory has been supported by results of laboratory experiments by Warren and Latham (1970), who explored the effects of temperature gradients ranging from 15°C/cm to 100°C/cm on different materials. Their results showed *b*-values that are larger than those typically found in studies of fracturing by mechanically induced stresses.

Therefore, we interpret the high *b*-value anomaly below 8 km depth to indicate the presence of a magma reservoir. Mori *et al.* (1996a) used seismic tomography to infer the location of *P*-wave low-velocity anomalies between 8 and 14 km depth beneath Mount Pinatubo and interpreted them as expressions of a magma body. We demonstrate good spatial correlation between the *b*-value anomaly and the volumes of low *P*-wave velocities; the depth ranges coincide and the *b*-value anomaly is located adjacent to the velocity anomaly. We would expect a *b*-value anomaly to be found adjacent to the magma body, because no earthquakes occur within it. Based on petrological studies, Rutherford and Devine (1996) concluded that the storage region for the dacite pre-eruptive magma of the 15 June 1991 eruption was located at depths between 7 and 11 km, also in good agreement with our results.

Changes in *b*-values with time can be difficult to detect. Variations over time in instrumentation, earthquake location procedures, or changing analysis staff can introduce changes in the reporting of earthquakes that influence the *b*-value (e.g., Zuniga and Wyss, 1995). By constructing differential *b*-value maps for different periods between May and August 1991, including a comparison of post-eruption and pre-eruption periods, we did not find significant changes of *b*-values as a function of time. Therefore, we conclude that the first-order variations in *b*-value in this dataset occur predominantly as a function of space.

2.7. Conclusions

Mapping the *b*-value constrains the distribution of volumes beneath Mount Pinatubo in which there is higher production of small earthquakes relative to large ones. The high *b*-value anomaly found in the upper 4 km beneath the volcano may represent a volume in which there exists a combination of

increased pore pressure caused by magma–water interaction, as well as high material heterogeneity arising from a combination of processes. These may include vesiculation and fragmentation of ascending magmas, repeated intrusions, and caldera collapses that have fractured the rocks to a higher degree than normal. The observed *b*-value anomaly below 8 km depth may be the expression of high material heterogeneity caused by stresses and thermal effects on the surroundings of the magma reservoir. Alternatively, the lack of large earthquakes may suggest the presence of hot, semibrittle rock.

There is good spatial correlation between the *b*-value anomalies found in our mapping and the zones of low *P*-wave velocities found in earlier tomography studies (Mori *et al.*, 1996a); the depth ranges coincide, and the *b*-value anomalies are adjacent to the regions of low *P*-wave velocity. Also, evidence from petrological studies (Rutherford and Devine, 1996) indicates that the storage region for the dacite pre-eruptive magma of the 15 June 1991 eruption was located at depths of 7–11 km, in good agreement with our results. The *b*-value anomalies thus provide additional constraints on the location and configuration of magma bodies and the adjacent regions of the crust.

2.8. Acknowledgements

We wish to thank J. Mori for providing the relocated catalog of earthquakes used in this study and S. Wiemer for the computer program ZMAP. T. Murray provided help with the software used to visualize the waveforms and repicking of earthquakes during an early stage of the work. This article benefited greatly from the comments and thorough reviews of W. Marzocchi, A. Hurst, C. Newhall, S. Moran, and C. Rowe. This work was supported by the Alaska Volcano Observatory and the U.S. Geological Survey (USGS), as part of their Volcano Hazards Program, and by additional funds by the State of Alaska.

2.9. Figures

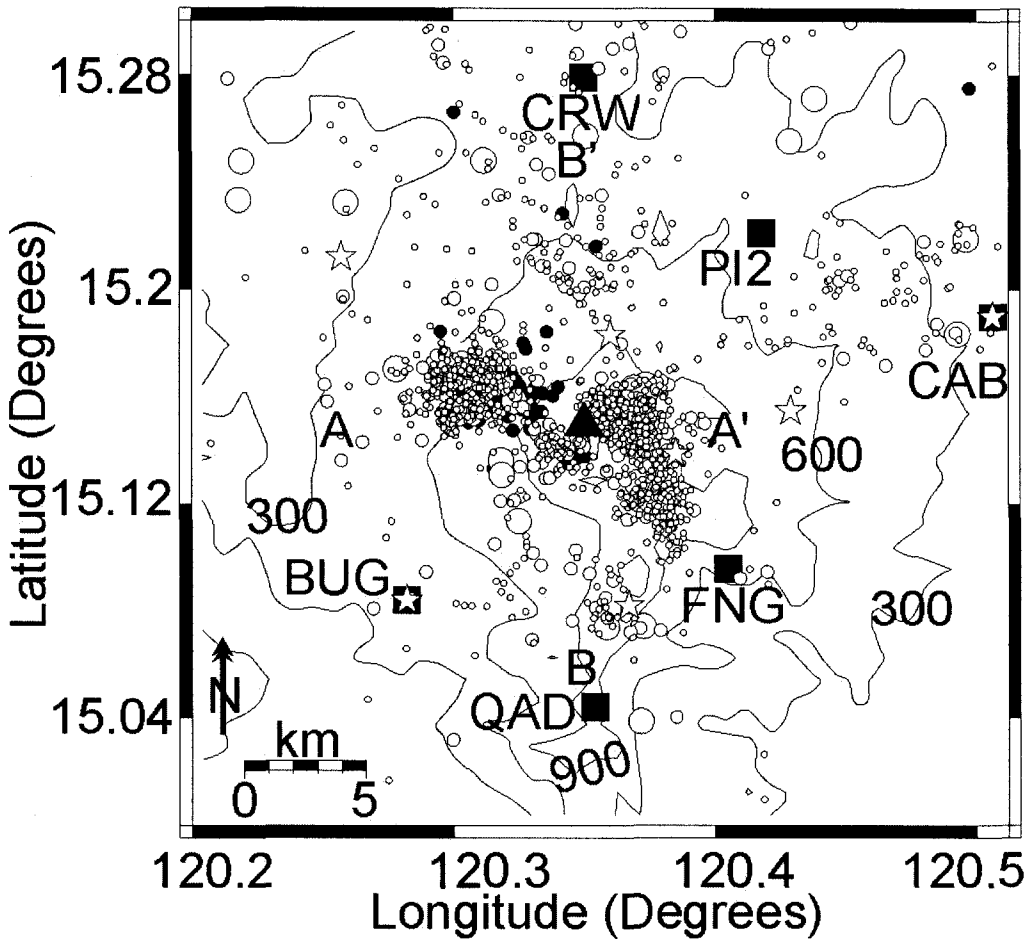

Figure 2.1. Map of Mount Pinatubo. Contours represent meters above sea level; contour interval is 300 m. Black triangle at the center marks the location of the vent. Stars mark the locations of the pre-15 June 1991 seismograph stations. Solid black circles show epicenters of pre-eruption earthquakes. Solid black squares mark the locations of the post-15 June 1991 seismograph stations. White circles show epicenters of post-eruption $M_D \geq 0.73$ earthquakes used for the *b*-value mapping. Magnitude is proportional to symbol size. A-A and B-B indicate the locations of cross sections shown in Figure 2.4.

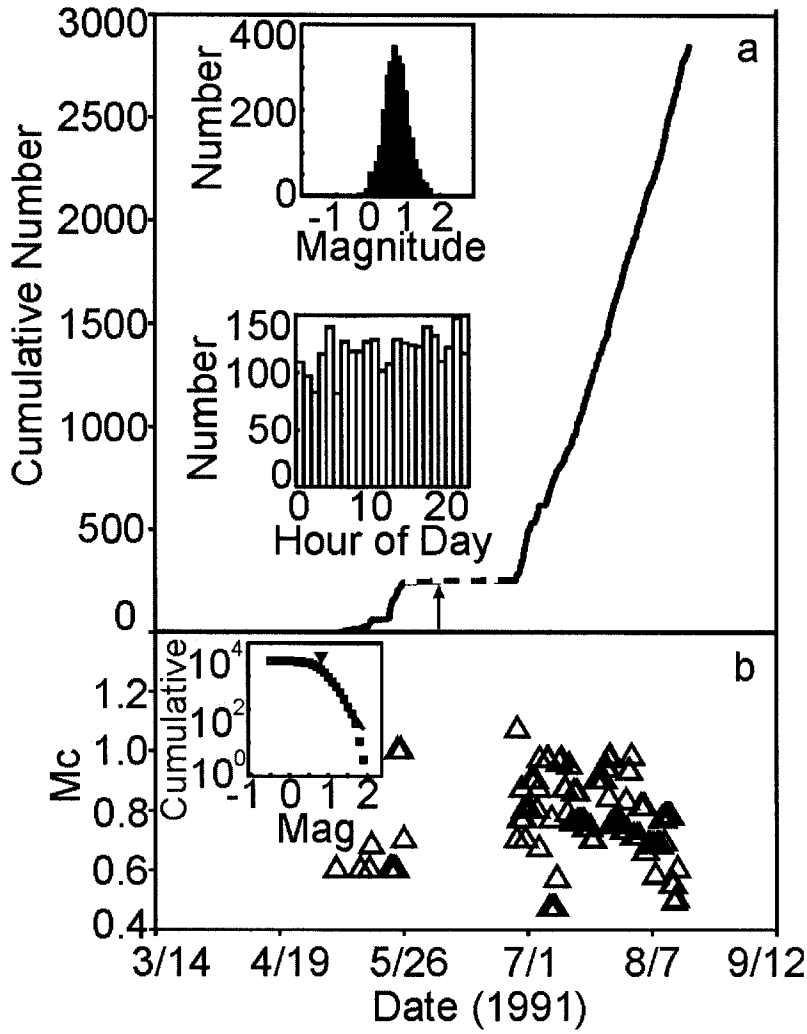

Figure 2.2. Seismicity rates and M_c. (a) Plot of cumulative number of located events as a function of time. Starting time is May 7; ending time is 19 August 1991. The vertical arrow marks the 15 June eruption. The dotted portion of the line indicates the period during which data were not usable (earthquakes not locatable) or no data were recorded. The inset in the upper part of the plot shows a histogram of number of events versus magnitude, and the inset in the lower part is a histogram of number of earthquakes versus hour of the day. (b) Magnitude of completeness, M_c, versus time. A constant number of events, n = 200, and an overlap of 5 events has been used. Triangles mark the center of the time window. The inset shows a plot of cumulative number of events versus magnitude, the triangle marks the automatic estimation of M_c=0.73 for the whole catalog, and the solid line is the weighted least-squares best fit to the distribution of events with $M_D \geq M_c$.

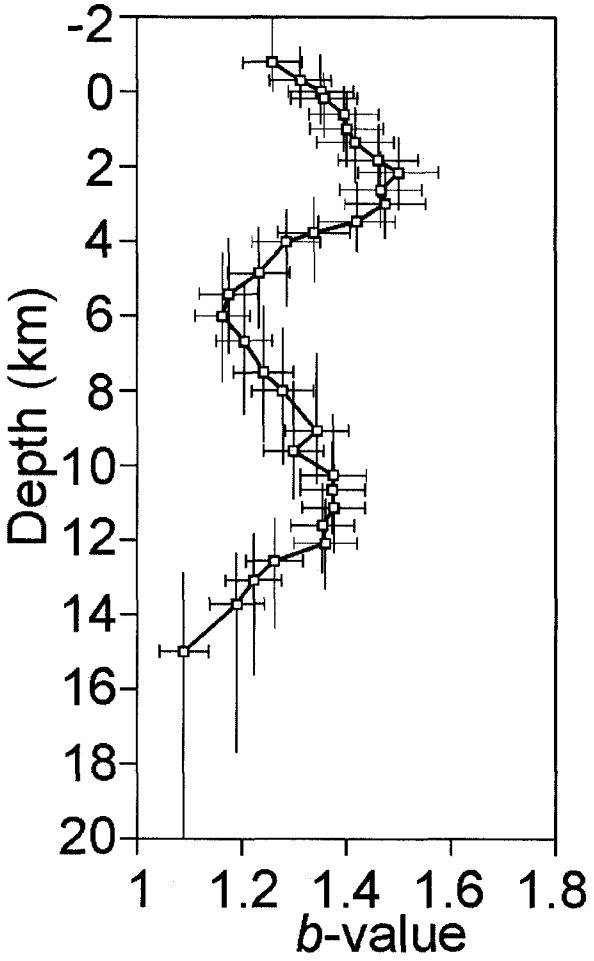

Figure 2.3. *b*-value versus depth. Plot of *b*-value as a function of depth for earthquakes at Mount Pinatubo. All depths are referenced to sea level. Each point represents 200 events with overlap of 5 events. Horizontal bars are standard deviations (σ) of *b*-value, vertical bars are the depth range that is represented by overlapped events.

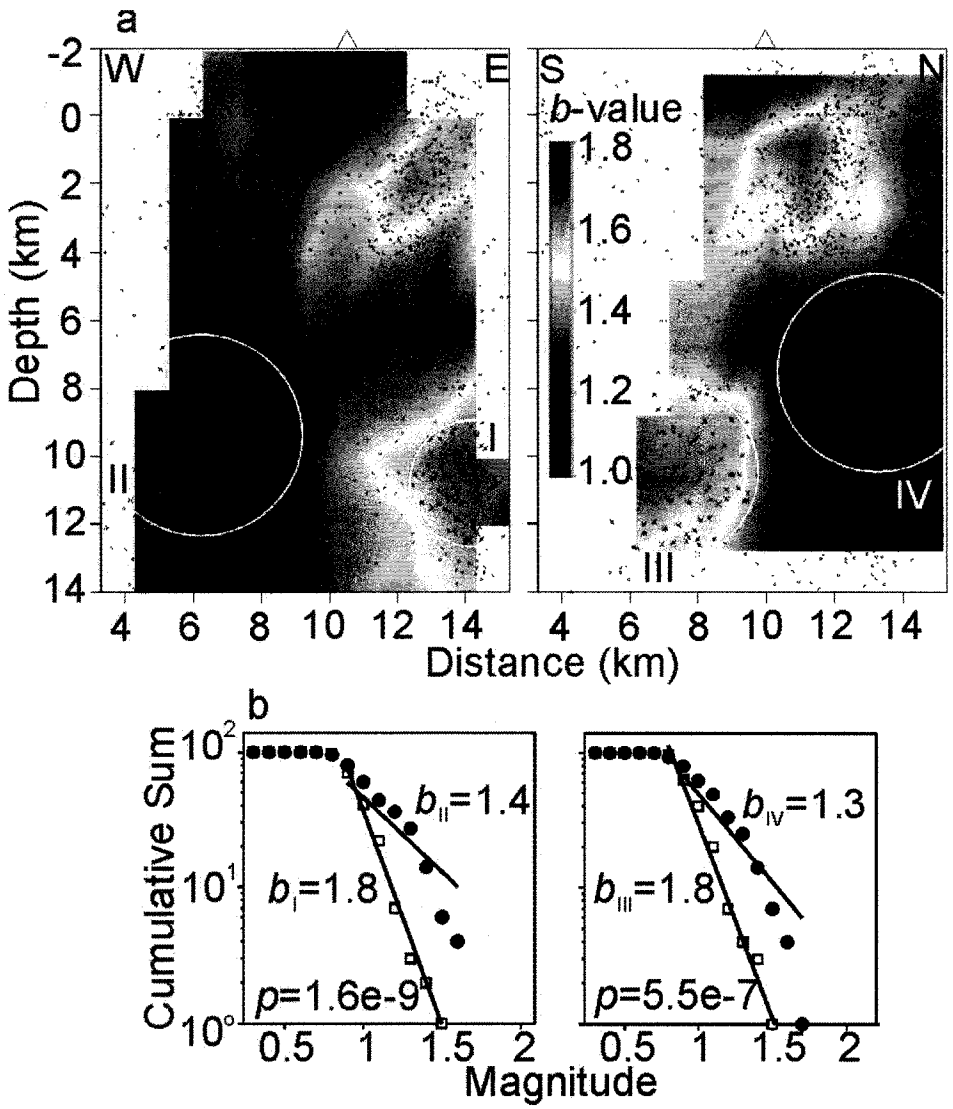

Figure 2.4. *b*-value cross sections and statistical tests. (a) Left: east–west cross section (A-A in Fig. 2.1), through the vent, showing *b*-values at Mount Pinatubo. A grid spacing of 1 km horizontally and 2 km vertically and the nearest $n = 100$ earthquakes were used. Blue and red colors indicate low and high *b*-values, respectively. Circles labeled with Roman numerals indicate samples for which *b*-values are compared, with selected earthquakes marked by "x," and black circles represent other earthquake hypocenters. Hollow triangle marks the location of the vent. Right: north–south cross section (B-B in Fig. 2.1) of *b*-values. (b) Left: The FMD for samples marked in the east–west cross section. The parameter *p* in the lower left of the graph is the probability that the two samples being compared belong to the same population. Solid circles and hollow squares mark the spatially different volumes. Right: The FMD for samples marked in the north–south cross section.

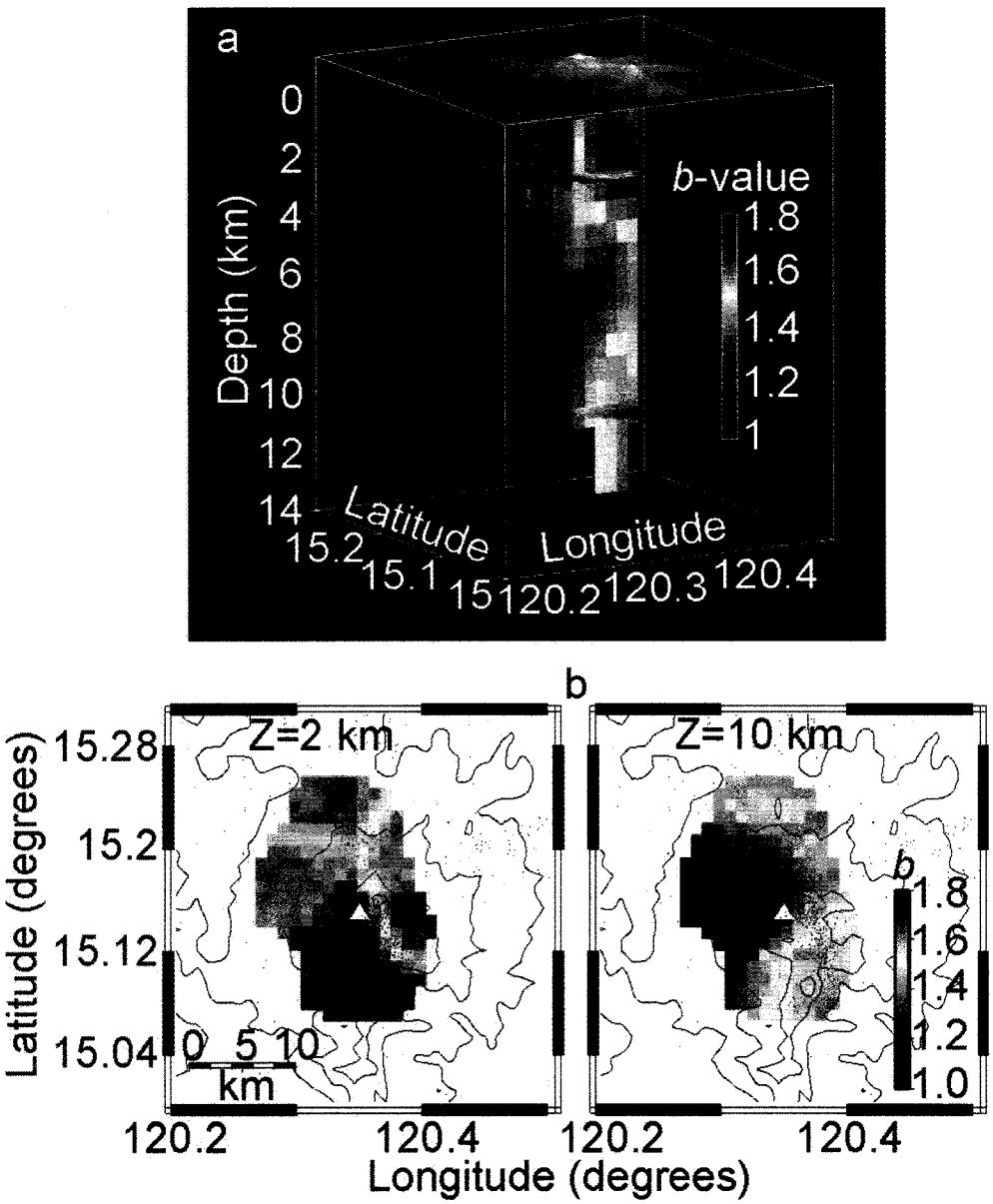

Figure 2.5. 3D mapping of *b*-values. (a) Three-dimensional view of *b*-values beneath Mount Pinatubo. View is from the southwest. A grid of 1 km x 1 km x 2 km (longitude, latitude, depth) and the nearest n = 100 earthquakes to each node were used. Hotter colors indicate high *b*-values. The two vertical slices are perpendicular to one another and cross the vent in east–west and north–south directions. Two horizontal slices at depths of 2 and 10 km are shown. (b) Left: Map view of horizontal slice at 2 km depth through the 3D *b*-value matrix. Solid white triangle marks the vent. Black dots mark earthquake epicenters. Topographic contours are drawn every 300 m. Other conventions as in (a). Right: Map view of horizontal slice at 10 km depth.

2.10. References

Aki, K. (1965). Maximum likelihood estimate of *b* in the formula log *N*= *a* - *bM* and its confidence limits, *Bull. Earthquake Res. Inst. Tokyo Univ.* **43,** 237–239.

Bautista, B. C., L. P. Bautista, R. S. Stein, E. S. Barcelona, R. S. Punongbayan, E. P. Laguerta, A. R. Rasdas, G. Ambubuyong, and E. Q. Amin (1996). Relationship of regional and local structures to Mount Pinatubo activity, in *Fire and Mud: Eruptions and Lahars of Mount Pinatubo, Philippines*, C. G. Newhall and R. S. Punongbayan (Editors), PHIVOLCS and University of Washington, Seattle, 351–370.

Eichelberger, J. C. (1995). Silicic volcanism: ascent of viscous magmas from crustal reservoirs, *Ann. Rev. Earth Planet. Sci.* **23**, 41–63.

Frolich, C., and S. Davis (1993). Teleseismic *b*-values: or much ado about 1.0, *J. Geophys. Res.* **98**, 631–634.

Gutenberg, B., and C. F. Richter (1944). Frequency of earthquakes in California, *Bull. Seism. Soc. Am.* **34**, 185–188.

Harlow, D. H., J. A. Power, E. P. Laguerta, G. Ambubuyong, R. A. White, and R. P. Hoblitt (1996). Precursory seismicity and forecasting of the June 15, 1991, eruption of Mount Pinatubo, in *Fire and Mud: Eruptions and Lahars of Mount Pinatubo, Philippines*, C. G. Newhall and R. S. Punongbayan (Editors), PHIVOLCS and University of Washington, Seattle, 285–305.

Ishimoto, M., and K. Iida (1939). Observations of earthquakes registered with the microseismograph constructed recently, *Bull. Earthquake Res. Inst. Tokyo Univ.* **17**, 443–478.

Jolly, A. D., and S. R. McNutt (1999). Seismicity at the volcanoes of Katmai National Park, Alaska: July 1995–December 1997, *J. Volcanol. Geotherm. Res.* **93**, 173–190.

Lockhart, A. B., S. Marcial, G. Ambubuyong, E. P. Laguerta, and J. A. Power (1996). Installation, operation, and technical specifications of the first Mount Pinatubo telemetered seismic network, in *Fire and Mud: Eruptions and Lahars of Mount Pinatubo, Philippines*, C. G. Newhall and R. S. Punongbayan (Editors), PHIVOLCS and University of Washington, Seattle, 215–223.

Mogi, K. (1962). Magnitude–frequency relation for elastic shocks accompanying fractures of various materials and some related problems in earthquakes, *Bull. Earthquake Res. Inst. Tokyo Univ.* **40**, 831–853.

Morgan, F. D., G. Wadge, J. Latchman, W. P. Aspinall, D. Hudson, and F. Samstag (1988). The earthquake hazard alert of September 1982 in southern Tobago, *Bull. Seism. Soc. Am.* **78**, 1550–1562.

Mori, J., D. Eberhart-Phillips, and D. H. Harlow (1996a). Three-dimensional velocity structure at Mount Pinatubo: resolving magma bodies and earthquake hypocenters, in *Fire and Mud: Eruptions and Lahars of Mount Pinatubo, Philippines*, C. G. Newhall and R. S. Punongbayan (Editors), PHIVOLCS and University of Washington, Seattle, 371–382.

Mori, J., R. A. White, D. H. Harlow, P. Okubo, J. A. Power, R. P. Hoblitt, E. P. Laguerta, L. Lanuza, and B. C. Bautista (1996b). Volcanic earthquakes following the 1991 climatic eruption of Mount Pinatubo: strong seismicity during a waning eruption, in *Fire and Mud: Eruptions and Lahars of Mount Pinatubo, Philippines*, C. G. Newhall and R. S. Punongbayan (Editors), PHIVOLCS and University of Washington, Seattle, 339–350.

Murru, M., C. Montuori, M. Wyss, and E. Privitera (1999). The locations of magma chambers at Mt. Etna, Italy, mapped by *b*-values, *Geophys. Res. Lett.* **26**, 2553–2556.

Newhall, C. G., and R. S. Punongbayan (Editors) (1996). *Fire and Mud: Eruptions and Lahars of Mount Pinatubo, Philippines.* PHIVOLCS and University of Washington, Seattle, 1126 pp.

Newhall, C. G., S. E. Albano, N. Matsumoto, and T. Sandoval (2001). Roles of groundwater in volcanic unrest, *J. Geol. Soc. Phil.* **56**, 69–84.

Pallister, J. S., R. P. Hoblitt, G. P. Meeker, R. J. Knight, and D. F. Siems (1996). Magma mixing at Mount Pinatubo: petrographic and chemical evidence from the 1991 deposits, in *Fire and Mud: Eruptions and Lahars of Mount Pinatubo, Philippines*, C. G. Newhall and R. S. Punongbayan (Editors), PHIVOLCS and University of Washington, Seattle, 687–731.

Power, J. A., M. Wyss, and J. L. Latchman (1998). Spatial variations in the frequency–magnitude distribution of earthquakes at Soufriere Hills volcano, Montserrat, West Indies, *Geophys. Res. Lett.* **25**, 3653–3656.

Rutherford, M. J., and J. D. Devine (1996). Preeruption pressure–temperature conditions and volatiles in the 1991 dacitic magma of Mount Pinatubo, in *Fire and Mud: Eruptions and Lahars of Mount Pinatubo, Philippines*, C. G. Newhall and R. S. Punongbayan (Editors), PHIVOLCS and University of Washington, Seattle, 751–766.

Scholz, C. H. (1968). The frequency–magnitude relation of microfracturing in rock and its relation to earthquakes, *Bull. Seism. Soc. Am.* **58**, 399–415.

Utsu, T. (1992). On seismicity, in Report of the Joint Research Institute for Statistical Mathematics, Institute for Statistical Mathematics, Tokyo, 139–157.

Warren, N. W., and G. V. Latham (1970). An experimental study of thermally induced microfracturing and its relation to volcanic seismicity, *J. Geophys. Res.* **75**, 4455–4464.

Wiemer, S. (1996). Seismicity analysis: new techniques and case studies, *Ph.D. Thesis*, University of Alaska, Fairbanks, 150 pp.

Wiemer, S. (2001). A software package to analyze seismicity: ZMAP, *Seism. Res. Lett.* **72**, 373–382.

Wiemer, S., and J. Benoit (1996). Mapping the *b*-value anomaly at 100 km depth in the Alaska and New Zealand subduction zones, *Geophys. Res. Lett.* **23**, 1557–1560.

Wiemer, S., and S. R. McNutt (1997). Variations in the frequency–magnitude distribution with depth in two volcanic areas: Mount St. Helens, Washington, and Mount Spurr, Alaska, *Geophys. Res. Lett.* **24**, 189–192.

Wiemer, S., and M. Wyss (2002). Mapping spatial variability of the frequency–magnitude distribution of earthquakes, in *Advances in Geophysics*, Vol. 43, R. Dmowska (Editor), 336 pp.

Wiemer, S., S. R. McNutt, and M. Wyss (1998). Temporal and three-dimensional spatial analysis of the frequency–magnitude distribution near Long Valley caldera, California, *Geophys. J. Int.* **134**, 409–421.

Wolfe, E. W., and R. P. Hoblitt (1996). Overview of the eruptions, in *Fire and Mud: Eruptions and Lahars of Mount Pinatubo, Philippines*, C. G. Newhall and R. S. Punongbayan (Editors), PHIVOLCS and University of Washington, Seattle, 3–20.

Wyss, M. (1973). Towards a physical understanding of the earthquake frequency distribution, *Geophys. J. R. Astr. Soc.* **31**, 341–359.

Wyss, M. (1991). Reporting history of the central Aleutians seismograph network and the quiescence preceding the 1986 Andreanof Island earthquake, *Bull. Seism. Soc. Am.* **81**, 1231–1254.

Wyss, M., F. Klein, K. Nagamine, and S. Wiemer (2001). Anomalously high *b*-values in the south flank of Kilauea Volcano, Hawaii: evidence for the distribution of magma below Kilauea's east rift zone, *J. Volcanol. Geotherm. Res.* **106**, 23–37.

Wyss, M., K. Shimazaki, and S. Wiemer (1997). Mapping active magma chambers beneath the off-Ito volcano, Japan, *J. Geophys. Res.* **102**, 413–420.

Zúñiga, R., and M. Wyss (1995). Inadvertent changes in magnitude reported in earthquake catalogs: influence on *b*-value estimates, *Bull. Seism. Soc. Am.* **85**, 1858–1866.

Zúñiga, R., and M. Wyss (2001). Most- and least-likely locations of large to great earthquakes along the Pacific coast of Mexico estimated from local recurrence times based on b-values, *Bull. Seism. Soc. Am.* **91**, 1717–1728.

Chapter 3. Spatial Mapping of the *b*-value at Galeras Volcano, Colombia, Using Earthquakes Recorded from 1995 to 2002[1]

3.1. Abstract

The catalog of volcano-tectonic earthquakes at Galeras volcano, Colombia, was analyzed to determine the magnitude of completeness of the seismograph network and to explore the subsurface structure by mapping the *b*-value of the frequency-magnitude distribution. By using 8,435 well-located earthquakes between 1995 and 2002 with duration magnitudes between -1.2 and 4.5 we found the catalog to be complete above M_c=0.26. The average *b*-value of 0.71 was found to be the result of an unintentionally stretched magnitude scale. A linear regression equation for local magnitudes was obtained from a group of 147 earthquakes recorded simultaneously by the short-period and broad band sub networks. The change in magnitude scale resulted in appositive shift of the average values for magnitude of completeness and *b* of ΔM_c=0.94 and Δb=0.44, respectively. The two- and three-dimensional mapping of *b*-value illuminates a vertically elongated structure beneath the active crater of Galeras down to a depth of 6 km, which may be associated with a conduit, or alternatively, with a shallow region of temporary magma storage. A structure with this geometry and location has not been found before in previous studies of *b*-value on volcanoes around the world.

[1] Sánchez, J.J., D. M. Gómez, R. A. Torres, M. L. Calvache, A. Ortega, A. P. Ponce, A. P. Acevedo, F. Gil-Cruz, J. M. Londoño, S. P. Rodríguez, J. de J. Patiño, and O. P. Bohórquez (2004). Spatial mapping of the *b*-value at Galeras volcano, Colombia, using earthquakes recorded from 1995 to 2002, *Submitted to Earth Sciences Research Journal.*

3.2. Introduction

Galeras volcano is located in southwestern Colombia, 9 km from the city of San Juan de Pasto (pop. ~ 350,000) and it is one of the most active volcanoes in the region, with frequent small-volume eruptions over the last 5,000 yr (Calvache et al., 1997). In 1988 Galeras showed signs of unrest and erupted explosively in 1989; an andesitic lava dome was emplaced during September-November 1991, and explosive activity took place again during 1992-1993. The last explosive eruption occurred on June 7, 2002 (Global Volcanism Network, 2003).

Between 1989 and 2002 the Observatorio Vulcanológico y Sismológico de Pasto (OVSP) compiled an important catalog of earthquakes' locations and this offers the possibility of determining the magnitude of complete detection and spatially mapping the *b*-value to explore the internal structure of the volcano down to a depth of 10 km. Between 1991 and 1992 the seismicity at Galeras was dominated by the occurrence of long-period events (LP) but also volcano-tectonic earthquakes (VT) were recorded (Gil-Cruz and Chouet, 1997). Both types of events, however, form the background seismicity at the volcano from 1993 until present. In this work we focus on the VT earthquakes. These earthquakes usually show sharp and distinct arrivals of P and S waves to the various seismograph stations, and broadband spectra, commonly above 5 Hz (Lahr et al., 1994). The sharp arrivals of P and S waves allow reliable location of the earthquakes. From 1993, the locations of VT earthquakes around Galeras illuminate several particularly active regions north of the active crater (Figure 3.1).

The distribution of earthquakes sizes in a region can be described by a law identified by Ishimoto and Iida (1939), and later by Gutenberg and Richter (1944):

$$\text{Log } N = a - bM \qquad (1)$$

where N is the cumulative number of earthquakes with magnitude larger than or equal to M, and a, b are constants that describe the activity of a seismogenic region and the relative distribution of earthquakes sizes, respectively. When plotting the cumulative number of earthquakes versus their magnitudes (frequency-magnitude distribution, FMD), b represents the slope of the best-fitting line for a certain magnitude range and is inversely proportional to the average size of faults that rupture during earthquakes (Aki, 1965). Values of b are close to 1.0 in the Earth's crust (Frolich and Davis, 1993) but in volcanic regions b is commonly higher than 1.0 (Wiemer and McNutt, 1997; Wyss et al., 2001, Sánchez et al., *2004*). This anomalously high b-value at volcanoes has been attributed to excessive material heterogeneity (Mogi, 1962), decreased applied stress (Scholz, 1968), decreased effective stress (high pore pressure) (Wyss, 1973), or alternatively, elevated thermal gradients (Warren and Latham, 1970). In this work we determine the magnitude of completeness (M_c) of the seismograph network and then we select a subset of data that is optimal for spatial mapping of b.

3.3. Data

Since 1989 the seismic activity at Galeras has been monitored with a 3 to 9-station seismograph network. (Figure 3.1). The network is equipped with five L-4 Mark Products vertical-component seismometers with natural frequency of 1 Hz, two L-22 Mark Products three-component seismometers with 2 Hz natural

frequency; and four Broadband, three-component seismometers (two Guralp CMG-40T and two Streckeisen STS-2) with 0.01 Hz natural frequency.

Earthquakes are located by reading the arrival times of P and S-waves to several seismograph stations and using the iterative computer program HYPO71 (Lee and Lahr, 1975). A one-dimensional model consisting of five layers over a half-space, with velocities increasing with depth, and constant Vp/Vs = 1.78 is used as approximation to the distribution of velocities in the Galeras area. Table 3.1 lists the parameters of the velocity model.

The VT earthquakes occur close to the active crater with an apparent tendency to align with the active faults mapped in the region of Galeras, particularly in direction SW-NE, although there are also earthquakes that align in direction SE-NW (Figure 3.1). The depths of earthquakes vary, but we observe a dominance of hypocenters between the summit and 10 km depth (Figure 3.2). We also observe that between 1989 and mid-1995 the seismicity rates vary quite frequently because of intense swarm activity. After August 1995 the distribution and rates of earthquakes are more representative of background-like seismicity.

We use the catalog of earthquakes and map the *b*-value to recognize the regions where the production rate of small earthquakes is statistically higher or lower than average. This is of interest because several workers at volcanoes elsewhere have suggested a relationship between high *b*-values, and possible regions of high material heterogeneity, high pore pressure, decreased applied stresses and high thermal gradients; which are conditions that intuitively are expected near magma conduits or reservoirs (see references in previous section).

On average, the number of stations used routinely for locations of VT earthquakes shows a clear tendency to increase with time (Figure 3.3), which also prompted us to use the more recent data since 1995. The original catalog compiled by OVSP starts in 1989 and includes 8,435 earthquakes with magnitudes in the range -1.2 to 4.5. The original magnitudes are duration magnitudes (M_D) estimated from the duration of shaking, starting from the onset of the P-waves until the coda waves are roughly equal in amplitude to the background noise. We discarded earthquakes without magnitude computation or with no estimates of the location errors.

We computed preliminary estimates of the M_c and *b*-values using the original M_D of earthquakes and found that the average M_c and *b*-value were 0.26 and 0.71, respectively. This suggests that the magnitude scale is unintentionally *stretched* and implies that in terms of the usual *b*-values (b~1) our anomalous volumes have low values. Nevertheless we could argue that it is still possible to map volumes of high *b*, relative to "normal" (what we define as the average *b* in our catalog). Although it is difficult to devise a more appropriate magnitude scale, we used amplitude data for 147 earthquakes recorded at the four broadband stations between April 2002 and September 2003, and duration data for the same set of earthquakes recorded by the short-period network to derive a regression equation to convert all magnitudes in the catalog from M_D to M_L (Figure 3.4). This implies that our new magnitudes will be scaled up by some amount and produce M_c and *b*-values that look comfortably similar to those in other areas. We use the rescaled magnitudes for the remainder of the study. We feel, however, that we still cannot directly compare *b*-values in one local catalog to those in another and recommend that the results of this work be cautiously used and with comparison purposes in the Galeras area only, without attempting to derive conclusions on the absolute value of *b*.

The histogram of the number of events versus magnitudes shows a simple distribution (Figure 3.5a); with some peaks, but in general it is uniform. The maximum in the number of earthquakes occurs in the magnitude range 1 to 1.5, which is a first indication of the value of M_c of the catalog. Indeed, an automatic estimate, based on weighted least squares, shows M_c = 1.2. The slope of the line that best fits the FMD for earthquakes with $M_L \geq 1.2$, is b = 1.15 (Figure 3.5b).

The errors in locations of earthquakes used here, as estimated by the computer program HYPO71 (Lee and Lahr, 1975), are on average 1 and 2 km in the horizontal and vertical directions, respectively. The errors in depth decrease to 1 km after August 1995, which may reflect the improvement of the monitoring network.

Because the M_c varies with time as a result of factors such as changes in seismograph network configuration and detection systems, instrumental failures, increased awareness and level of detail during times of volcanic unrest, and also temporal changes introduced by different human analysts during routine locations; we study the magnitude of completeness of the Galeras catalog by using a moving windows technique. For the catalog ordered sequentially in time, the detection threshold is calculated for the first 300 events by using the FMD, then the window is moved forward in time by 5 events and the computation is repeated, proceeding systematically until the end of the catalog. In this fashion we obtain a smoothed graph of M_c versus time (Figure 3.6).

We decided to divide the catalog of VT earthquakes at Galeras into two periods: pre- and post-August 1995. Because the activity prior to August 1995 was characterized by swarm activity we use only 1918 earthquakes with $M_L \geq$

1.2 recorded between September 1995 - June 2002 that represent better the background seismicity. This decision is based on the temporal characteristics of the VT activity (Figure 3.2), the gradual improvement of the seismograph network that resulted in a higher number of stations being used for the locations (Figure 3.3); and on average, a lower M_c (Figure 3.6), which allows expanding the range in magnitudes for analysis and maximizes the usable number of earthquakes. We note that the error estimates of our earthquake data are within the uncertainties that are usually expected for locations obtained from arrival times to stations in a sparse network. Our mapping of *b*-values is based on grids with nodes separated accordingly.

3.4. Method

To compute the *b*-value, we apply the method of Maximum Likelihood (Aki, 1965),

$$b = 2.3/(M_{avg} - M_o) \qquad (2)$$

where M_{avg} is the mean magnitude and $M_o = M_c - 0.05$ (0.05 is a half of the magnitude bin unit of 0.1). Because $M_{avg} - M_o$ and *b* are inversely proportional, whenever we measure *b*, we are also measuring M_{avg}.

To map *b* we use the method of Wiemer and Benoit (1996), Wyss et al., (1997), and Wiemer et al., (1998). Briefly, the *b*-values are calculated in two and three dimensions at grid nodes that are 2 km apart (horizontally and vertically), using a fixed number of earthquakes (n = 100) without limiting the size of the sampling volumes. During this mapping we observed that the radius of sampling varied between 1 and 6 km. In two dimensions, the nearest 100 earthquakes are selected according to their distances projected onto a vertical (cross-

section) or horizontal (map-view) plane; therefore the sampling volumes are cylinder-shaped and varying in height. In the case of three-dimensional mapping the sampling volumes have the shape of spheres. To verify that the results are independent of the method used, we computed *b*-values using two methods: Maximum Likelihood (ML) and Weighted Least Squares (WLS). Because the spatial patterns in *b*-values were invariant, we only show the maps obtained using the ML method. For a detailed discussion on the different methods used to estimate *b* and a comparison of results, the reader is referred to Centamore et al., 1999.

3.5. Results

The average *b*-value ($M_L \geq 1.2$) between September 1995 and June 2002 starts at $b = 1.46$ at shallow depths, decreases gradually to $b = 1.0$ at 7 km depth, then decreases rapidly to $b = 0.7$ at a depth of 8 km and below this depth the *b*-values oscillate between $b = 0.7$ and $b = 0.9$. Below 14 km depth the number of earthquakes is not large enough to estimate reliably the *b*-values (Figure 3.7). In map view and cross-section through the active crater (Figure 3.8a, b) we see that regions of low *b*-value are common and that the region located adjacent to and beneath the active crater shows the highest *b*-values, this region extends from the summit of the volcano down to a depth of 5 km.

These spatial patterns persisted when we mapped *b* under the assumption that M_c varies spatially at each sampling node; assuming that M_c is constant through the region; or changing the sampling method by using constant radius of 2 km and letting the number of earthquakes float. The differences in *b-values* among spatially different volumes are significant because the estimated probabilities that samples taken from contrasting regions come from the same population (Utsu, 1992) are low (Figure 3.8c). The three-dimensional mapping

of *b* for Galeras volcano (Figure 3.9) confirms that the high *b*-values region is located beneath the active crater and vertically elongated down to 5 km depth.

3.6. Discussion

The *b*-values calculated in this study are similar to those found by Eraso and Guerra (2002) in their study of the seismogenic regions around Galeras. They found that shallow sources that are close to the crater show *b*-values that are higher than those for deeper sources away from the vent. Because the absolute value of *b* depends on the magnitude scale used (Zúñiga and Wyss, 2001) we suggest that our estimates be taken with caution and used only for comparison purposes within the Galeras region. The contrast in *b*-value among different volumes that we document here is robust because the statistical tests indicate low probabilities that samples taken from contrasting regions are the same; and the spatial pattern of anomalies in *b*-values persists, independent of the methods used in sampling of earthquakes and estimating *b*.

Wiemer (1996) put forward the idea that restricted volumes of anomalously high *b*-values exist at volcanoes. This hypothesis has been tested at a number of volcanic regions: Mt. St. Helens, Washington, and Spurr, Alaska (Wiemer and McNutt, 1997); Off-Ito, Japan (Wyss et al., 1997); Long Valley, California (Wiemer et al., 1998); Soufriere Hills, Montserrat (Power et al., 1998); Katmai, Alaska (Jolly and McNutt, 1999), Etna, Italy (Murru et al., 1999); Kilauea, Hawaii (Wyss et al., 2001); and Mt. Pinatubo, Philippines (Sánchez et al., 2004). Thus, high *b*-value anomalies seem pervasive and independent of the type of volcano, although the pattern of the anomalies does vary.

There are many possible causes for higher-than-normal *b*-values at volcanoes. At Galeras, the high material heterogeneity was highlighted as likely

by Eraso and Guerra (2002) and related to the high *b*-values calculated for sources beneath and west of the vent. A possible source of the material heterogeneity close to the crater could be the fracturing of a semi-brittle magma body. When rapidly deformed, these bodies can fracture just as seen on the surface of lava domes, and the earthquakes thus generated would be relatively small (Newhall et al., 2001). Because Galeras has shown frequent eruptive activity, including emplacement of a lava dome (Calvache and Williams, 1997), we speculate that the high *b*-values found beneath the active crater may correspond to the regions adjacent to a conduit, the remnants of a semi-crystallized intrusion, or a shallow and temporary magma reservoir.

The total volume of the dome and its conduit system emplaced at Galeras between 1990 and 1992 was estimated to be 8.4 x 10^6 m^3 by Calvache and Williams (1997). The *b*-value anomaly that we report here is larger, ~ 32 x 10^6 m^3, which makes sense, if it surrounds a shallow semi-crystallized magma body.

Temporal changes in *b*-values at Galeras have been studied with some detail (Torres and Gómez, *Pers. Comm.,* 2004). The *b*-values on the most active seismogenic sources at Galeras are also in the range 1.0 – 1.4 and they speculated that the variations in *b* were related to changes in the volcano's eruptive activity. In this work, however, we limit our analysis to spatial changes and suggest, as future work, the refining of the study of temporal variations by using a differential mapping technique (e. g. Wiemer et al., 1998).

Galeras is not the exception among other volcanoes where *b* has been mapped, and several other possibilities for the generation of higher-than-normal *b*-values remain an open question. The location and apparent configuration of the anomaly found here, however, illuminates a new feature that has not been

mapped by this method before (Figure 3.9). Perhaps the application of earthquake-relocation techniques and mapping using another approach (such as P-and S-wave velocity tomography) can put our results to the test.

3.7. Conclusions

The relative distribution of VT earthquakes magnitudes at Galeras volcano, Colombia has been mapped to a depth of 8 km below the summit. We found relatively higher *b*-values in an elongated region below the vent and down to a depth of 5 km. This indicates the occurrence of earthquakes that are smaller than average. The higher-than-normal *b*-values can result from high pore pressure, repeated intrusions and eruptions, or alternatively, from high material heterogeneity (as produced by many fractures). There exists the possibility that we are illuminating the region adjacent to the conduit, a shallow magma reservoir, or the remnants of a semi-crystallized intrusion.

3.8. Acknowledgements

The authors wish to thank INGEOMINAS and all the staff at OVSP, Colombia, for their hard work in maintaining the monitoring network at Galeras, also for the help and data provided during the visit of one of the authors (J.J.S.) during which this work was initiated. IAVCEI provided some financial support for the project. Natalie Ortiz helped in the organization and compilation of data. Max Wyss provided advice and helpful discussion.

3.9. Figures

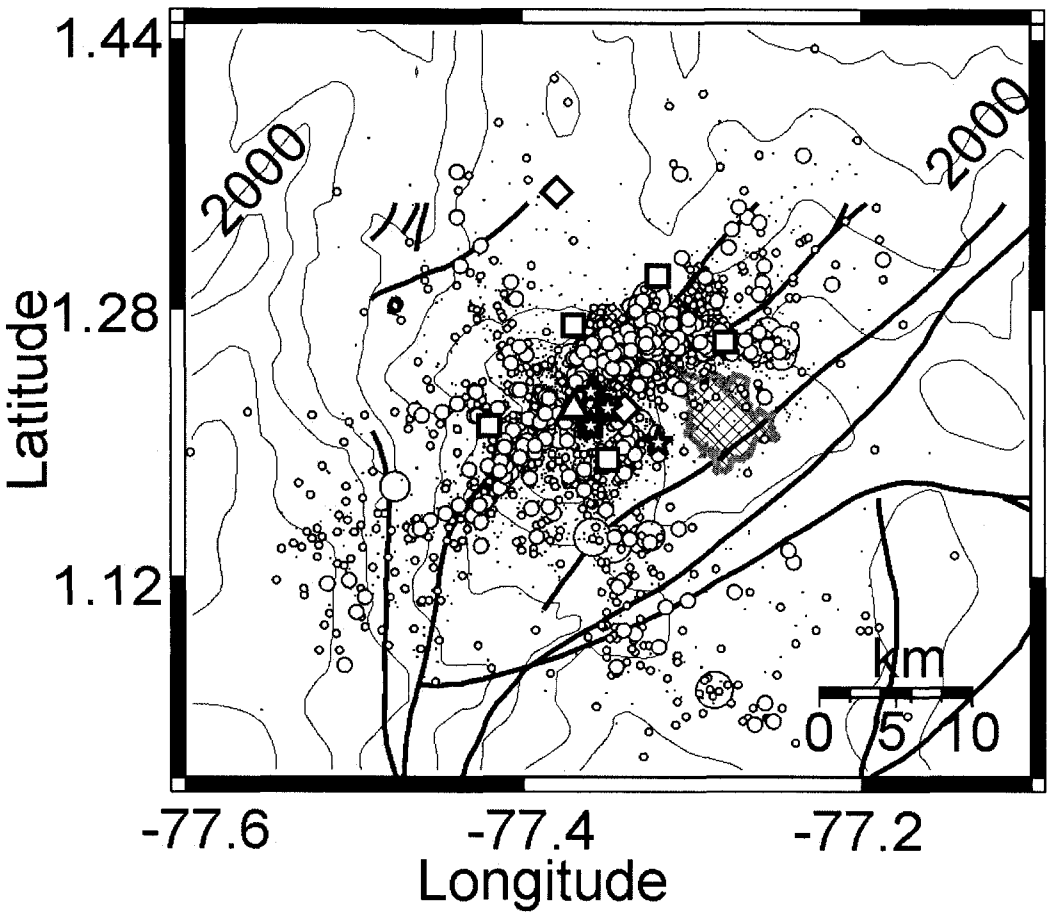

Figure 3.1. Map of Galeras volcano. Topographic contours drawn every 500 m. Circles represent epicenters of VT earthquakes recorded between 1989-2002, with magnitudes ranging between M=1 and M=3.8. The triangle marks the active crater. Thick solid lines cutting through topography are fault segments and the hatched area southeast of Galeras indicates the limits of the city of San Juan de Pasto. Squares- seismograph stations equipped with short-period, vertical component seismometers; diamonds-short-period, three component stations; stars- broadband stations.

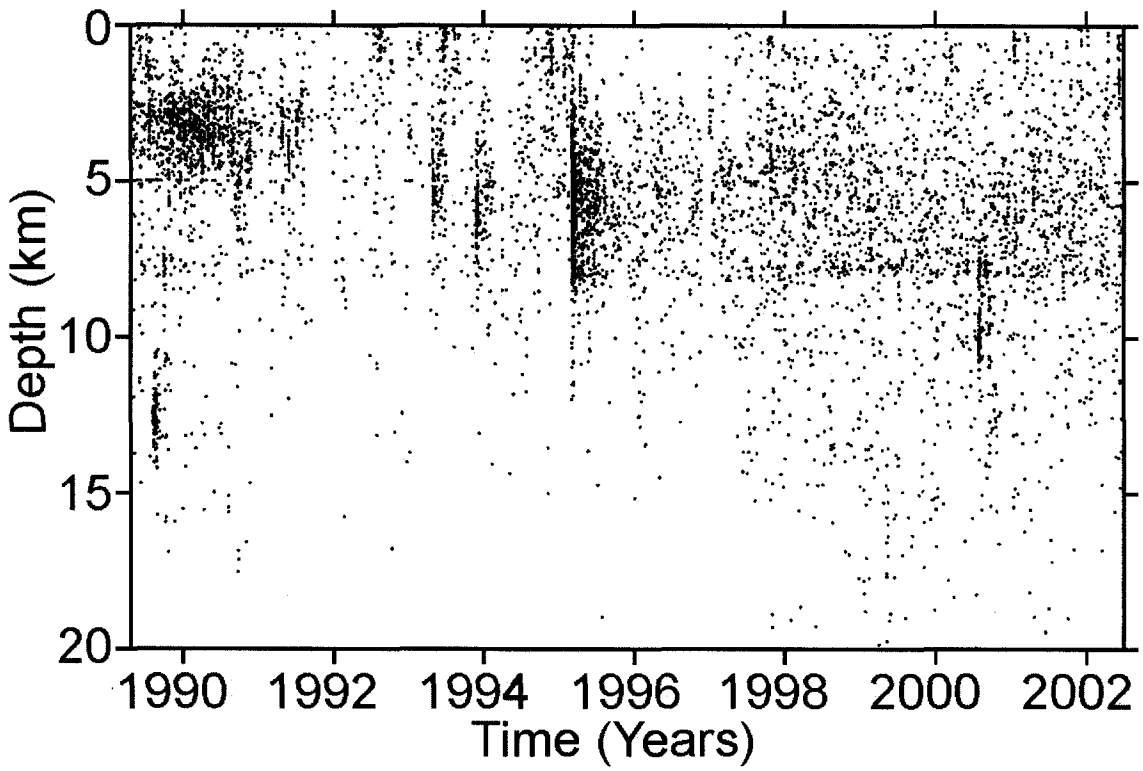

Figure 3.2. Seismicity versus time. Time-Depth plot for VT earthquakes at Galeras for earthquakes recorded between 1989 and 2002. Depths are referenced to the volcano's summit, which is 4,200 meters above sea level. Seismicity prior to August 1995 is characterized by swarm activity, and during subsequent years the seismicity is more representative of a steady background-like activity.

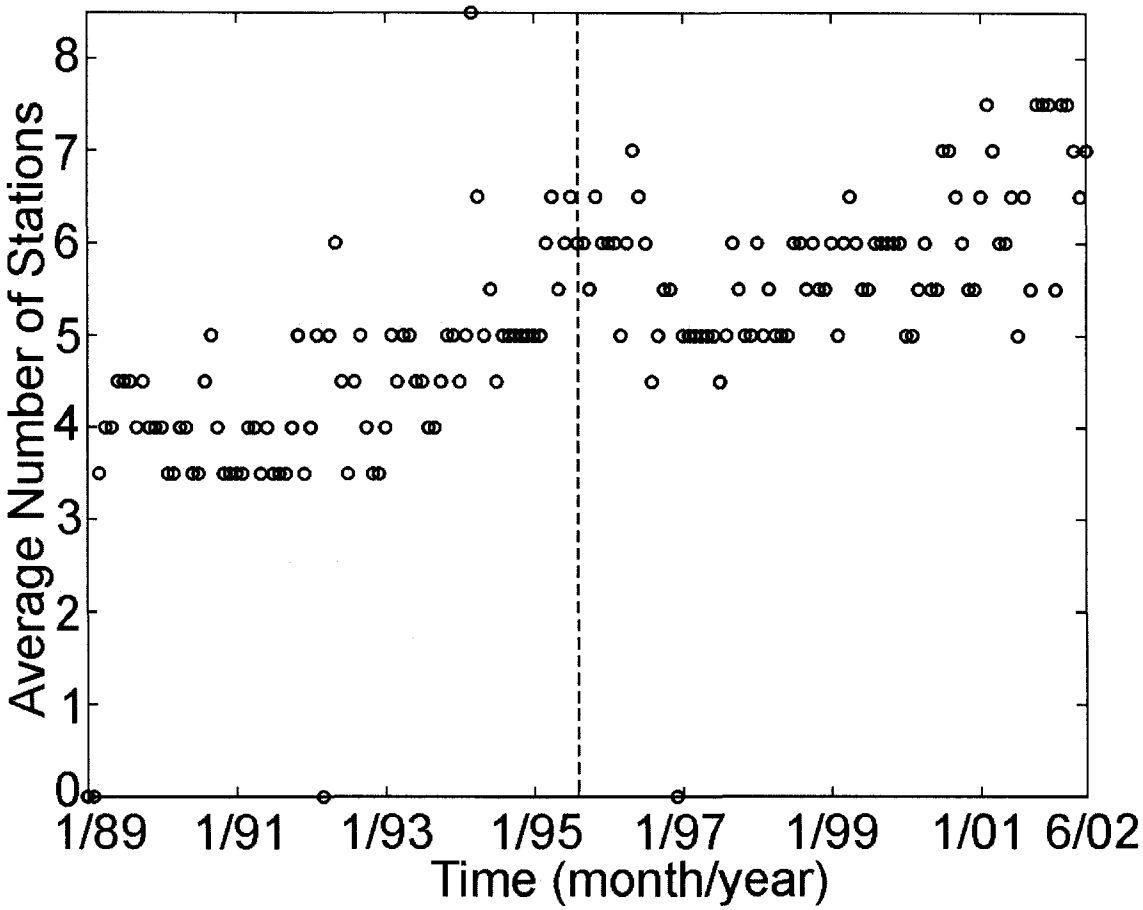

Figure 3.3. Number of stations versus time. Average number of stations used in the locations of VT earthquakes at Galeras. The vertical dashed line indicates the date August 1995. Values of zero were assigned whenever the catalog did not have locations during a particular month.

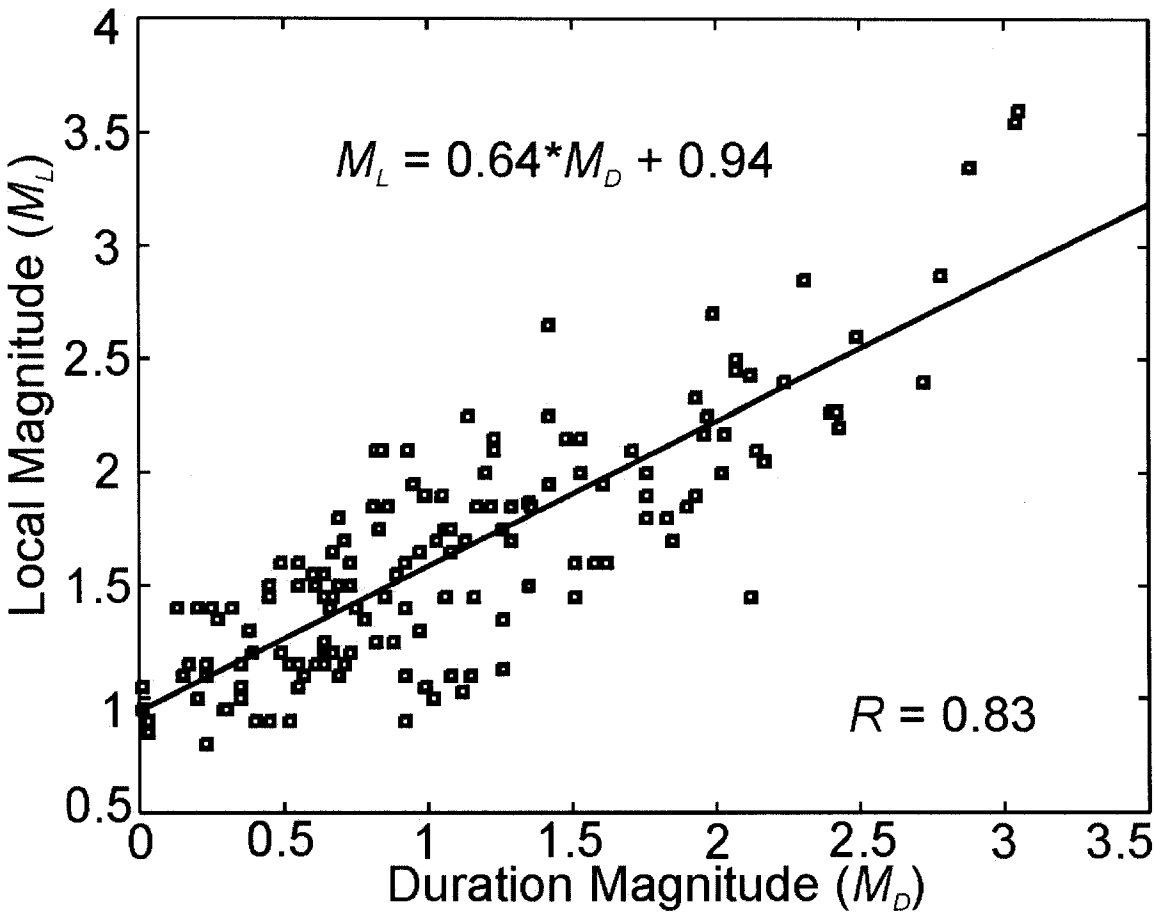

Figure 3.4. Equation for conversion of magnitudes. Regression equation for M_L. Plot of duration magnitude versus local magnitude for 147 VT earthquakes simultaneously recorded by the broad band and short period subnetworks. The solid line is the best fit to the data. The regression equation is used to re-compute all duration magnitudes used in the mapping of *b*-values at Galeras. The change of magnitude scale results in positive shifts of the average magnitude of completeness and *b*-value of $\Delta M_c = 0.94$ and $\Delta b = 0.44$, respectively.

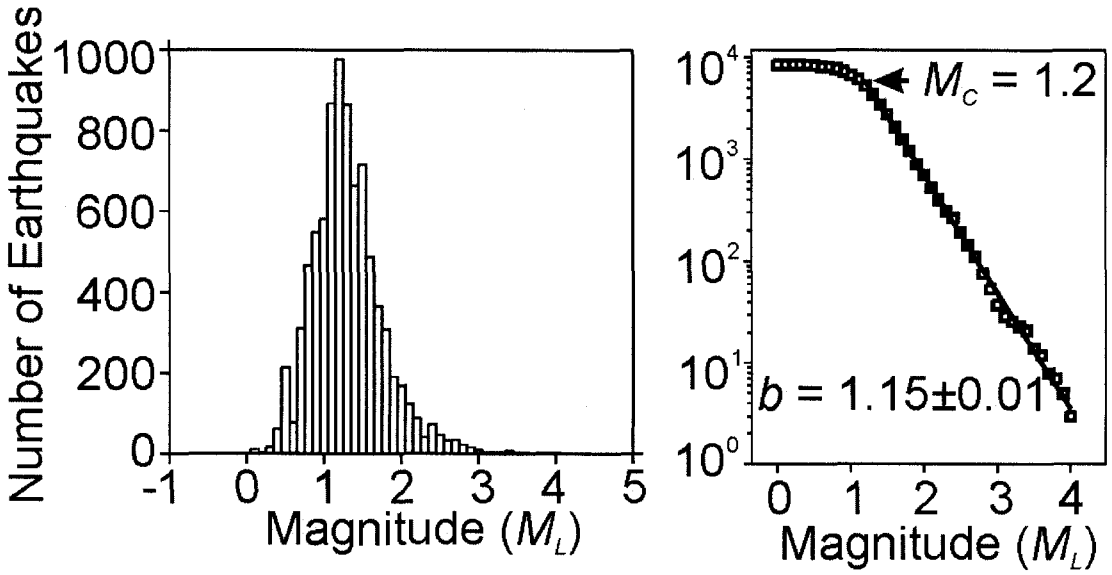

Figure 3.5. Average M_c. (a) Histogram of the number of events versus magnitudes for the original catalog compiled by OVSP. The magnitude bins are equal to 0.1. (b) The frequency-magnitude distribution (FMD) for all earthquakes at Galeras. The solid line shows the least squares best fit. The magnitude of completeness (M_c) is indicated by the arrow.

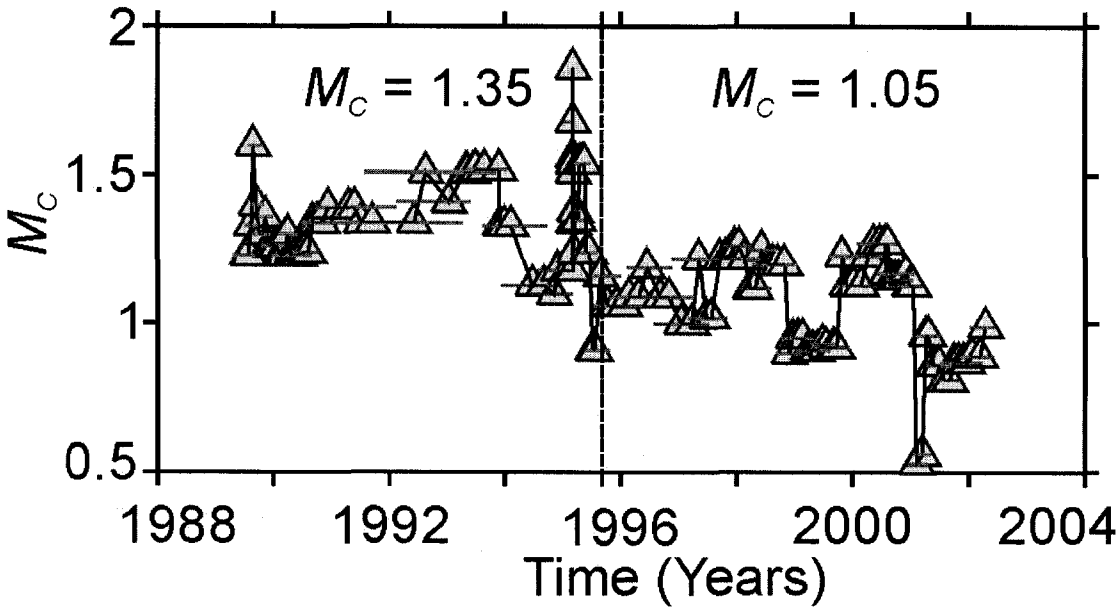

Figure 3.6. M_c versus time. The detection threshold is computed in moving windows with 300 earthquakes each, stepping 5 events. Triangles indicate the M_c for any particular window; horizontal lines show the window width (in time) of each group of 300 earthquakes. The average values of M_c before and after mid 1995 (vertical dashed line) are given.

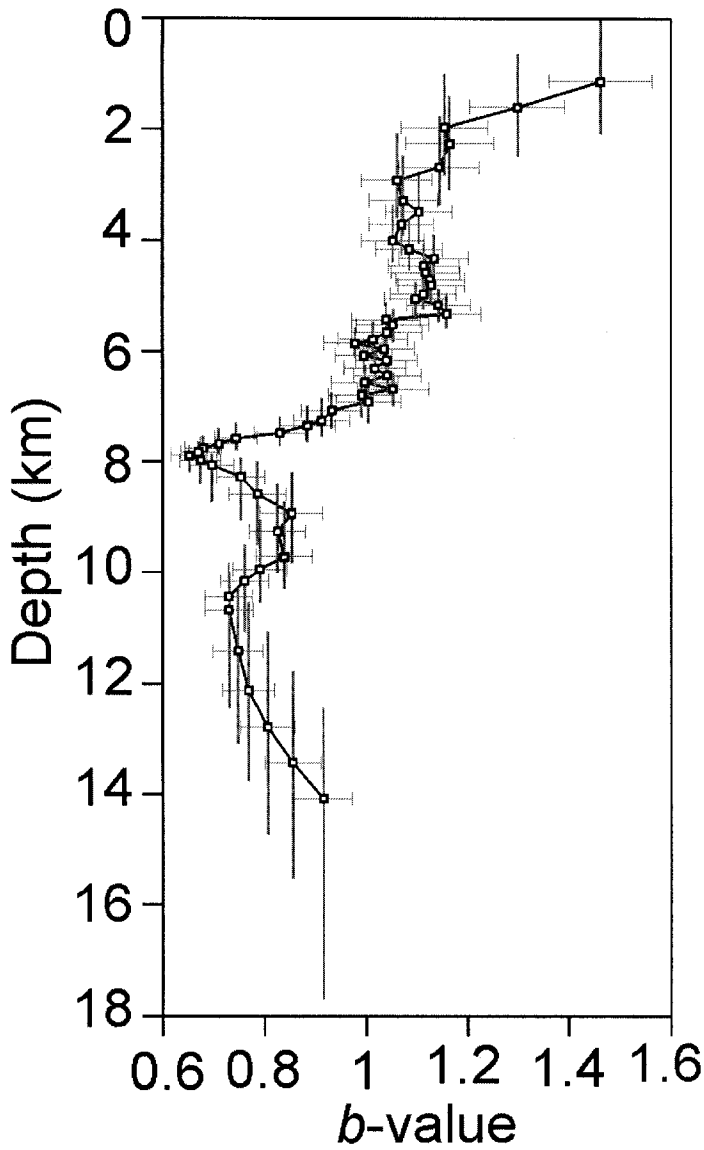

Figure 3.7. Average *b*-values versus depth at Galeras. To compute *b* we used mobile windows of 300 earthquakes each, stepping 5 events. Squares mark the center of the window, vertical lines show the window size and horizontal lines show the 1σ standard deviation.

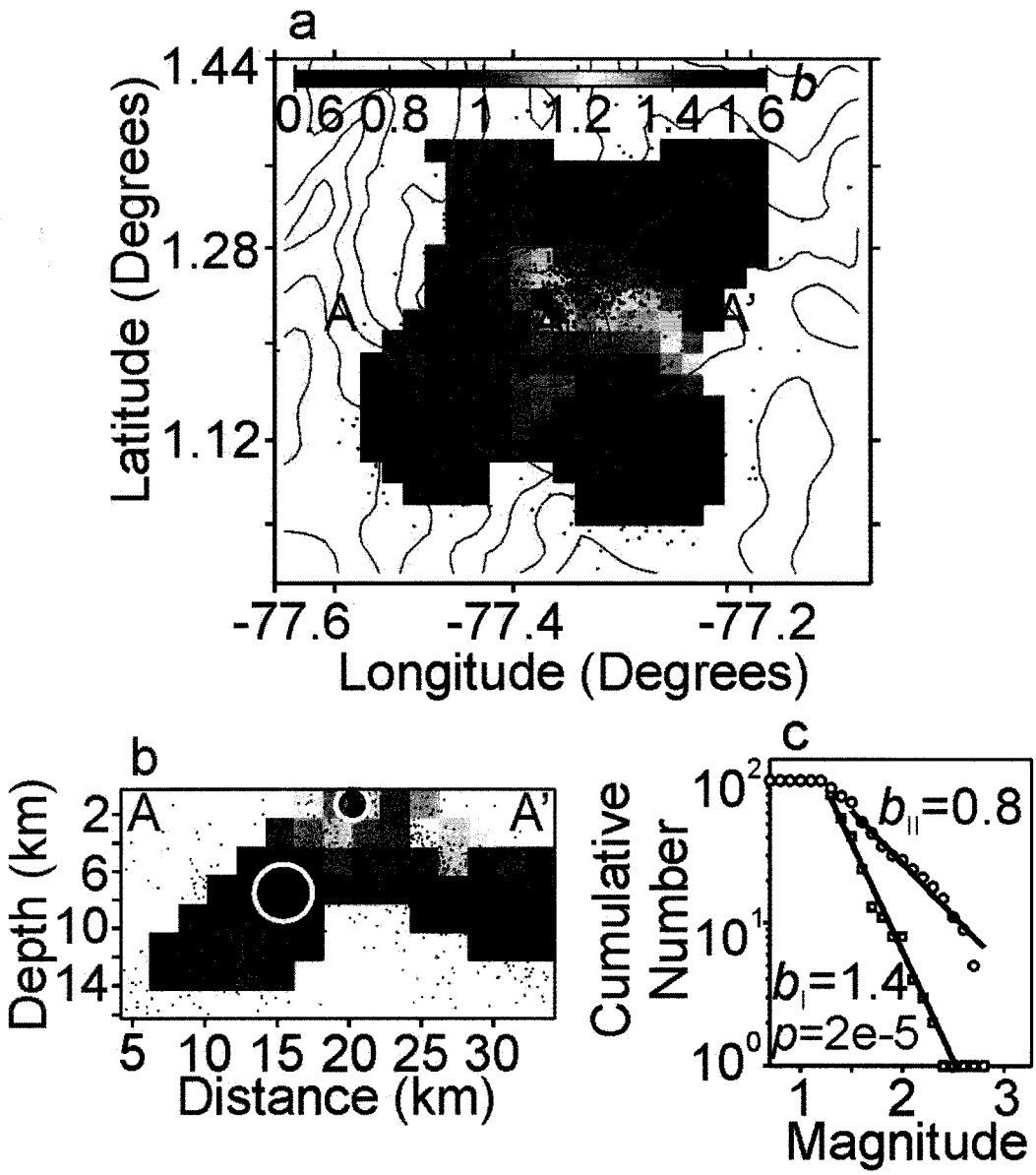

Figure 3.8. 2D mapping of *b*-values. (a) Map view showing the *b*-values at Galeras. Blue and reddish colors indicate low and high *b*-values, respectively. Nodes separated by 2km. A-A' indicates the length and orientation of the cross section. The white and red triangle marks the active crater. Other conventions as in Figure 3.1. (b) WE cross-section through the vent, showing the *b*-values at Galeras volcano. White circles labeled "I" and "II" enclose samples for which *b*-values are compared, selected earthquakes are marked by "x" and black dots mark other earthquake hypocenters. (c) . Frequency-magnitude distribution for selected samples in (b). The value *p* indicates the probability that the two samples being compared come from the same population (Utsu, 1992).

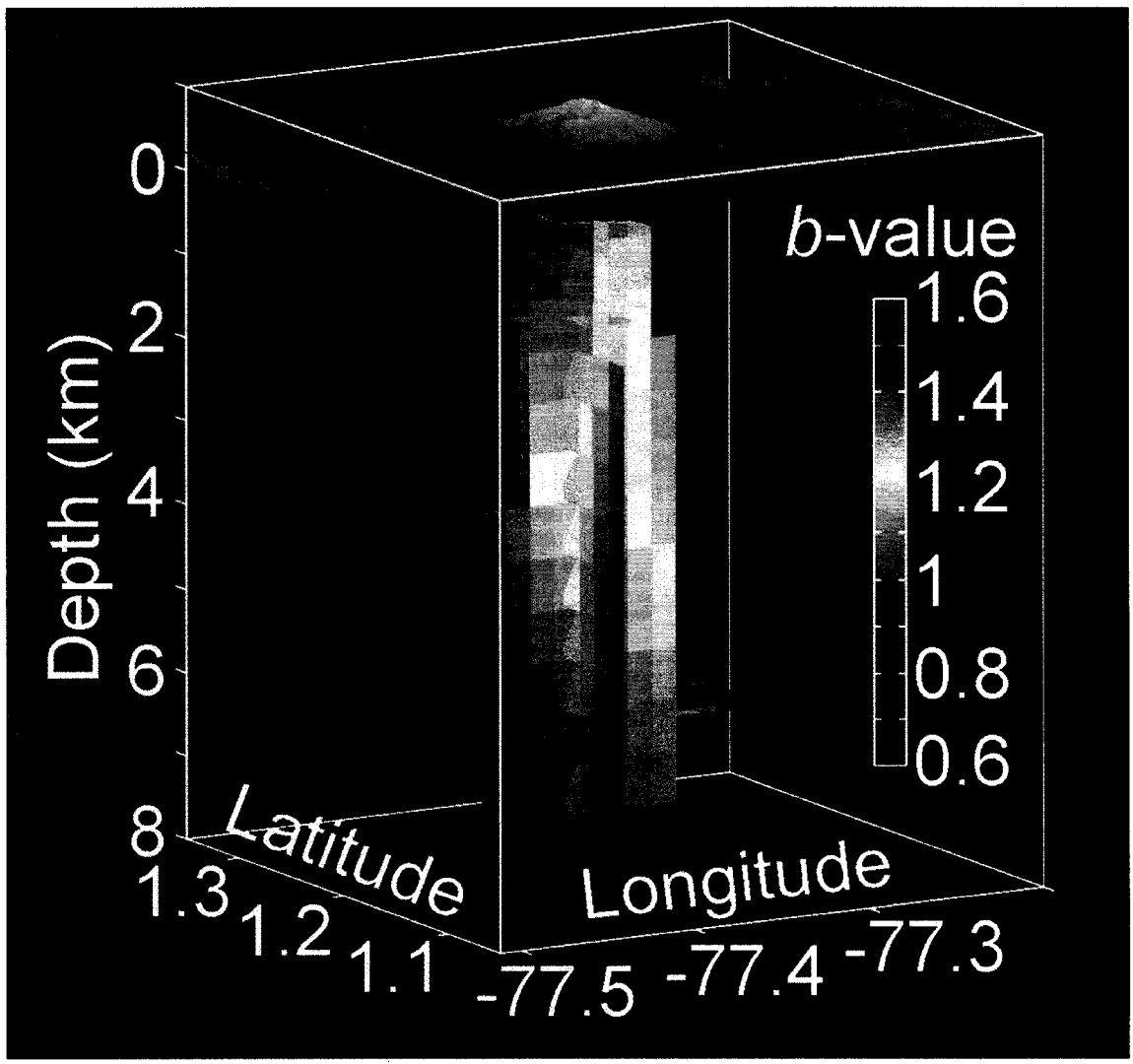

Figure 3.9. 3D view of *b*-values at Galeras. The mapping of *b* is performed in a 2km x 2km x 2km grid (Lat., Lon., Depth) selecting the nearest 100 earthquakes to each node. The two vertical slices are mutually orthogonal and intersect at the vent in WE and NS directions. Two additional horizontal slices are shown at depths of 1.5 and 6.5 km. The light and dark tones of gray represent the topography (lighter colors are topographic highs). Conventions as in Figure 3.8.

3.10. Tables

Table 3.1. Velocity model used for the locations of earthquakes at Galeras volcano.

Depth of top of layer (km)	P-wave velocity (km/s)
0.0	3.5
2.0	3.7
4.0	4.0
8.0	6.0
26.0	6.8
44.0	8.0

3.11. References

Aki, K. (1965): "Maximum likelihood estimate of *b* in the formula log *N=a-bM* and its confidence limits". *Bulletin of the Earthquake Research Institute, University of Tokyo,* **43,** 237-239.

Calvache, M. L. and S. N. Williams. (1997): "Emplacement and evolution of the andesitic dome of Galeras volcano, 1990-1992". *Journal of Volcanology and Geothermal Research*, **77**, 57-69.

Calvache, M. L., G. P. Cortéz, and S. N. Williams (1997): "Stratigraphy and chronology of the Galeras volcanic complex, Colombia". *Journal of Volcanology and Geothermal Research*, **77**, 5-19.

Centamore, C., G. Patane, and T. Tuve (1999): "Maximum entropy estimation of b values at Mt. Etna: comparison with conventional least squares and maximum likelihood results and correlation with volcanic activity". *Annali di Geofisica*, **42**, 515-528.

Eraso, J. F., y Guerra, A. C. (2002): "Análisis de fuentes sismogénicas registradas por la red sismológica de vigilancia del volcán Galeras, como una contribución al estudio de amenaza sísmica de la región de influencia del volcán", *Tésis de Grado, Universidad de Nariño, Facultad de Ingeniería Civil, San Juan de Pasto.*

Frolich, C. and S. Davis (1993): "Teleseismic *b*-values: Or much ado about 1.0". *Journal m of Geophysical Research*, **98**, 631-634.

Gil Cruz, F. and B. Chouet (1997): "Long-period events, the most characteristic seismicity accompanying the emplacement and extrusion of a lava dome in Galeras volcano, Colombia, in 1991". *Journal of Volcanology and Geothermal Research*, **77**, 121-158.

Global Volcanism Network (2003): "Bulletin of the Global Volcanism Network 28:02". *http://www.volcano.si.edu/world/region15/colombia/galeras*

Gutenberg, B. and C. F. Richter (1944): "Frequency of Earthquakes in California". *Bulletin of the Seismological Society of America,* **34**, 185-188.

Ishimoto, M. and K. Iida (1939): " Observations of earthquakes registered with the microseismograph constructed recently". *Bulletin of the Earthquake Research Institute, University of Tokyo,* **17,** 443-478.

Jolly, A. D., and S. R. McNutt. (1999): "Seismicity at the volcanoes of Katmai National park, Alaska; July 1995-December 1997". *Journal of Volcanology and Geothermal Research,* **93**, 173-190.

Lahr, J.C., B. A. Chouet., C. D. Stephens., J. A. Power and R. A. Page (1994): "Earthquake classification, location, and error analysis in a volcanic environment: implications for the magmatic system of the 1989-1990 eruptions at Redoubt volcano, Alaska". *Journal of Volcanology and Geothermal Research*, **62,** 1-4, 137-151.

Lee, W. H. K. and J. C. Lahr (1975): "HYPO71 (Revised): a computer program for determining hypocenter, magnitude, and first motion pattern of local earthquakes". *U. S. Geological Survey Open-File Report* **75-311**.

Mogi, K. (1962): "Magnitude-frequency relation for elastic shocks accompanying fractures of various materials and some related problems in earthquakes". *Bulletin of the Earthquake Research Institute, University of Tokyo,* **40**, 831-853.

Murru, M. C., C. Montuori, M. Wyss, and E. Privitera. (1999): "The locations of magma chambers at Mt. Etna Italy, mapped by *b*-values". *Geophysical Research Letters,* **26**, 2553-2556.

Newhall, C. G., S. E. Albano, N. Matsumoto and T. Sandoval. (2001): "Roles of groundwater in volcanic unrest". *Journal of the Geological Society of Philippines,* **56**, 69-84.

Power, J. A., M. Wyss and J. L. Latchman. (1998): "Spatial variations in the frequency-magnitude distribution of earthquakes at Soufriere Hills volcano, Montserrat, West Indies". *Geophysical Research Letters,* **25**, 3653-3656.

Sánchez, J. J., S. R. McNutt., J. A. Power and M. Wyss. (2004): "Spatial variations in the frequency-magnitude distribution of earthquakes at Mount Pinatubo volcano". *Bulletin of the Seismological Society of America,* **94**, 430-438.

Scholz, C. H. (1968): "The frequency-magnitude relation of microfracturing in rock and its relation to earthquakes". *Bulletin of the Seismological Society of America,* **58**, 399-415.

Utsu, T. (1992): "On seismicity" in: *Report of the Joint Research Institute for Statistical Mathematics*, p. 139-157, Institute for Statistical Mathematics, Tokyo.

Warren, N. W. and G. V. Latham (1970): "An experimental study of thermally induced microfracturing and its relation to volcanic seismicity". *Journal of Geophysical Research,* **75**, 4455-4464.

Wiemer, S. (1996): " Seismicity analysis: new techniques and case studies". *Ph.D. thesis, University of Alaska, Fairbanks*, Fairbanks, 150 p.

Wiemer, S. and J. Benoit (1996): "Mapping the b-value anomaly at 100 km depth in the Alaska and new Zealand subduction zones". *Geophysical Research Letters*, **23**, 1557-1560.

Wiemer, S. and S. R. McNutt (1997): "Variations in the frequency-magnitude distribution with depth in two volcanic areas: Mount St. Helens, Washington, and mount Spurr, Alaska". *Geophysical Research Letters*, **24,** 189-192.

Wiemer, S., S. R. McNutt and M. Wyss (1998): "Temporal and three-dimensional spatial analysis of the frequency-magnitude distribution near Long-Valley caldera, California". *Geophysical Journal International*, **134**, 409-421.

Wyss, M., F. Klein., K. Nagamine and S. Wiemer (2001): "Anomalously high *b*-values in the South flank of Kilauea volcano, Hawaii: evidence for the distribution of magma below Kilauea's East rift zone". *Journal of Volcanology and Geothermal Research*, **106**, 23-37.

Wyss , M., K Shimazaki and S. Wiemer (1997): "Mapping active magma chambers beneath the off-Ito volcano, Japan". *Journal of Geophysical Research*, **102**, 413-420.

Wyss, M. (1973): "Towards a physical understanding of the earthquake-frequency distribution". *Geophysical Journal of the Royal Astronomical Society,* **31**, 341-359.

Zúñiga , R., and M. Wyss. (1995): "Inadvertent changes in magnitude reported in earthquake catalogs: Influence on *b*-value estimates". *Bulletin of the Seismological Society of America,* **85**, 1858-1866.

Chapter 4. Intermediate-Term Declines in Seismicity at Mt. Wrangell and Mt. Veniaminof Volcanoes, Alaska, Following the November 3, 2002, Mw 7.9 Denali Fault Earthquake[1]

4.1. Abstract

The Mw 7.9 Denali fault earthquake ruptured segments of the Susitna Glacier, Denali, and Totschunda faults in central Alaska providing a unique opportunity to look for intermediate-term (weeks to months) responses of active volcanoes to shaking from a large earthquake. The Alaska Volcano Observatory (AVO) monitors 24 volcanoes with seismograph networks. We examined one station per volcano; digitally filtered data for the period four weeks before to four weeks after the mainshock were plotted at a standard scale. Mt. Wrangell, the closest volcano to the epicenter (247 km), had a background rate of 16 events/day. For the following 30 days, however, its seismicity rate dropped by 50%. Mt. Veniaminof (1400 km from the epicenter) had a rate of 8 seismic events/day, but suffered a drop in seismicity by 80% after the mainshock; this may have lasted for 15 days. The seismicity at both volcanoes is dominated by long-period seismic events. With the exception of Martin and Novarupta volcanoes, the other 20 volcanoes showed no changes in seismicity attributable to the Denali fault earthquake. We conclude that the changes in seismicity observed are real, and are related to the Denali fault earthquake. These seismicity drops are in strong contrast to cases of short-term triggered seismicity increases observed at other volcanic systems such as Martin-Novarupta, Mt. Rainier, Yellowstone, Mammoth Mountain, and The Geysers, Coso and Cerro Prieto (Mexico) geothermal fields. This suggests that

[1] Sánchez, J. J. and S. R. McNutt (2005). Intermediate-Term Declines in Seismicity at Mt. Wrangell and Mt. Veniaminof Volcanoes, Alaska, Following the November 3, 2002, Mw 7.9 Denali Fault Earthquake, *Bull. Seism. Soc. Am.*, Vol **94**, No 6B, pp S370-S383.

fundamentally different mechanisms may be acting to modify seismicity at volcanoes.

4.2. Introduction

Earthquake-volcano interactions have been suggested because of reports of eruptions and increases in volcanic seismicity following large regional earthquakes (e.g. Linde and Sacks, 1998; Hill et al., 2002). In terms of triggering of seismicity in both volcanic and non-volcanic areas after distant earthquakes, the Mw 7.3 Landers, and the Mw 7.1 Hector Mine, California earthquakes settled the question when distinct increases in earthquake rates were reported at locations, as far as 1200 km from the epicenter of the Landers earthquake (Hill et al., 1993), and roughly 800 km in the case of the Hector Mine shock (Gomberg et al, 2001). On November 3, 2002 the Mw 7.9 Denali fault earthquake (DFE) ruptured along the Susitna Glacier, Denali, and Totshunda faults in Alaska, and again reports of triggered seismicity, this time at distances of at least 3800 km from the mainshock, were documented (Moran et al., 2005; Husen and Wiemer, 2005; Hill et al., 2003; Pankow et al., 2003; Hough et al., 2003; Eberhart-Phillips et al., 2003). Thus, at present there is no question that tectonic earthquakes do affect the activity at some volcanoes, and so far the reported observations have been of short-lived triggering of earthquakes that start during or immediately following the passage of seismic waves.

In broad terms, however, it is of interest to document both decreases and increases to provide constraints on source processes. In this paper we document intermediate-term (weeks to months) decreases in seismicity at Mt. Wrangell (MW) and Mt. Veniaminof (MV) following the DFE sequence (Fig. 4.1a). We make detailed comparisons of the rates of seismicity from four weeks

before to four weeks after the DFE and perform statistical tests for the significance of the changes. The seismicity rates are estimated by counting the numbers of local earthquakes on filtered and unfiltered seismograms from stations located close to the vents of the volcanoes. The catalog of located earthquakes for MW was also analyzed over a longer time scale. We then discuss the seismicity declines in terms of possible mechanisms, while recognizing that the study of these volcanoes is preliminary.

4.3. Data

The Alaska Volcano Observatory (AVO) monitors 24 volcanoes with seismograph networks and satellite imagery. Following the shaking from the DFE a detailed scan of filtered continuous seismic data was done for several stations at each of the 24 volcanoes to look for evidence of triggered local earthquakes. During the several hours that followed, the only clear evidence for triggering was found at Katmai National Park (Moran et al., 2005). Shishaldin volcano (distance ~ 1460 km from DFE), which has had sustained long-period seismic activity since the fall of 1999 (Petersen et al., 2002) showed no change within the first week of the DFE and then it experienced an increase in seismicity that we consider to be unrelated to the DFE (McNutt and Sánchez, 2003). Special attention was placed on MW because of its proximity to the DFE epicenter, but there were no confirmed changes during the first three days because of saturation by aftershocks. During the following days, however, a decline in the number of locatable events was observed, which could not be attributed to telemetry problems, because the stations operated normally following the DFE (Dixon et al., 2003). A similar decrease was noted at MV, which was undergoing an intense long-period earthquake swarm that lasted until March 2003. The observation that two volcanoes with ongoing high

seismicity rates experienced an unexpected response to the DFE prompted this paper.

MW and MV (Fig. 4.1), are located in different tectonic settings characterized by intracontinental right-lateral strike-slip that accommodates part of the oblique collision of the Yakutat block into southern Alaska (Plafker et al., 1994) (MW), and underthrusting due to the subduction of the Pacific plate beneath the North American plate (MV).

Seismicity at MW has been monitored since July 2000, when two seismograph stations were installed, and location of earthquakes began in August 2001, with the installation of two additional stations (Fig. 4.1b). This network is equipped with three L-4 Mark Products vertical-component seismometers having a 1 s natural period, and one L-22 Mark Products three-component seismometer having a 0.5 s natural period. The seismograph network at MV was deployed in the summer of 2001, but data archiving and recording began in February 2002. This network is composed of nine stations equipped with L-4 Mark Products vertical-component seismometers having a 1 s natural period. The detection thresholds for the seismograph networks at MW and MV have been estimated to be 0.9 and 0.7, respectively (Dixon et. al., 2003; McNutt, 2002).

The vast majority of earthquakes from MW and MV are long-period events (LP), whose occurrence is frequently associated with pressure variations inside fluid-filled conduits beneath the volcanoes (e.g. Aki et al., 1977; Koyanagi et al, 1987; Chouet et al, 1987; Gil-Cruz and Chouet, 1997). There have been no studies published previously analyzing the LP events at either volcano, and we infer, based solely on the waveforms and spectra, that the events are similar to LP events elsewhere. LP seismic events are characterized by emergent P-

waves, unclear or absent S-waves, and dominant frequencies in the range 1-5 Hz. Some of these events have been located at MW (Fig. 4.1b), because the high signal-to-noise ratio allows identification of first P arrivals (Fig. 4.2). We acknowledge, however, that the locations of these events shown in Figures 4.1b and 4.8a are preliminary because of the limited number of seismograph stations. LP seismic events at MV have not been located (Fig. 4.1c) because of their emergent arrivals (Fig. 4.2).

A second type of earthquake recorded at MW and MV are volcano-tectonic seismic events (VT) which typically occur in swarms and are attributed to slip on faults. VT events have clear P- and S-waves, a broadband spectrum usually in the range 5-15 Hz (Fig. 4.2), and magnitudes typically $\leq$ 2. VT seismic events are located in a conventional manner, using P and S arrival times for several seismograph stations.

4.4. Method

We band-pass filtered the continuous seismic data between 0.8 and 5 Hz at one station for each volcano, to eliminate surf noise and oceanic microseisms below 0.8 Hz and wind noise above 5 Hz. Data were then plotted at a standard scale used for AVO routine monitoring (Fig. 4.3). The plots thus generated will be referred henceforth as pseudohelicorder plots, to distinguish them from the unfiltered analog seismograms named helicorder records.

The criteria used to count earthquakes on pseudohelicorder plots are based on the amplitude and appearance of the waveforms. A signal is included if the amplitude is at least 250 counts and the waveform indicates a local source. The time scale in the pseudohelicorder plots is very compressed (Fig. 4.3), therefore a signal is rejected if it shows extended coda or an obvious S-P time. We used

the pseudohelicorder plots from stations WANC and VNNF, respectively (Fig. 4.1). To be certain that our results did not depend on processing artifacts, we also inspected analog helicorder records from stations WANC (MW) and VNSS (MV). In this case, the criteria used to count earthquakes are based on the amplitude, duration, S-P time, and appearance of the waveforms. A signal is included if the amplitude is $\geq$ 2.5 mm, the duration is > 10 s, and the S-P time is $\leq$ 3 s. If part of a daily record was unusable because of storm noise, aftershocks of the DFE, or data outages, we estimated the day total by multiplying the counts by the factor $24/U_H$, where U_H is the number of usable hours of record. Unusable days were assigned a value of zero. In the intermediate-term time scale of weeks to months, this does not affect our estimates of average seismicity rates. Also we note that there were some unusable days before the DFE, which also introduces low estimates balancing the counts on both time periods. To qualify the event counts we assigned scores depending on the amount of usable data. The scores range from A = good data, to D = unusable data. Table 4.1 shows the scoring scheme.

By assuming that the counts on any day are independent from the rest, we used the *z*-statistic (Habermann, 1987), a general parametric test to estimate the difference between two means. In our case the two means being compared are the averages of daily earthquake counts for the periods preceding and following the DFE. The formula for the *z*-statistic is

$$z = \frac{(M1 - M2)}{\sqrt{\frac{(S1)^2}{N1} + \frac{(S2)^2}{N2}}} \qquad (1)$$

where *M1*, *M2*: mean rates during the two periods (before and after the DFE); *S1*, *S2*: standard deviations; *N1*, *N2*: numbers of days in the sample. The *z*-

value represents the number of standard deviations from the mean of a normal distribution (i.e., $z = 1.64$ represents 90% significance, $z = 1.96$ represents 95% significance, and $z = 2.57$ represents 99% significance) and the sign of the z-value indicates the polarity of the change (i.e., $z < 0$ indicates rates increases, $z \approx 0$ indicates no change, and $z > 0$ indicates rate decreases). Usually a large sample size ($N_i > 30$) is used for the z-statistic (Crow et. al., 1960). At MW we have $N_i = 33$ for both pseudohelicorder plots and helicorder records, and $N_i = 94$ for located events. At MV we only analyze 15 days before to 15 days after the DFE. This sample size (N_i=15) although small, still allowed us to identify the differences in mean rates above random noise.

To detect significant changes in seismicity rates we also plot the cumulative sum of earthquakes versus time and find the z-values resulting from all possible divisions of the data in two halves. In this case the two samples under testing are only equal in size at the date of the DFE. The statistical tests were applied to the counts in the order they were obtained and also to multiple data sets obtained by random permutations of the observations.

4.5. Results

Visual inspection of pseudohelicorder plots from before to after the DFE provides a hint about the decreases in seismicity rates at the two volcanoes. Figure 4.3 shows 6-hour sections of typical pseudohelicorder plots before and after the DFE for stations WANC located on MW and VNNF located on MV; the differences in rates are quite obvious.

Plots of daily numbers of earthquakes versus time recorded at stations WANC and VNNF are shown in Figures 4.4a and 4.4b in discrete and cumulative forms, respectively. The counts shown on these figures are based

on pseudohelicorder plots and cover 66 days centered at the time of the DFE for station WANC, and 30 days for station VNNF. Under each cumulative sum we show the plot of *z*-values versus time. The difference in the seismicity rates at both stations from before to after the DFE is striking. The average counts at station WANC before and after the DFE are 15.5 and 8.3, respectively, and at station VNNF the averages are 7.7 and 1.4. By testing the counts in the order of the observations we found that the mean rates, from before to after the DFE, are different at least at the 99% confidence level at both WANC and VNNF stations (Fig. 4.4b). The *z*-values curve does not peak exactly at the date of the DFE, this reflects the fact that the seismicity rate changes happened in a gradual manner. To compare these results with a random distribution of the counts, we applied the same test to one hundred data sets generated by random permutation of the observations. We found the curves for the original data to be different from the random series.

Data in Figure 4.4a suggests that the rates of seismicity at MW and MV were in decline prior to November 3. We therefore also consider the rate decreases in this context and apply a logarithmic regression to the pre-DFE data in 4.4a and find the curves that best fit the apparent decays in seismicity prior to the DFE. We observe that during the immediate two weeks following the DFE, the best-fitting curves overestimate the seismicity rates. Prior to November 3 the regression curves underestimate the data. A statistical test of the sign of the residuals from figure 4.4a, based on a binomial distribution, shows that at MW the probability of finding a positive residual decreased from 0.45 to 0.30 from before to after the DFE. At MV the probability drops from 0.53 before the DFE to negligible values after the DFE. We see that the seismicity at both volcanoes dropped to lower levels than would be expected for an intrinsic decay and infer that the drops in seismicity resulted from a perturbation caused by the DFE. The

same procedure was applied to the counts from analog helicorder records and the results were stable.

At MW we also analyzed the catalog of located earthquakes on a longer time scale of one year. We used only located earthquakes with $M_L \geq 0.9$ and found that the drop in seismicity lasted for at least five months following the DFE (Fig. 4.5). This indicates that our results are robust and independent of the method used to estimate the seismicity rates.

Most volcanoes in Alaska showed no changes. Only two volcanoes in the Katmai area, Novarupta and Mt. Mageik, responded with short-lived bursts of small VT earthquakes during several hours following the DFE (Moran et al., 2005). Shishaldin volcano, located roughly 1460 from the DFE, showed no change immediately following the DFE, but its rates increased a week later. Because LP seismicity fluctuations at Shishaldin have been common over the past several years, we infer that this rate increase is unrelated to the DFE.

4.6. Discussion

4.6.1. Summary of Results

We carefully inspected filtered data for all 24 volcanoes seismically monitored by AVO. At two volcanoes: MW and MV, the average earthquakes rates dropped by approximately 50% and 80%, respectively, after the DFE and we estimated the differences in means from before to after the DFE to be significant at the 99% confidence level (Figs. 4.3, 4.4, and 4.5). The data are different from many randomly permuted series, in particular around the time of the DFE, and similar results were obtained when the seismicity rates were

estimated from unfiltered records or from the catalog of located earthquakes. We infer that this drop in seismicity is real and is related to the DFE.

Because earthquakes at volcanoes tend to occur in swarms, the daily seismicity rates can be underestimated if a swarm is hidden by noise. This might be true for short-lived swarms, but it does not apply to the elevated background rates that characterize MW or long-lived swarms that occur at MV. The occurrence of many LP events means that the source mechanisms at both volcanoes are likely fluid-driven, although this may be true of VT earthquakes as well. Based on the timing and polarity of the seismicity changes we infer that the DFE affected both volcanoes similarly.

4.6.2. Inferences on Mechanisms

We next examine the history and activity at the two volcanoes, to help determine the cause of seismicity decreases. We envision the plumbing systems of the two volcanoes as having open conduits with standing columns of water (MW) and magma (MV) through which gases percolate upwards causing seismic events. Under these conditions, candidates to decrease the seismicity rates include: choking off the supply of gas, widening the channel to change the flow conditions, opening new cracks to permit gas escape, and reopening pre-existing cracks.

4.6.2.1. Mt. Wrangell

Phreatic eruptions at MW occurred during the early twentieth century (Miller et al., 1998), but steaming is more common and an increase in heat flux has been documented since 1980 (Benson and Motyka, 1978; Benson and Follet, 1986). We infer that MW has a relatively unobstructed conduit. At some locations within the volcano, however, disturbances in the fluid flow may give

rise to pressure fluctuations that lead to LP seismicity (Chouet, 1996). At stratovolcanoes the disruption of the hydrothermal system caused by interactions between magma conduits and ground water may be a rich source of LP activity (Gil-Cruz et. al., 1987). Because of limited data and little previous research at MW or MV, the geometry and extent of their magma bodies and surrounding thermal anomalies are unknown. From the preliminary locations of LP events at MW and relative amplitudes among stations we infer that the sources of seismicity are close to the active vent (Fig. 4.1b).

We speculate that most LP earthquakes at MW result from interaction between hot rocks of the conduit and the surrounding hydrothermal system. When water is heated to the boiling point, the steam created generates overpressure in cavities and triggers oscillations that result in LP events. A first possible mechanism for the drop in the rate of LP events involves dynamic interaction between the passing waves of the DFE and the volcano. Peak accelerations at MW ranged between 0.18 and 0.34 g (NEIC, 2003), thus the shaking from the DFE may have created new cracks or opened old ones, by dislodging of sulfur salts or weathering products (Brodsky et al., 2003). This effect would allow overpressure to be released under low resistance, preventing the walls of cracks from oscillating, and hence decreasing the rate of LP events (Fig. 4.6a). Such a mechanism is also consistent with reduced ice and snow volumes at the summit of MW volcano following large earthquakes. Eyewitness accounts report increased emissions of steam and ash at MW after a large earthquake shook Yakutat Bay in September 3, 1899 (Benson and Motyka, 1978); melting ice and snow also suggested that the volcano warmed after the Mw 9.2 great Alaska earthquake in 1964 (Benson and Follet, 1986) and after the Mw 7.5 St. Elias earthquake of February 1979 (C. Benson, *Pers. Comm.,* 2003). Figure 4.6a shows a model for dynamic interactions between the passing waves of the DFE and MW.

We model the dilatational strains resulting from the DFE using the computer program Coulomb 2.5 (Toda et. al., 1998) (Fig. 4.7a). MW is located in a region of positive dilatational strains with values close to $2x10^{-5}$. Thus, an alternative mechanism for the decrease in seismicity involves sudden volumetric expansion resulting from the DFE. Here we speculate that when the pore pressure is high enough, water approaching the conduit is warmed, triggering the formation of bubbles or steam flashes that pressurize and set cavities into oscillations, and lead to LP activity at MW. If pore pressure decreases, water withdraws from the vicinity of the conduit, decreasing the rate of LP events. Because of the location of MW in the dilatational area of the DFE, we suggest that a drop in pore pressure in the MW area occurred as a result of the DFE, lasting for weeks or longer and decreasing the rate of LP events (Fig. 4.6b). Other large earthquakes that appear to have affected MW produced similar stress changes (Kanamori, 1970; Perez and Jacob, 1980).

4.6.2.1.1. Focal Mechanisms-Mt. Wrangell

We computed a composite fault-plane solution for VT earthquakes based on 41 reliable first motion readings, and used that information to investigate local stress changes on faults. To measure the coverage of first motion readings around the focus we used the station distribution ratio (STDR, Reasenberg and Oppenheimer, 1985). If STDR has a low value (STDR < 0.5), then a number of stations lie near the nodal planes of the solution, and thus the P-wave arrivals to these stations may be difficult to identify. The solution found at MW is consistent with thrust faulting and has STDR=0.51(Fig. 4.1b).

4.6.2.1.2. Coulomb Stress Changes-Mt Wrangell

Because of recent evidence for a correlation between stress changes, caused by large earthquakes or dike intrusions, and seismicity rate changes (e.g. Stein et. al., 1994; Toda et al., 2002; Toda and Stein, 2002) we computed Coulomb stress changes (ΔCFC) from the DFE on both optimally-oriented thrust faults and strike-slip faults at a depth of 5 km (mid-depth for VT hypocenters). The results show that MW is located in a region of negative ΔCFC ~ 0.02 bars (0.002 Mpa) for thrust faults (Fig. 4.7b). If the stress changes are projected on strike-slip faults, MW falls in a nodal region (Fig. 4.7c). We reproduced these results by modeling the changes in Coulomb stress using different values of fault slip, regional stress orientation, and target depth. These computations indicate that VT earthquakes at MW may have also been inhibited after the DFE.

4.6.2.1.3. Competing Processes-Mt. Wrangell

Competing processes may have occurred within MW after the DFE. We suggest that the opening of cracks acted to reduce pressure and inhibit seismicity, whereas rectified diffusion of water vapor into bubbles would act to increase pressure (Sturtevant et al., 1996; Brodsky et al, 1998), thus triggering seismicity (Fig. 4.6a). The outcome of the latter effect on the volcano should be apparent during a few days after the passage of the seismic waves from the DFE. Unfortunately, observation of seismic activity at MW in the 72 hours following the mainshock was impeded by saturation of the signal from aftershocks. We note that no eruptions at MW were detected on AVO satellite imagery. Because the seismicity at the volcano during the months that followed was lower than usual (Figs. 4.3-4.5) we suggest that the process inhibiting seismicity dominated.

4.6.2.2. Mt. Veniaminof

MV erupted in 1995 (Miller et al., 1998) and mild eruptions likely took place in 2002 (Global Volcanism Network, 2002). We suggest that the plumbing of MV may be represented by a semi-open system in which a standing column of magma resides in the conduit.

Because the distance between MV and the epicenter of the DFE is ~1400 km, the amplitudes of both dynamic and static strains are smaller than at MW. Indeed, the acceleration from the DFE in the MV area is estimated to be less than 0.002 g (NEIC, 2003) and the ΔCFC values are negligible (Fig. 4.7). Seismograms at MV in the 24 hours following the DFE were saturated by aftershocks and noise. We suggest, however, that no eruptions were triggered by the DFE because no activity at MV was detected on satellite imagery, and there were no reports of unusual activity at the volcano. Our data indicate that the overall seismicity at the volcano dropped by 80% during the two weeks following the DFE. We infer that the short duration of this decrease reflects the lesser effect that the dynamic strains had on the volcano. The available data allow us to see the change in seismicity, but the mechanism that could create the effect remains an open question.

4.6.2.2.1. Focal Mechanisms-Mt. Veniaminof

For MV individual fault-plane solutions were not analyzed because of the small number of VT earthquakes available. A composite fault-plane solution was obtained from 39 first-motion readings, with STDR=0.55. The solution is consistent with a thrust fault, with some strike-slip component (Fig. 4.1c).

4.6.2.2.2. Coulomb Stress Changes-Mt Veniaminof

Our Coulomb stress modeling places MV in a region of positive ΔCFC (encouraging failure) for optimally oriented thrust faults (Fig. 4.7b), or negative ΔCFC (inhibiting failure) for optimally oriented strike-slip faults (Fig. 4.7c). In both cases, however, the changes in the ambient stress field due to the static stress changes from the DFE are negligible because of the great distance to the DFE rupture.

4.6.3. Seismicity Changes Elsewhere

We observed decreases in seismicity at MW and MV, and little to no change in seismicity at other Alaskan volcanoes following the DFE. This is in stark contrast to multiple reports of short-term (hours to days) increases in seismicity elsewhere in the United States, including Yellowstone (Husen and Wiemer, 2005), Mt. Rainier (S. Malone, *written comm.,* 2002), The Geysers and Coso geothermal fields, Mammoth Mountain, Long Valley Caldera (Hill et al., 2003) and Cerro Prieto geothermal field in northwestern Mexico (R. Castro, *written comm.*, 2003). This implies that after a large tectonic earthquake occurs, fundamentally different mechanisms may act to modify activity at volcanoes. After the Mw 7.3 Landers, and Mw 7.1 Hector Mine, California earthquakes, seismicity increases were reported at volcanic and non-volcanic areas that were preferentially aligned along strike with the fault ruptures (Hill et al, 1993; Gomberg et al., 2001). Similarly, after the DFE most localities that responded with an increase in seismicity rates were concentrated along the azimuth of the rupture direction (Gomberg et al., 2004; Velasco et al., 2005) indicating that the directivity in the radiated energy during the DFE played a role in the triggering

mechanisms. In contrast, MW and MV volcanoes are located approximately perpendicular to the rupture direction, where the directivity effect is smaller.

Reports of cases of eruptions being inhibited by tectonic earthquakes are equally rare. Alvarado et al., (1992) postulate that the absence of eruptive activity at Poas volcano between 1980 and 1986, the increase in fumarolic temperatures at Miravalles geothermal field, and the appearance of new fumaroles on Irazú volcano may all have been related to tectonic seismicity located $\leq$ 200 km away. All these descriptions are consistent with a reduction in internal pressure of the volcanoes, similar to our postulated effects.

4.7. Conclusions

New data and observations indicate that systematic changes in seismicity at two volcanoes in Alaska, Mt. Wrangell and Mt. Veniaminof, took place on intermediate-term time scales of weeks (MV) to months (MW) following the DFE of November 3, 2002. Decreases in seismicity, mostly LP events, by more than 50% took place at the two volcanoes and lasted for at least five months at MW and for at least two weeks at MV. We infer that these changes are related to the DFE.

We conclude that key aspects of our observations of decreases in seismicity are: (1) the seismic activity at MW and MV volcanoes is dominated by LP events (hence fluid-driven processes), in contrast to the VT earthquakes (shear failure) that dominate in the cases of triggering, (2) MW and MV are located in a perpendicular direction in relation to the DFE rupture, in contrast to the preferential along-strike location in the cases of seismicity increases, and (3) the intermediate-time (weeks to months) duration of the declines in seismicity, in contrast to the short-lived (hours to days) durations of triggering elsewhere.

Our interpretation of the declines in seismicity at the volcanoes is presented in terms of decreases in pressure in postulated hydrothermal or magmatic systems. The causes of these decreases in pressure can be attributed either to dynamic interaction between the passing waves of the earthquake and the volcanoes, or to static stress changes; or to a combination of effects. The strong shaking at MW from the DFE may have created new cracks or reopened old ones, by dislodging sulfur deposits from the walls of the cracks. This would allow a release of accumulated pressure and subsequently decrease the rate of LP events. A static stress change is an alternative cause for a decrease in pressure. We speculate that a drop in pore pressure took place after the earthquake, such that water withdrew from the proximity of the magma or hot rocks of the conduits, thereby slowing the rate of LP events.

Because MW has not had recent eruptions, and steaming at its summit is common and prolific, we infer that its hydrothermal plumbing system is open, and that both dynamic and static interactions have acted there. MV, which has had recent mild eruptions and a somewhat elevated level of seismic activity, may be best represented by a semi-open system, in which a standing column of magma resides with gases percolating through it. At both volcanoes, mechanisms that induce short-lived seismicity increases may have acted too, competing with our proposed mechanisms to inhibit LP event generation. However, our data suggest that because of the duration of the reduction in seismicity, the effects of the inhibiting mechanisms prevailed.

Finally we conclude that it is important to examine *all* responses in volcanic activity following large earthquakes, because intermediate to long-term effects may be overlooked as a result of the increased awareness and expectations for short-term effects.

4.8. Acknowledgements

The authors wish to thank C. Benson for sharing his observations on changes at MW related to large tectonic earthquakes; S. Stihler for assistance with the locations of earthquakes at MW and Mt Veniaminof; R. Castro (CICESE, Mexico) for information on activity at Cerro Prieto geothermal field following the DFE; and G. Alvarado for information on changes in activity of volcanoes in Costa Rica following large earthquakes. This paper benefited from reviews by S. Sherburn, W. Marzocchi and C. Rowe. We also thank E. Brodsky, K. Felzer and J. R. Grasso for useful comments and discussion. This work was supported by the Alaska Volcano Observatory and the U.S. Geological Survey (USGS), as part of their Volcano Hazards Program, and by additional funds by the State of Alaska.

4.9. Figures

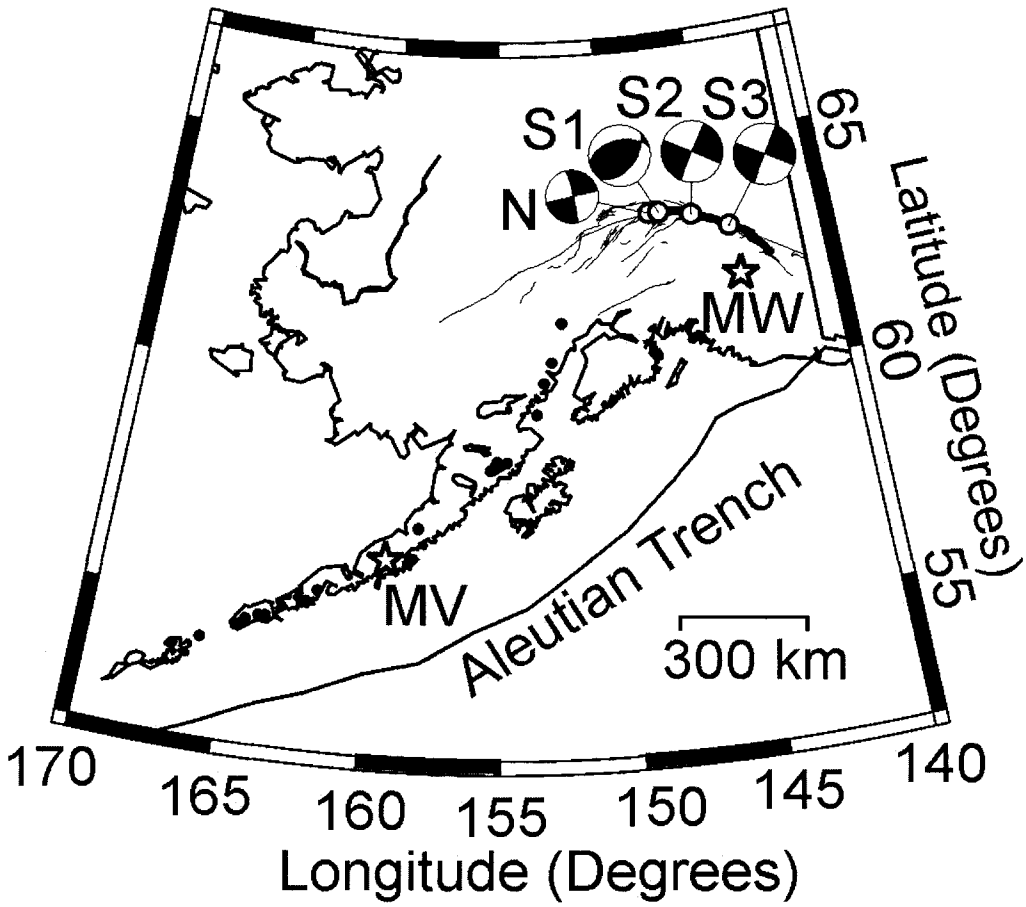

Figure 4.1a. Location maps for MW and MV. (a) Map of Alaska showing some of the main faults and tectonic structures (solid lines). Circles mark the locations of the October 23, 2002 Mw 6.7 Nenana Mt. earthquake (N) and the three subevents (S1 to S3) determined for the DFE, lower hemisphere projections with compressional areas in black. Thick black line marks the DFE rupture. Black circles mark the locations of volcanoes seismically monitored by AVO. Stars mark the locations of Mt. Wrangell (MW) and Mt. Veniaminof (MV) volcanoes.

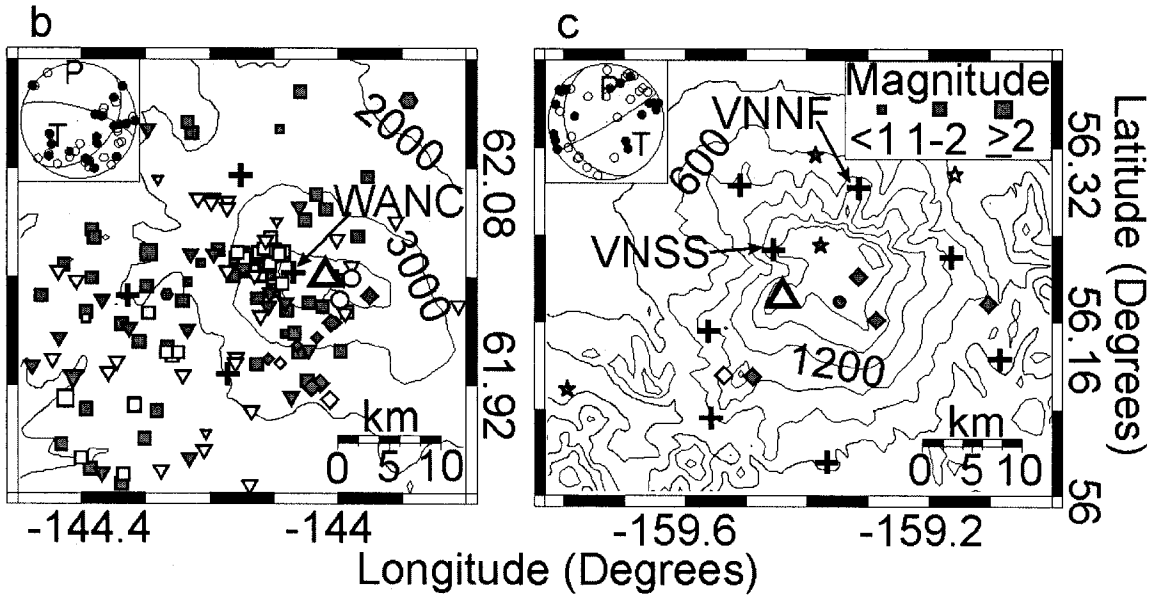

Figure 4.1. (Continued) Local maps of MW and MV. (b) Map of MW. Triangle marks the vent. Topographic contours are 1000 m. Crosses mark seismograph stations (only stations mentioned in the text are labeled for clarity). Locations of seismic events between June 4, 2002 and June 30, 2003 are shown. Gray symbols correspond to pre-DFE seismicity, white symbols represent post-DFE seismicity. Symbols are coded according to the type and depth of seismic event: LP seismic events: Hexagons (<0 km), squares (0 to 10 km), inverted triangles (>10 km); VT earthquakes: Circles (<0 km), diamonds (0 to 10 km), and stars (>10 km). Symbol size is proportional to magnitude. Inset shows composite fault-plane solution of VT earthquakes. Lower hemisphere projection. Hollow and filled circles represent dilatations and compressions, respectively. P and T mark the P- and T-axes. (c) Map of the MV area. Topographic contours are 300 m. Locations of seismic events between August 22, 2002 and January 15, 2003. Other conventions as in (b).

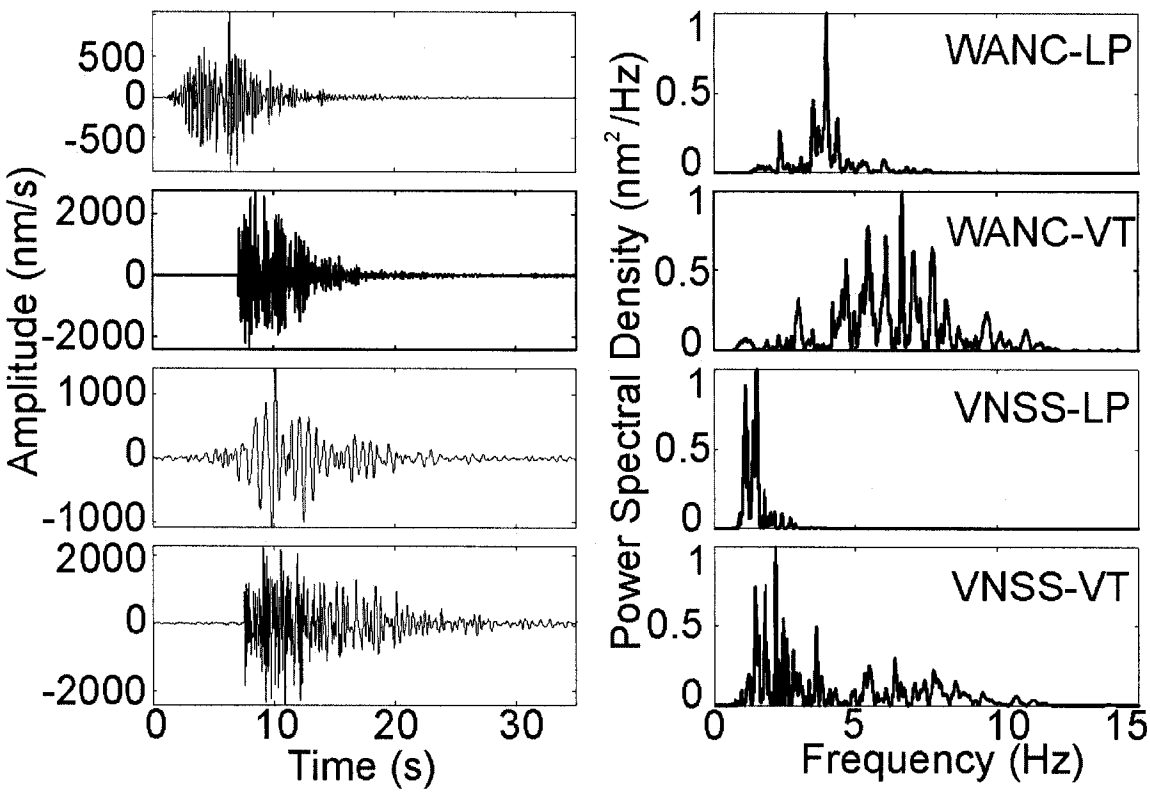

Figure 4.2. Typical waveforms at MW and MV. Top four panels: Typical seismograms (band-pass filtered between 0.8 and 5 Hz) and spectra of long-period (LP) and volcano-tectonic (VT) earthquakes recorded at station WANC on MW volcano.. Origin times (UT) are October 2, 2002 at 13:08, and October 27, 2002 at 12:11, respectively. Bottom four panels: Same as above for seismic events at station VNSS on MV volcano. Origin times (UT) are October 10, 2002, at 00:56, and October 30, 2002 at 4:11, respectively.

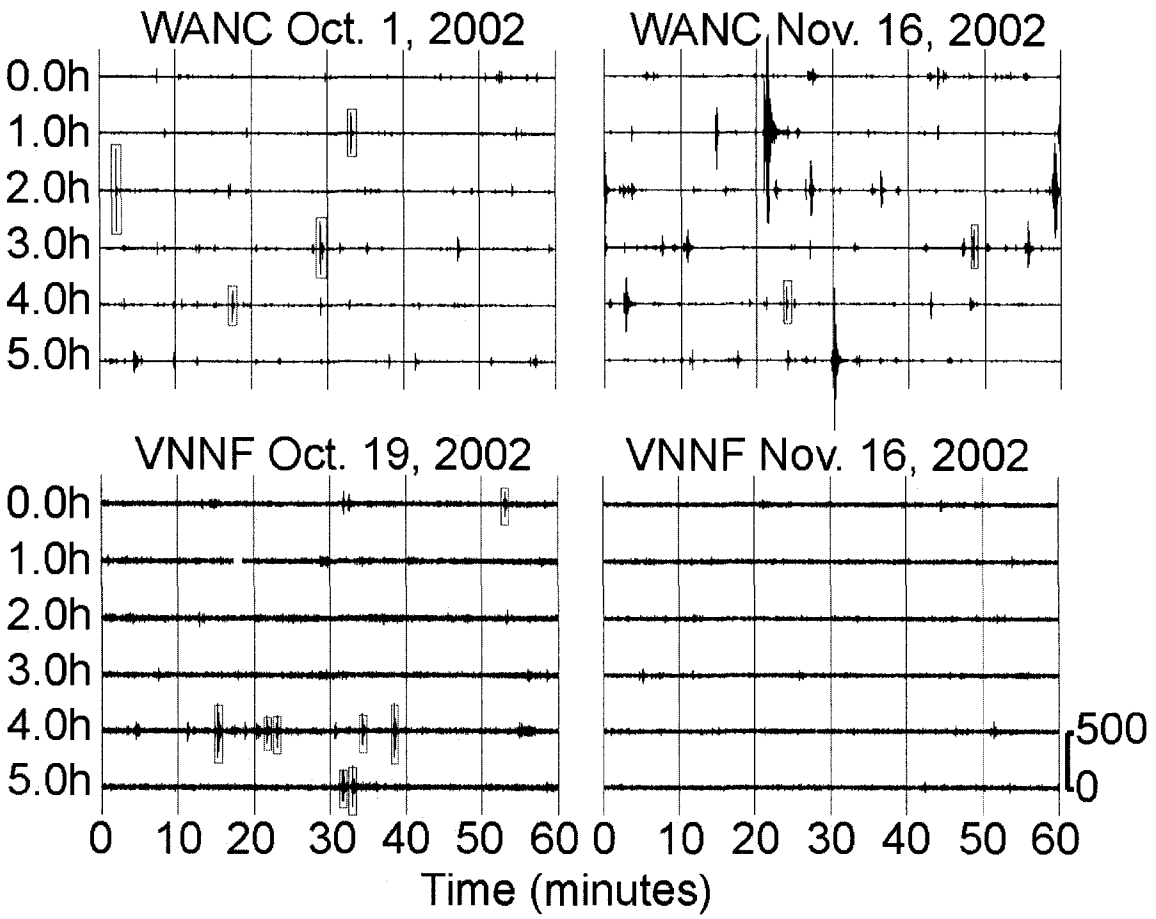

Figure 4.3. Seismicity before and after the DFE. (a) 6-hour long pseudohelicorder plot for station WANC, on MW volcano, October 1, 2002. Data are band-passed between 0.8 and 5 Hz. Earthquakes that meet the counting criteria are enclosed in boxes (see text). (b) Same as (a) for November 16, 2002. Large events are aftershocks of the DFE. (c) and (d) Pseudohelicorder plots for station VNNF on MV volcano, recorded on October 19, 2002 and November 18, 2002, respectively.

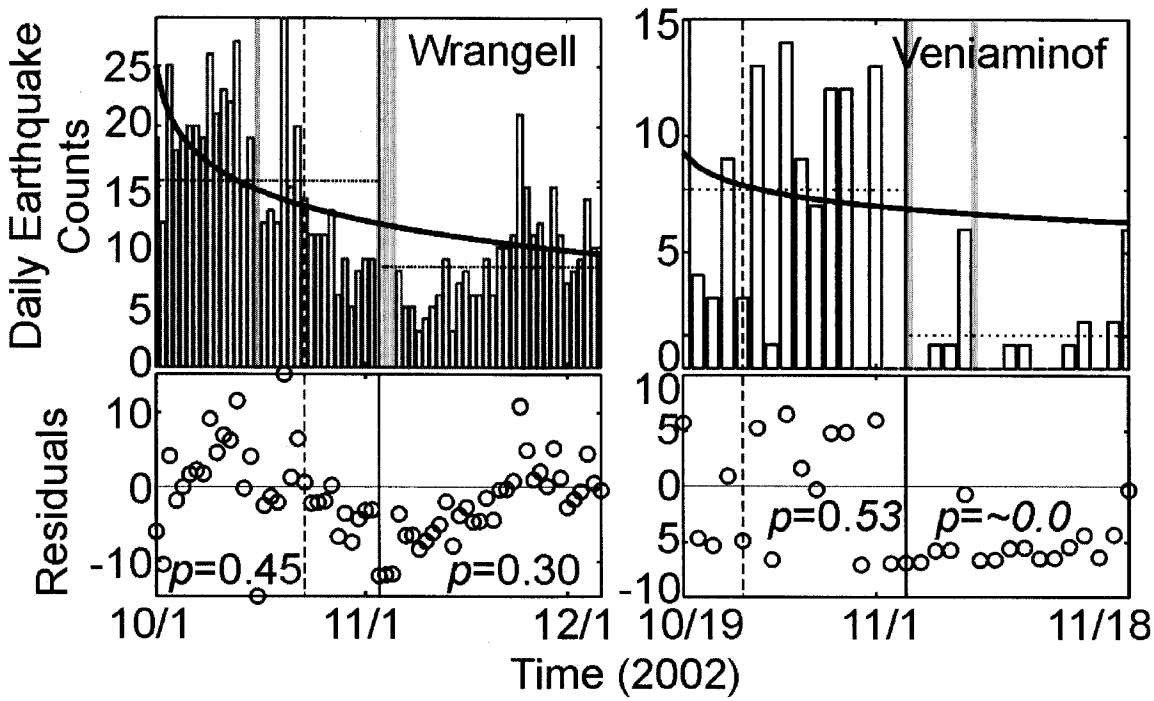

Figure 4.4a. Bar plot of pseudohelicorder counts. Left: Histogram of daily pseudohelicorder event counts at station WANC (top) on MW. The vertical solid line marks the DFE (November 3, 2002); a vertical dashed line to the left marks the Mw 6.7 Nenana Mountain earthquake (October 23, 2002). Horizontal dotted lines are the average counts before and after the DFE. A letter "u" marks the days during which the record was rendered useless because of noise or aftershocks. During all other days at least 6 hours of clear recording were available, mostly 21 hours or more (see Table 1). The thick black curve shows the logarithmic regression applied to the data prior to the DFE. The best-fit function is y = -3.7Ln(x) + 25, where y is the number of local earthquakes during any day and x is the time in days after September 30, 2002. The bottom panel shows the plot of residuals (data minus logarithmic fit). The values indicated for *p* are the probabilities of finding a positive residual before and after the DFE. Right: same as above for the pseudohelicorder counts at station VNNF on MV. The best-fit function is: y = -0.9Ln(x) + 9.

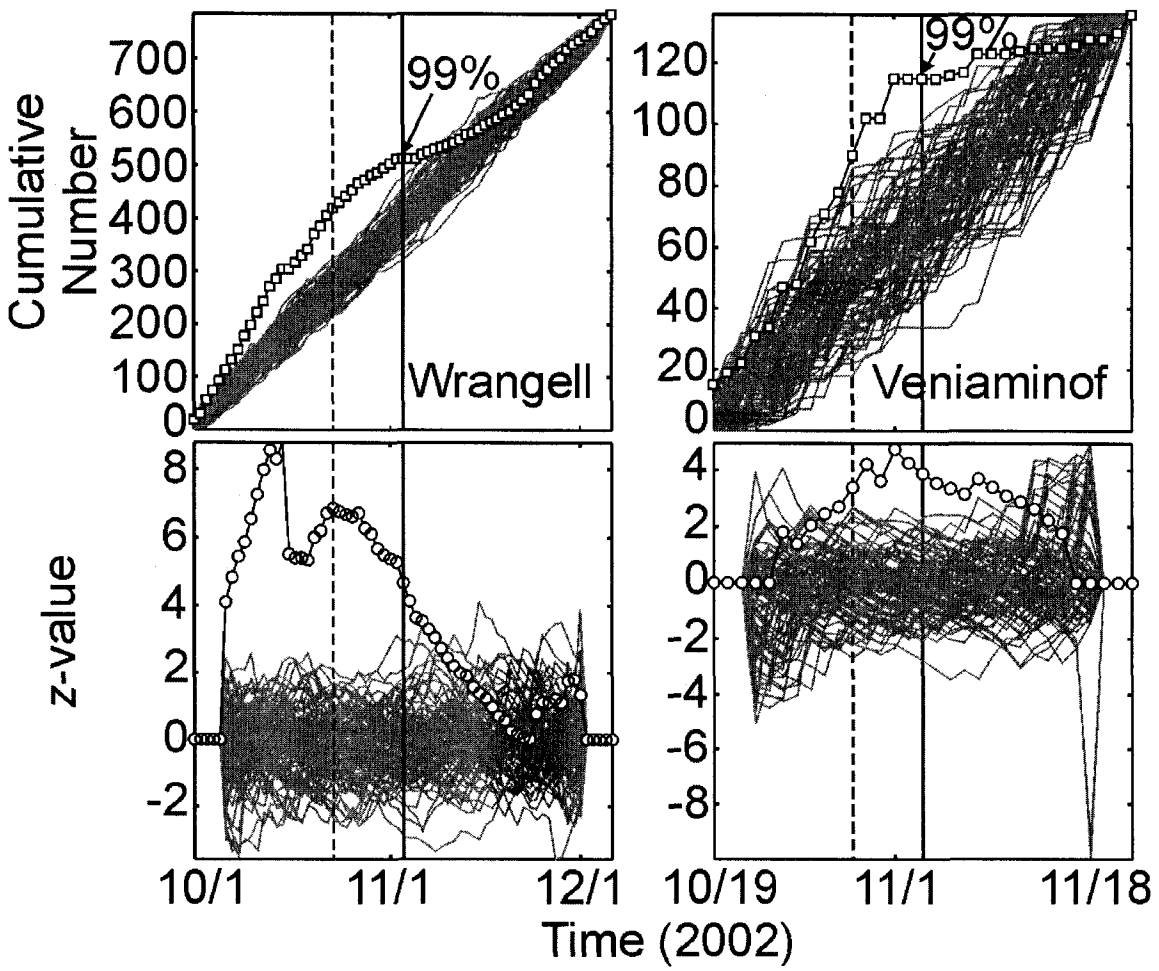

Figure 4.4b. Cumulative sum of counts versus time. Left: Cumulative form of the data shown in (a) for station WANC on Mt. Wrangell. The bottom part shows the plot of *z* values versus time. In both plots, cumulative numbers and *z* values, lines with symbols represent the ordered data and lines without symbols represent 100 random permutations. The percentages shown indicate the confidence levels at which the two means, before and after the DFE, are different as evaluated by the *z*-test. Other conventions as in (a). Right: Same as above for station VNNF, on MV.

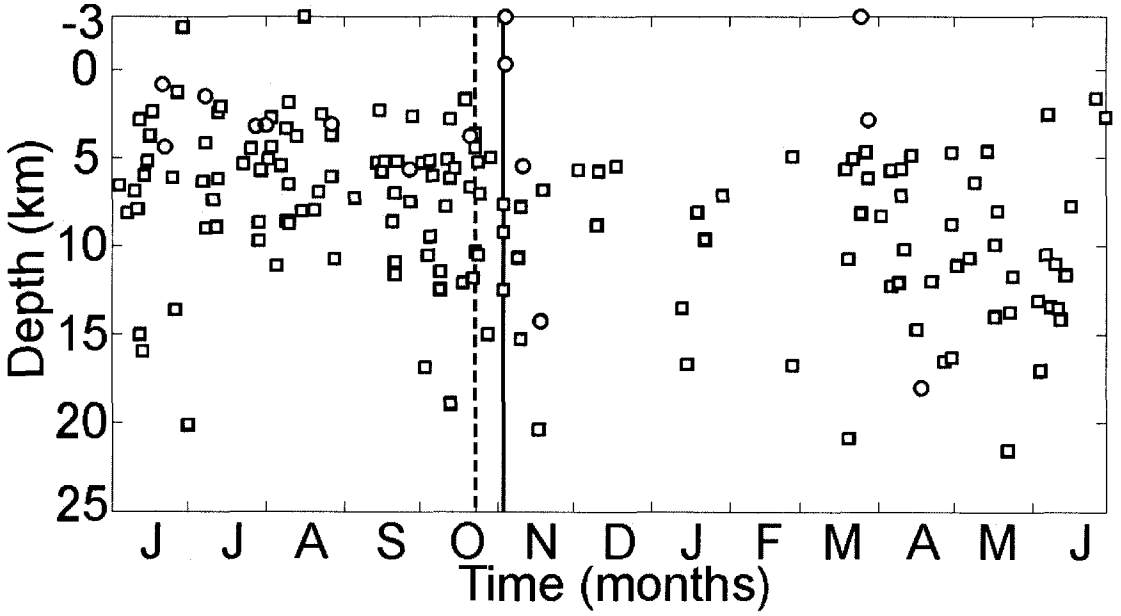

Figure 4.5a. Seismicity versus time at MW. (a) Depth versus time plot for located earthquakes with magnitude $\geq$ 0.9 at MW between June 2002 and June 2003. Negative depths correspond to locations above sea level. Squares and circles mark LP and VT earthquakes, respectively. Note the decrease in seismicity after the DFE, which persisted at least until early March 2003. Other conventions as in Figure 4.4.

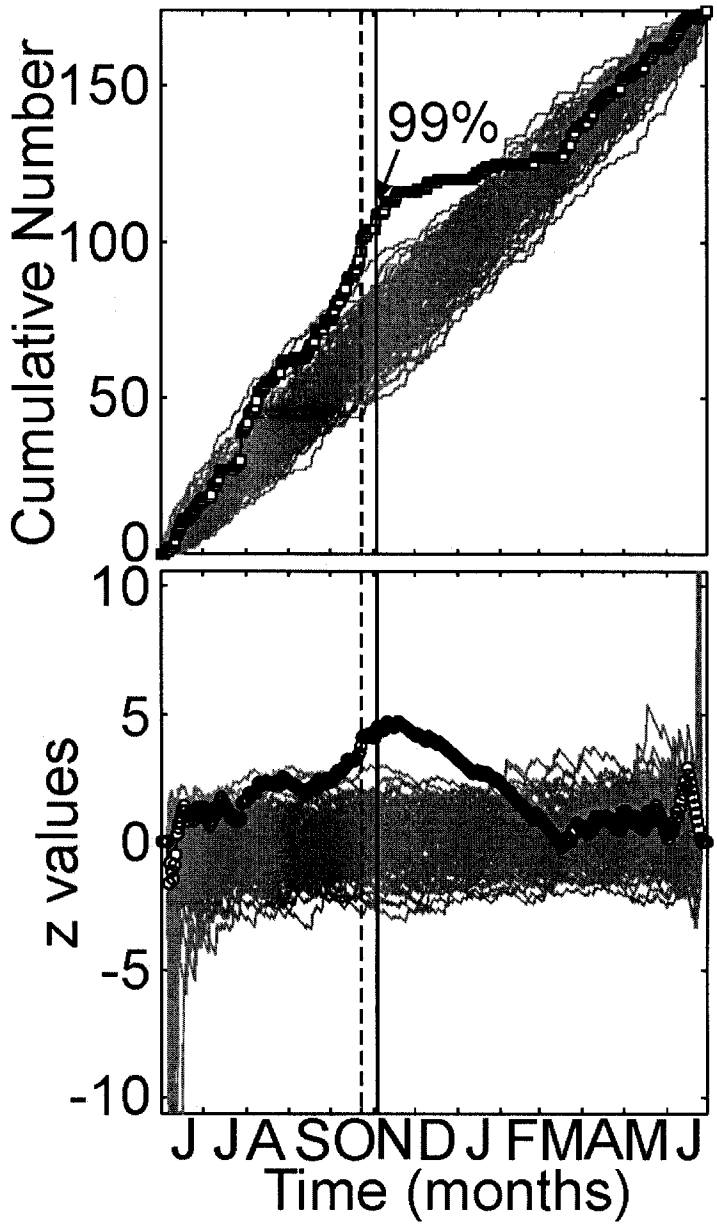

Figure 4.5b. Located earthquake counts at MW. Top: Cumulative sum of daily counts of located earthquakes at MW. The decline in seismicity following the DFE is found here at the 99% confidence level. Bottom: Plot of *z*-values versus time. Other conventions as in Figure 4.4b.

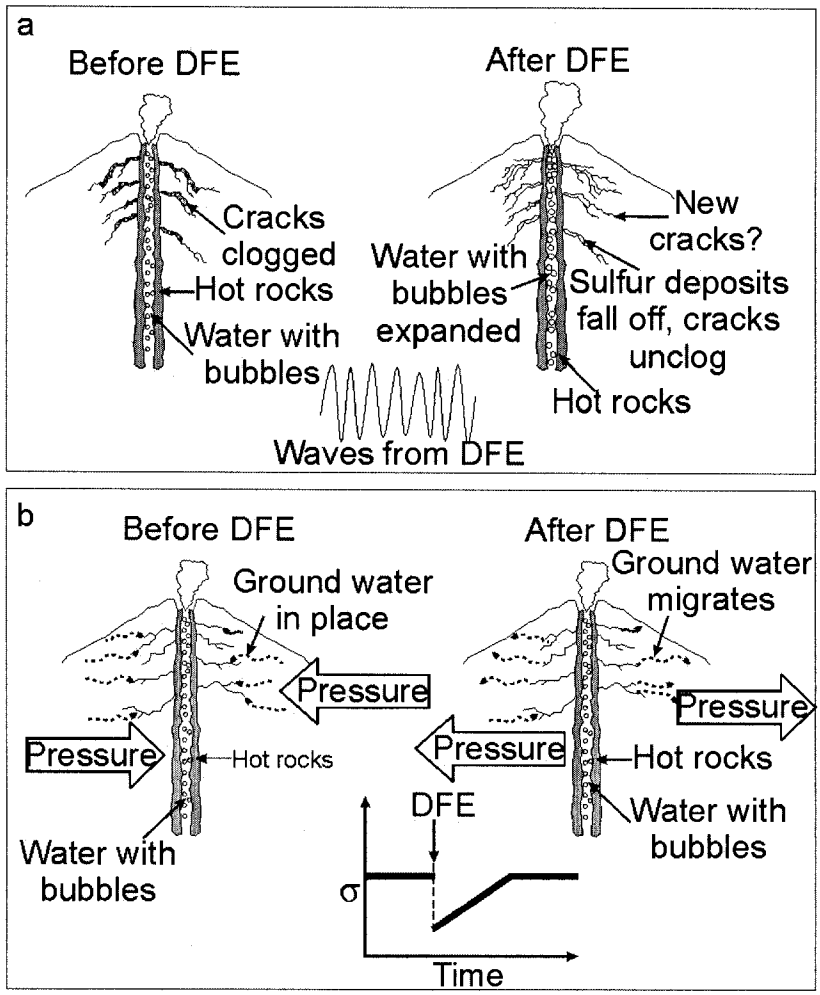

Figure 4.6. Earthquake-volcanoes interactions. (a) Sketch, not to scale, of a hypothetical scenario in which MW and its plumbing system are affected by the dynamic stresses of the passing waves from the DFE. The plumbing system is represented by a conduit with hot rocks (shaded areas), a standing column of water with bubbles in it, and cracks at shallow levels. Some pre-existing cracks are clogged by sulfur deposits (hatched areas), the cracks become unclogged because of the strong shaking, and possibly new cracks are formed. Circles represent bubbles in water. (b) Same as (a) but here the plumbing system of the volcano is affected mostly by a static stress change (decompression) after the earthquake. Ground water (dotted arrows) is in contact with the hot rocks of the conduit, under certain background pressure (large horizontal arrows). After the DFE, a sudden decompression occurs and the pressure falls below background, allowing some of the water to withdraw. After the decompression caused by the DFE, the loading gradually recovers to its original level, allowing the seismicity to return to pre-DFE rates (see also Figure 4.5a.).

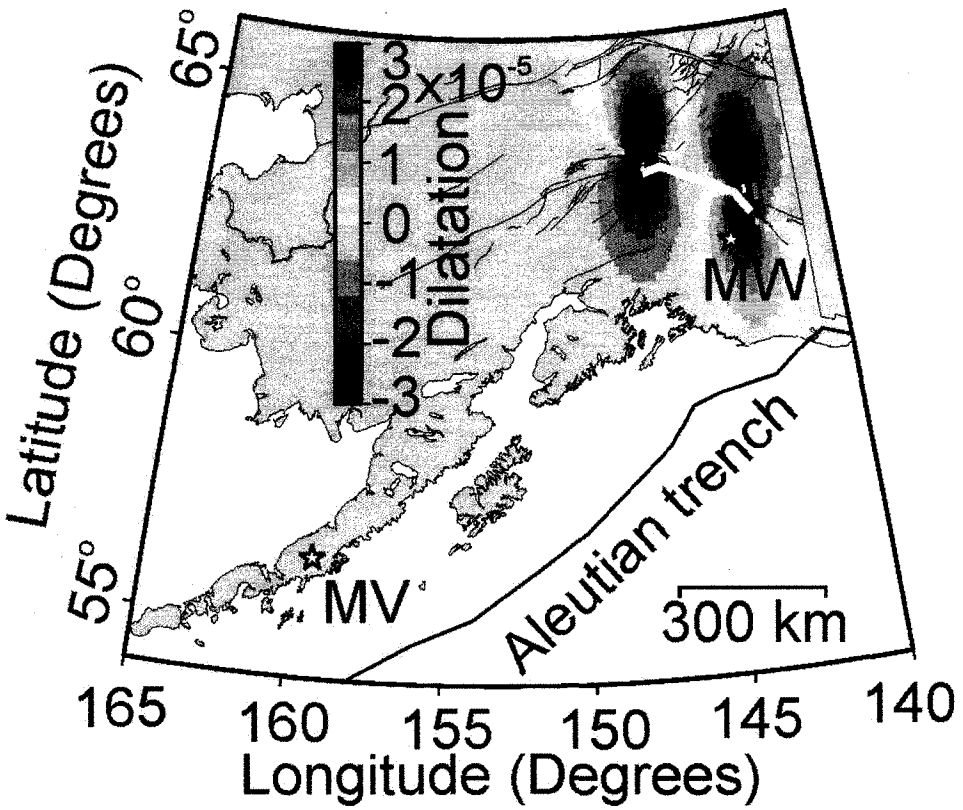

Figure 4.7a. Static stress changes. Dilatational strain at a depth of 5 km resulting from the DFE. Thick white lines represent the faults that ruptured during the DFE sequence (Susltna Glacier, Denali, and Totschunda faults). The amount of slip in meters and dip angle assigned to each of the three faults is (right-lateral slip, reverse slip, dip): Susitna Glacier=(1 m, 2.5 m, 48°), Denali = (6 m, 0 m, 90°), and Totschunda = (2 m, 0 m, 90°). The fault depth range is 0-18 km and regional maximum principal stress was oriented (azimuth clockwise from north/dip) σ_1=150°/0°. Red colors represent dilatation, blue colors represent compression. Other conventions as in Figure 4.1a.

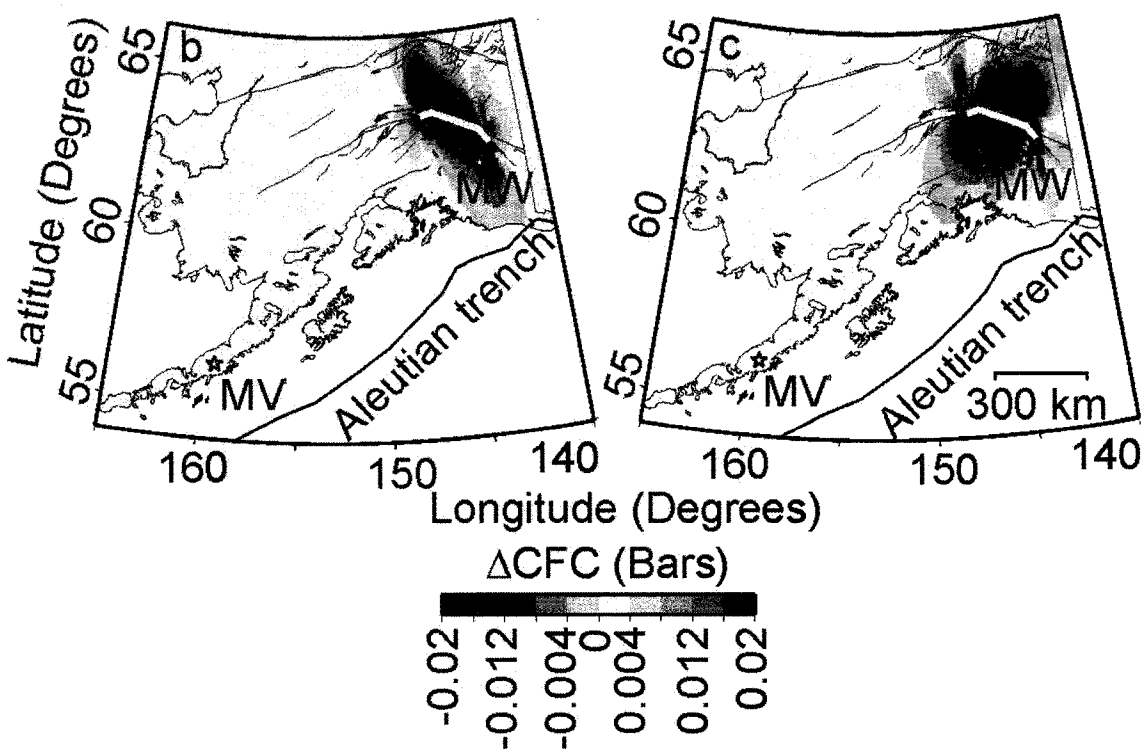

Figure 4.8. (continued). Change in Coulomb stress. (b) Change in Coulomb stress computed for optimally oriented thrust faults (target depth = 5km) as a result of the DFE. The values of friction coefficient, Poisson's ratio, and Young's Modulus used were: 0.4, 0.25, and $8x10^5$ bars, respectively. Red colors indicate positive change in Coulomb stress (encouraging failure) and blue colors negative (inhibiting failure). Other conventions as in (a). (c) Same as (b) for optimally oriented strike-slip faults.

4.10. Tables

Table 4.1. Rating Criteria for Data Quality

			Number of Days Within this Category			
			Pseudohelicorder		Helicorder	
Score	P (% of usable record)	Description	VNNF	WANC	VNSS	WANC
A	$P \geq 90$	Good	14	51	22	27
B	$60 \leq P < 90$	Fair	10	7	6	8
C	$25 \leq P < 60$	Regular	5	5	3	19
D	$P < 25$	Unusable	2	4	0	13

4.11. References

Aki, K., M. Fehler and S. Das (1977). Source mechanism of volcanic tremor: Fluid-driven crack models and their application to the 1963 Kilauea eruption, *J. Volcanol. Geotherm. Res.* **2,** 259-287.

Alvarado, G. E., M. Fernandez, R. Barquero, H. Flores and G. J. Soto, (1992). Aborted eruptions triggered by earthquakes?, *EOS*, **73**, 194.

Benson, C. S. and A. B. Follet (1986). Application of photogrammetry to the study of volcano-glacier interactions on Mount Wrangell, Alaska, *Photogrammetric Engineering and Remote Sensing* **52**, 813-827.

Benson, C. S. and R. J. Motyka (1978). Glacier-volcano interactions on MW, Alaska, *University of Alaska, Geophysical Institute, Annual Report 1977-78*, 1-25.

Brodsky, E. E., B. Sturtevant and H. Kanamori (1998). Earthquakes, volcanoes, and rectified diffusion, *J. Geophys. Res.* **103,** 23827-23838.

Brodsky, E. E., E. Roeloffs, D. Woodcock, I. Gall and M. Manga (2003). A mechanism for sustained groundwater pressure changes induced by distant earthquakes, *J. Geophys. Res.* **108,** 10.1029/2002JB002321.

Chouet, B. (1996). Long-period volcano seismicity: its source and use in eruption forecasting, *Nature* **380,** 309-316.

Chouet, B., R. Y. Koyanagi and K. Aki (1987). Origin of volcanic tremor in Hawaii, part II. Theory and discussion, in *Volcanism in Hawaii*, R. W.

Decker, T. L. Wright and P. H. Stauffer (Editors), *U.S. Geol. Survey Profess. Pap. 1350,* 1259-1280.

Crow, E. L., F. A. Davis and M. W. Maxfield (1960). *Statistics Manual*, Dover Publications, Inc. New York.

Dixon, J. P., S. D. Stihler, J. A. Power, G. Tytgat, S. C. Moran, J. Sánchez, S. Estes, S. R. McNutt and J. Paskievitch (2003). Catalog of earthquake hypocenters at Alaskan volcanoes: January 1 through December 31, 2002, U. S. Geol. Sur. Open-File Rept. 03-267, 58 pp.

Dixon, J. P., J. A. Power and S. D. Stihler (2003). Seismic monitoring of Alaska's volcanoes: A comparison of event detection with IASPEI and Earthworm acquisition systems, *EOS* 84, 1135.

Eberhart-Phillips, D., P. Haeussler, J. T. Freymueller, A. D. Frankel, C. M. Rubin, P. Craw, N. A. Ratchkovski, G. Anderson, G. A. Carver, A. J. Crone, T. E. Dawson, H. Fletcher, R. Hansen, E. L. Harp, R. A. Harris, D. P. Hill, S. Hreinsdóttir, R. W. Jibson, L. M. Jones, R. Kayen, D. K. Keefer, C. F. Larsen, S. C. Moran, S. F. Personius, G. Plafker, B. Sherrod, K. Sieh, N. Sitar, W. K. Wallace (2003). The 2002 Denali fault earthquake, Alaska: a large magnitude, slip-partitioned event, *Science* **300**, 1113-1118.

Gil-Cruz, F., H. J. Meyer, B. A. Chouet and D. Harlow (1987). Observations of long-period events and tremor at Nevado del Ruiz volcano 1985-1986, *Hawaiian Symposium on How Volcanoes Work*, Hilo, Hawaii, January 19-25, 1987.

Gil-Cruz, F. and B. Chouet (1997). Long-period events, the most characteristic seismicity accompanying the emplacement and extrusion of a lava dome in Galeras Volcano, Colombia, in 1991, *J. Volcanol. Geotherm. Res.* **77,** 121-158.

Gomberg, J., P. A. Reasenberg, P. Bodin and R. A. Harris (2001). Earthquake triggering by seismic waves following the Landers and Hector Mine earthquakes, *Nature* **411,** 462-466.

Gomberg, J., P. Bodin, K. Larson and H. Dragert (2004). Earthquake nucleation by transient deformations caused by the M=7.9 Denali, Alaska, earthquake, *Nature* **427**, 621-624.

Global Volcanism Network (2002). Volcanic Activity Reports Bulletin of the Global Volcanism Network, Smithsonian Institution, *BGVN* **27**,10.

Habermann, R. E. (1987). Man-made changes of seismicity rates, *Bull. Seismol. Soc. Am.* **77,** 141-159.

Harvard-CMT (2002). Harvard University Centroid-Moment Tensor Project web page, *http://www.seismology.harvard.edu/CMTsearch.html.*

Hill, D. P., F. Pollitz and C. Newhall (2002). Earthquake-volcano interactions, *Physics Today* 55, 41-47.

Hill, D. P., S. Prejean, D. Oppenheimer, A. M. Pitt, S. D. Malone and K. Richards-Dinger (2003). Activity remotely triggered in volcanic and geothermal centers in California and Washington by the 3 November, 2002 Mw=7.9 Alaska earthquake, *EOS* **84,** 1723.

Hill, D. P., P. A. Reasenberg, A. Michael, W. J. Arabaz, G. Beroza, D. Brumbaugh, J. N. Brune, R. Castro, S. Davis, D. dePolo, W. L. Ellsworth, J. Gomberg, S. Harmsen, L. House, S. M. Jackson, J. S. Johnston, L. Jones, R. Keller, S. Malone, L. Munguia, S. Nava, J. C. Pechmann, A. Sanford, R. W. Simpson, R. B. Smith, M. Stark, M. Stickney, A. Vidal, S. Walter, V. Wong and J. Zollweg (1993). Seismicity remotely triggered by the Magnitude 7.3 Landers, California earthquake, *Science* **260,** 1617-1623.

Hough, S., J. Gomberg and K. Hutton (2003). Remotely triggered earthquakes in southern California?, *EOS* **8**4, 1724.

Husen, S., and S. Wiemer (2005). Remotely Triggered Seismicity in the Yellowstone National Park Region by the 2002 Mw=7.9 Denali Fault Earthquake, Alaska. *Bull. Seismol. Soc. Am.* **94**, S317-S331.

Kanamori, H. (1970). The Alaska, earthquake of 1964: radiation of long-period surface waves and source mechanism, *J. Geophys. Res.* **75,** 5029-5040.

Koyanagi, R. Y., B. Chouet and K. Aki (1987). Origin of volcanic tremor in Hawaii, part I. Data from the Hawaiian Volcano Observatory 1969-1985, in *Volcanism in Hawaii,* R. W. Decker, T. L. Wright and P. H. Stauffer (Editors), *U.S. Geol. Survey Profess. Pap. 1350,* 1221-1257.

Linde, A. T. and S. I. Sacks (1998). Triggering of volcanic eruptions, *Nature* **395,** 888-890.

McNutt, S. R. (2002). Seismology: The state of knowledge of the Aleutian arc, 2002. 3rd *Biennal Workshop on Subduction Processes Emphasizing the Kurile-Kamchatkan-Aleutian Arc*, Fairbanks, Alaska, 9-15 June, 2002.

McNutt, S. R., and J. J. Sánchez (2003). Intermediate-term declines in seismicity at two volcanoes in Alaska following the Mw 7.9 Denali fault earthquake, *EOS* **84, 1723**.

Miller, T. P., R. G. Mcgimsey, D. F. Richter, J. R. Riehle, C. J. Nye, M. E. Yount and J. A. Dumoulin (1998). Catalog of the historically active volcanoes of Alaska, *U.S. Geol. Sur. Open-File Rept.* **98-582**, 104 pp.

Moran, S. C., J. A. Power, S. D. Stihler, J. J. Sánchez and J. Caplan-Auerbach (2005). Earthquake triggering at Alaskan volcanoes following the November 3, 2002, Denali fault earthquake, *Bull. Seismol. Soc. Am.* **94**, S300-S309.

NEIC-National Earthquake Information Center World Data Center for Seismology (2003). U.S. Geological Survey web page, *http://neic.usgs.gov/neis/poster/2002/20021103.html.*

Pankow, K., L., S. J. Nava, J. C. Pechmann and W. J. Arabaz (2003). Triggered seismicity in Utah from the November 3, 2002, Denali fault earthquake, *EOS* **8**4, 1724. *Bull. Seismol. Soc. Am.* **94**, S332-S347.

Perez, O. J. and K. H. Jacob (1980). St. Elias, Alaska, earthquake of February 28, 1979: tectonic setting and precursory seismic pattern, *Bull. Seismol. Soc. Am.* **70,** 1595-1606.

Petersen, T., Caplan-Auerbach J., and S. R. McNutt (2002). Temporal distribution and rates of repetitive low-frequency earthquakes at Shishaldin volcano, Alaska, *EOS* 83, 1484.

Plafker, G., L. M. Gilpin and J. C. Lahr (1994). Neotectonic map of Alaska, in *Geology of Alaska, Geology of North America*, G. Plafker and H. C. Berg (Editors), v. G-1, plate 12, 1 sheet, 1:2,500.000 scale.

Reasenberg, P. A. and D. Oppenheimer (1985). FPFIT, FPPLOT, and FPPAGE: FORTRAN computer programs for calculating and displaying earthquake fault-plane solutions, *U.S. Geol. Sur. Open-File Rept.* 85-739, 25 pp.

Stein, R. S., G. C. P. King and J. Lin (1994).Stress triggering of the 1994 M=6.7 Northridge, California, earthquake by its predecessors, *Science* **258**, 1432-1435.

Sturtevant, B., H. Kanamori and E. E. Brodsky (1996). Seismic triggering by rectified diffusion in geothermal systems, *J. Geophys. Res.* **101,** 25269-25282.

Toda, S., R. S. Stein and T. Sagiya (2002). Evidence from AD 2000 Izu islands earthquake swarm that stressing rate governs seismicity, *Nature* **419,** 58-61.

Toda, S., and R. S. Stein. (2002). Response of the San Andreas fault to the 1983 Coalinga-Nuñez earthquakes: An application of interaction-based probabilities for Parkfield, *J. Geophys. Res.* **107,** 10.1029/2001JB000172.

Toda, S., R. S. Stein, P. A. Reasenberg and J. H. Dieterich (1998). Stress transferred by the 1995 Mw=6.9 Kobe, Japan, shock: effect on aftershocks and future earthquake probabilities, *J. Geophys. Res.* **103,** 24543-24565.

Velasco, A., C. J. Ammon, J. Farrel and K. Pankow (2005). Rupture directivity of the November 3, 2002 Denali earthquake determined from surface waves, *Bull. Seismol. Soc. Am.* **94**, S293-S299.

Chapter 5. Unexpected Response of Mt. Wrangell Volcano, Alaska, to the Shaking from a Large Regional Earthquake: a Puzzle for Intermediate-Term Earthquake-volcanoes Interactions[1]

5.1. Abstract

On November 3, 2002 three segments of the Denali fault in interior Alaska ruptured during an Mw 7.9 earthquake, offering a unique opportunity to study earthquake-volcano interactions. Among the 24 volcanoes that are seismically monitored by the Alaska Volcano Observatory (AVO), Mt. Wrangell, is the closest volcano to the epicenter (247 km) and showed the clearest response to the shaking in the intermediate-term (weeks to months) time scale. The response was unexpected because it consisted of a decline by at least 50% in the volcano's seismicity rate (mostly low-frequency events) that lasted for five months. Because previous well-documented instances of short-term (minutes to days) responses of volcanic centers to the passing waves of distant earthquakes have all been seismicity increases, the decline in seismicity at Mt. Wrangell poses a controversial puzzle. By using several independent methods to measure the seismicity rate at the volcano from before to after the mainshock, and applying rigorous statistical testing, we conclude that the change in seismicity at the volcano was a real effect of the Denali earthquake and that the volcanic seismicity at Wrangell did not fully recover to pre-Denali rates as of June 2003. We suggest that a depressurization of the volcanic plumbing system took place either as a result of sudden decompression (static stress changes) or because of creation of new pathways resulting from the

[1] Sánchez, J. J. and S. R. McNutt. Unexpected response of Mt. Wrangell volcano, Alaska, to the shaking from a large regional earthquake: a puzzle for intermediate-term earthquake-volcanoes interactions, Article in Press, *Earth Sciences Research Journal.*

strong shaking (dynamic stresses). At present we cannot distinguish between these two possibilities.

5.2. Introduction

The interactions between earthquakes and volcanoes have been a subject of scientific interest for many years and recently a topic of active research thanks to the increasing number of reports and the improvement of precise instrumentation. The link between tectonic and volcanic activity is better understood by considering the scales of time and space: at very long times (hundreds to millions of years) and large distances (tens of thousands of kilometers) the connection is explained under the theory of plate tectonics and one only needs to glance at a map of global tectonics to see that the distributions of earthquakes and volcanoes are not the result of mere coincidence.

In the very short time scale of minutes to days and distances of kilometers to tens of kilometers, there are numerous documented cases of eruptions following the shaking from large earthquakes. Such interactions are exemplified by the 1975 summit eruption of Kilauea volcano 1.5 hours after the Ms 7.5 Kalapana earthquake (Tilling et al., 1976) and the eruption of Cordon Caulle volcano two days following the magnitude Mw 9.5 1960 Chile earthquake (Gerlach et al., 1988). In the intermediate-term scale of weeks to months or years, new evidence and research points towards a positive link, meaning that a regional earthquake with Mw 6.5 or larger can trigger unrest at volcanoes located several hundreds of kilometers away (Hill et al., 2002).

In all instances of earthquake-volcano interactions, all observations indicate that a distant earthquake is able to cause changes in activity at volcanic (and

non-volcanic) areas in terms of eruptions or increases in seismicity. The opposite effect, however, has not been clearly observed and the literature, with only a few exceptions (Alvarado, et al., 1992; McNutt and Sánchez, 2002; Sánchez and McNutt, 2005), does not include documentation of eruptions at volcanoes being *inhibited* or seismicity rates being *decreased* by either the transient or permanent changes induced by a distant earthquake.

In November 2002, the Mw 7.9 Denali Fault Earthquake (DFE, Figure 5.1) caused short-lived seismicity increases at volcanic areas located along the rupture direction to distances as far as 3660 km from the epicenter (Eberhart-Phillips et al., 2003) and a clear intermediate-term drop in the seismicity at Mount Wrangell (MW) volcano, located in the perpendicular direction with respect to the rupture and roughly 240 km away from the epicenter. This effect may have lasted for five months. The same type of seismicity drop, with duration of roughly two weeks, was detected at Mount Veniaminof (MV), located ~1400 km from the DFE (Sanchez and McNutt, 2005).

In this paper we provide evidence, by means of statistical testing, that the decline in seismicity observed at MW was real and can be attributable to the DFE. To do so, we analyze the catalog of located volcanic earthquakes compiled by the Alaska Volcano Observatory (Dixon et al., 2003a, 2004) and test it for the significance of the changes following the DFE. We focus on Mt. Wrangell because the duration of the decline in seismicity at Mt. Veniaminof was shorter and the LP seismicity has not been located there.

5.3. Data

The Alaska Volcano Observatory (AVO) has monitored the seismic activity at MW since July 2000 (Fig. 5.1), when two local seismograph stations were

installed. Locations of earthquakes were possible beginning August 2001, when two additional stations were deployed. From August 2001 to March, 2003, 5451 events triggered the automatic detection system, but only 508 could be located (Figure 5.2). The reason for this low detected/located ratio stems from a combination of low signal-to-noise ratio, limited number of seismograph stations and most important of all, the characteristics of the first arrivals of the earthquakes at the different stations. Of all located earthquakes, 86.4% have been identified as long-period seismic events (LP). LP events show emergent first arrivals to the seismograph stations, lack distinct P- and S-arrivals, and have spectra with dominant frequencies between 1 and 5 Hz (Minakami, 1974). The remaining percentage of seismic events has been identified as volcano-tectonic (VT) earthquakes, which have similar source mechanisms for earthquakes that occur in tectonic areas.

Because seismic activity at MW is monitored and recorded in continuous and event-trigger mode, we can examine three largely different datasets: 1) digitally filtered waveform data; 2) unfiltered analog seismograms of station WANC (located 3.2 kilometers west of the vent); and 3) the catalog of located earthquakes. We will refer to each of these datasets as pseudohelicorder, helicorder, and located earthquake counts, respectively. The time period covered by our different data sets is September 1, 2002 – December 31, 2002 for the pseudohelicorder and helicorder event counts and August 5, 2001 – March 18, 2004 for the catalog of located earthquakes.

5.4. Methods

We measure the seismicity rates at MW based on daily event counts out of the three datasets described and the significance of the changes is estimated

by applying the *z* (Habermann, 1987) and β (Mathews and Reasenberg, 1988) statistical tests to the data, in both ordered and randomized time series.

We define the seismicity rate changes at the volcano in terms of the rates during the periods before and after the DFE. The *z*-test is a parametric test for estimating the difference between two means, in our case the two means being compared are simply the averages of daily earthquake counts for the period preceding and following the DFE. The formula for the *z*-statistic is

$$z = \frac{(M1 - M2)}{\sqrt{\frac{(S1)^2}{N1} + \frac{(S2)^2}{N2}}} \qquad (1)$$

where:

M1, *M2*: mean rates during the two periods (before and after the DFE).
S1, *S2*: standard deviations of the rates.
N1, *N2*: numbers of days (i.e. samples) in each time period.

The *z*-statistic is interpreted in terms of significance as the number of standard deviations from the mean of a normal distribution (i.e., $z = 1.64$ represents 90% significance, $z = 1.96$ represents 95% significance, and $z = 2.57$ represents 99% significance) (Habermann, 1987). The sign of the *z*-statistic indicates the polarity of the change (i.e., $z < 0$ indicates rates increases, $z \approx 0$ indicates no change, and $z > 0$ indicates rate decreases). We also use a moving window technique to compute the *z*-values. This is done by finding all possible subdivisions of the data in two halves and computing the *z*-values for all pairs of means, allowing us to estimate the significance of a difference in mean seismicity rates at any given point (time) in the curve.

We investigated the sensitivity of the *z*-values versus time curve to the presence of abrupt changes in seismicity rates by computing the *z*-values of several synthetic data sets with varying amounts of change (decreases) in the number of earthquakes per unit time. Our synthetic datasets have the following features: (1) The seismicity rates from before to after the change are different but remain constant within each period; (2) the seismicity rate after the change is some normalized percentage of the seismicity rate before the change; (3) the value of the earthquake count at the middle point of the time series is zero, simulating an unusable record the day of the DFE. To somewhat mimic our pseudohelicorder counts data, we created synthetic time series containing one break point and two segments, simulating drops in seismicity of 100% (total drop of seismicity), 95%, 75%, 50%, 25% , and 0% (no change in seismicity). We also investigated the effect of having a seismicity rate that decreases in two steps preceding the main drop. We did this by creating a data set that has two break points and three segments with constant rate each. In this way we simulate a constant rate, and a drop of 25% that precedes a second drop of 50%, after which the seismicity stays at that level. The lengths of these synthetic data sets are 101 data points, equivalent to 101 days in our case.

To mimic our data of located LP seismic events, we created a longer synthetic data set in which there are two break points and three segments. In this case the second segment contains a drop in seismicity of 80% and the third segment represents a recovery of the seismicity rates to background values (rate equal to first segment). The length of this synthetic data set was 487 data points.

Seismicity rates changes can also be characterized using the β-statistic as described by Mathews and Reasenberg (1988):

$$\beta = \frac{n_a - E(n_a)}{\sqrt{\mathrm{var}(n_a)}} = \frac{n_a - n_b(t_a / t_b)}{\sqrt{n_b t_a / T}} \qquad (2)$$

where:

n_a=Number of earthquakes in the region of interest after the perturbing main shock.

t_a=Time period after.

$E(n_a)$=Expected number or earthquakes. $E(n_a) = rt_a$, and

$r = n_b/t_b$ is the *ambient* rate of earthquakes estimated from a background period, t_b.

t_b=Time period before (background).

n_b= Number of earthquakes during the background period.

Note that for a binomial distribution $var(n_a) = Npq$,

Where:

$p = t_a/T$, $q = 1 - p = t_b/T$,

$T = t_a + t_b$ and

$N = n_a + n_b$.

Because the observed value of n_a may be anomalous, $E(n_a)$ is used instead, and $N = n_b(1 + t_a/t_b)$.

The sign of β in this case agrees with the polarity of the change in seismicity rate (i.e., $\beta < 0$ represents a decrease in rates, $\beta \approx 0$ means no change, and $\beta > 0$ represents rates increases). Because there are various methods to compute β that differ in their underlying assumptions and the validity of those assumptions cannot readily be verified (Gomberg et al., 2003) we do not ascribe absolute significance level to the rate variations computed with β-statistic and use them only to assess spatially the nature of the seismicity rate changes at MW.

5.5. Results

5.5.1. Pseudohelicorder and Helicorder counts

The plots of cumulative daily numbers of volcanic earthquakes estimated from pseudohelicorder plots and helicorder records are shown in Figure 5.3. The absolute values in numbers of events are different because of the different criteria used to count earthquakes on each type of record and the different noise levels (usually less noise in pseudohelicorder plots) and instrumental sensitivities. The change in slope indicating the change in seismicity rate is more obvious in the pseudohelicorder counts curve. The *z*-values at the date of the DFE are $z = 6.7358$ and $z = 2.5531$ for pseudohelicorder and helicorder counts, respectively, which correspond to confidence levels for the difference in mean rates before and after de DFE above 99.99% and 99% respectively. From the cumulative number and *z*-values plot for pseudohelicorder counts, we note that the decrease in seismicity begins before the DFE, around the time of the Mw 6.7 Nenana Mountain earthquake (October 23, 2002) (NME). The helicorder count data, although somewhat noisier, also show the change in rates.

We tested the hypothesis that the data showing the suggested decrease in seismicity at Wrangell is no different from background seismicity, represented by seismicity in many random time series. To do this we randomly permute our data sets of pseudohelicorder and helicorder counts, plot the cumulative number of earthquakes versus time and compute the *z*-values for the permuted series. This is done 100 times for each data set being analyzed and we always plot the randomly permuted series along with the original data. We observe less spread in the random series for pseudohelicorder counts. Further, the data from pseudohelicorder records is equal to the random noise towards both ends of the

time series, but is different towards the middle of the series. The helicorder count data reaches the extreme value of the random noise, but does not exceed it.

5.5.2. Analysis of Synthetic Counts Data- Pseudohelicorder counts

Figure 5.4 shows several cumulative number versus time and *z*-values versus time plots for six synthetic data sets, each representing a sharp decrease in seismicity, with varying amounts of change. The results show that the spread in the randomly permuted counts increases as the amount of change in seismicity rate increases and so does the separation between real data and random permutations. This means that the stronger the rate change, the more we should be able to see it above background. Also we see that even in the case of small rate changes the *z*-values versus time curve is sharply peaked *near* the time of the change. Careful examination of the *z*-values curves reveals that the peaks occur exactly one data point before the time where the rate change starts. This is not caused by the number of data points being either even or odd, or by the presence of a zero count at the time of the change, nor by the position of the time of change in the data set. The effect is expected because the *z*-values curve is tracking the evolution of the cumulative sum in time. Let n be the total number of data points and n_i be the position of the breakpoint. The cumulative curve will be constant until exactly n_i-1, and then drops to a different rate. That is where the two segments being compared are the most different.

An additional interesting result from our testing is the observation that the steepness of the rise in *z*-values near the break point depends on the strength of the rate change. The z-values curve is sharply peaked for large changes in rate and rises more gradually for small rate changes (Figure 5.5).

The analysis of a synthetic data set with two break points (Figure 5.6) shows that when a minor decline in rate precedes a larger one, the *z*-values curve is double-peaked. Surprisingly, however, the first peak has a larger *z*-value, regardless of the length of the two segments preceding the main break point. As the length of the second segment shortens, the peaks come together into one. These curious non-intuitive results will be analyzed in the Discussion Section.

Similar effects are also present in the pseudohelicorder count data, with the two largest peaks in z-values occurring several days before the date of the DFE. The first peak in z-values occurs on October 15, 2002, and it is sensing a zero count value (unusable record) on October 16, after which the counts drop for a few days. We tested the influence of this zero value by replacing it with a value similar to its neighbors and the double peak persisted, although with slightly decreased significance. The second peak in *z*-values occurs on October 23, 2002 (the date of the NME) and it is sensing a general decrease in number of daily counts (mostly good usable days) leading to the strongest drop on November 3. We suggest that the relatively gradual increase in *z*-values leading towards the peak on October 23 reflects the magnitude of the seismicity drop following the DFE, although we cannot reject the possibility that the decrease in seismicity actually started near the NME on October 23, 2002.

5.5.3. Analysis of Synthetic Counts Data- Located Earthquake Counts

When we use a larger synthetic data set of 487 data points (equal to the number of located LP seismic events) simulating a time series with a final segment in which the rates recover to the background values, we observed that the *z*-values curve has two peaks, the first one representing the drop in

seismicity and a second one, with negative *z*-value, indicating the recovery (increase) to background rates (Figure 5.7).

5.5.4. Located Volcanic Earthquakes

We examined the catalog of located earthquakes at MW from August 2001 through March 2004. In Figure 5.8 we show a time-depth plot of earthquakes at MW. Notable changes in seismicity rate include the apparent increase associated with the introduction of the EARTHWORM acquisition system (Johnson et al., 1995; Dixon et al., 2003); the decrease following the DFE, and two other subsequent decreases (July – September 2003 and December 2003) associated with temporary telemetry problems and data disruptions.

We used the computer program ZMAP (Wiemer, 2001) which is suited for analysis of located earthquakes and includes routines to estimate changes in seismicity rates. The catalog includes 508 events with magnitude from -0.2 to 2.7. A standard estimate of the magnitude of completeness indicates the catalog to be complete for magnitudes $\geq$ 0.9, in agreement with the value reported by Dixon et al. (2003b). To avoid artifacts introduced by artificial rate changes, we select a subset of earthquakes between early March 2002 and late June 2003 (dotted box in Figure 5.8). Also, to ensure the completeness of the samples used, we select only earthquakes with magnitudes $\geq$ 0.9 for subsequent analysis.

The other decreases in seismicity rates observed in the catalog appear to be unrelated to large earthquakes along the Denali fault because the only other event of note was the Mw 5.7 earthquake on 22 October, 1996 (Ratchkovski et al., 2003). We infer that these decreases are caused by other factors such as temporary low signal-to-noise ratio or station outages. We note that the

decrease in seismicity at MW following the DFE was unrelated to "artificial" causes because the same analyst located all the volcanic earthquakes, all the stations were operational during the time of the decrease, and there were no changes to software or recording systems.

The catalog of located earthquakes at MW from August 5, 2001 to March 18, 2004, includes at least three decreases of noticeable duration. The only decrease in seismicity at MW following a large earthquake along the Denali fault is the one that followed the DFE. The other two decreases are artificial (temporary telemetry problems) and are not preceded by large earthquakes in the area or by moderate-sized (with magnitude 5.0 or larger) aftershocks of the DFE (AEIC, 2003). Thus although the seismicity rates at MW fluctuate, the coincidence of the rate decrease onset time with the DFE sequence suggests a causative relation and is not the result of chance.

To test the hypothesis that the decrease following the DFE, as estimated from located earthquakes, may not be different from random noise, we follow our previous procedure of randomly permuting our data sets of located earthquake counts (100 times), plot the cumulative number of earthquakes versus time, and compute the *z*-values for the permuted series. We show the results along with the original data in Figure 5.9. We do the analysis for LP and VT earthquakes separately. For LP events the cumulative number versus time plots shows several changes in slope that represent decreases in seismicity. The decrease associated with the DFE sequence, however, represents the breakpoint with the most significance, because the peak in *z*-value happens near the time of the DFE and nowhere else. We found that for LP events the cumulative number and *z*-values curves are different from their respective permuted series. Further, we note that data of located LP seismic events does not show a negative peak in the *z*-values curve that we observed by creating a

synthetic data set in which there was a recovery towards background rates. In other words, there is no apparent recovery.

For VT earthquakes the ordered data is no different from the randomly permuted series. The catalogs of located LP and VT earthquakes (Figures 5.8, 5.9) show that the decrease in seismicity occurred in a gradual manner after the DFE. This is because few earthquakes could be located during the immediate few days following the DFE. The total number of VT earthquakes is too small to draw reliable conclusions.

5.5.5. Spatial Mapping of the Amount of Decrease Using β-statistic

To examine spatially the decrease in seismicity at MW we divide the area of interest into a grid with nodes separated by 3 km (average of horizontal location errors) and compute the β-statistic using equation (2) for the 30 nearest earthquakes to each node. The two periods being compared to compute the β-statistic are: March 1, 2002 – November 3, 2002 and November 3, 2002 – June 30, 2003. The two time periods are of roughly equal duration (eight months each). The map of the β-statistic for MW is shown in Figure 5.10 and it shows a general decrease in the seismicity rates everywhere on the volcano. A small area located southwest of the vent experienced relatively little to no change, but this is a region with sparse seismicity. The catalog used is rather small, but the seismicity is distributed so that the radius of circles used to enclose the 30 nearest earthquakes to each node varied between < 2 km for areas around and west of the vent to 10 km around the edges of the region mapped.

5.6. Discussion

We examined the rate of occurrence of volcanic earthquakes at MW from before to after the DFE, at different time scales and using different data sources, to find the amount and significance of an observed decrease in volcanic seismicity. We think we can reliably measure this decrease because MW is an area with a high rate of background seismicity, and such places are optimal for observation of seismicity declines (Toda and Stein, 2002). The decrease that we see in the seismicity at MW following the DFE is not the decay from an aftershock sequence of a large earthquake rupturing along the Denali fault. The seismicity along the Denali fault is not collocated with the seismicity at Mt. Wrangell (Figure 5.2) and because we carefully checked all seismograms at station WANC on MW, we could easily identify non-local earthquakes and discard them from our counts (see, for example, Figure 3 of Sánchez and McNutt, 2005).

We used rigorous statistical testing of the earthquake data and found the rates of local volcanic earthquakes (LP and VT together) to have decreased by 40% when the pseudohelicorder record data is used in the time scale of two months before to two months after the DFE (Figure 5.3). In some areas around the volcano the seismicity may have decreased by as much as 80% when the located earthquake data from eight months before to eight months after the DFE are used (Figure 5.9). Although visual inspection of the data suggests that the rates of both LP and VT earthquakes decreased (Figures 5.8 and 5.9), it is statistically difficult to prove for VT earthquakes because of their low rate of occurrence. From the depth-time plot and the analysis of cumulative number of located earthquakes we found that the decrease lasted for five months after which the seismicity appears to recover to pre-DFE levels.

We investigated the question of why the *z*-values curve does not seem to reach its peak exactly on November 3, 2002 (the time of the DFE), but in most cases, before that time. By computing the *z*-values on six synthetic data sets with varying amounts of rate decrease (Figures 5.4 and 5.5), we found that the *z*-values curves reach their peak exactly one data point before the drop in seismicity begins, which is expected because the rate before the change is constant exactly until that data point. An obvious conclusion of this test is that if the rates of seismicity are not perfectly constant within each period, we should expect to find variations in the behavior of the *z*-values curve and the presence of multiple peaks of varying significance, which is what we see in our data (Figure 5.3). We also found that the *z*-values curve is highly sensitive to sharp rate changes, regardless of the amount of change.

We also tested the effect, in the *z*-values curve, of having a decrease in seismicity in two steps before the main perturbation and the effect of a seismicity rate that fully recovers sometime after the perturbation. The motivation for these two tests is the fact that our pseudohelicorder count data shows an apparent decrease in rates beginning sometime before the DFE (Figure 5.3) and because in the catalog of located earthquakes it *appears* as if the seismicity recovers to pre-DFE levels (Figures 5.8 and 5.9).

By simulating a two-step decrease in seismicity preceding the main rate change we observed that the *z* values curve is double-peaked and that the first peak indicates a more significant change (Figure 5.6). This puzzling result comes about because the *z*-values are a combination of the differences in means, the standard deviations of the two samples, and the number of data points in each sample (Equation. 1). Examination of Figure 5.6 indicates that at the position of the first peak: $M1-M2$= 0.4221, $S1$ =0, $S2$=0.1361, $N1$=24, and $N2$=77; whereas at the second peak $M1-M2$=0.3798, $S1$=0.1262, $S2$=0.07,

N1=50, and *N2*=51. Thus it is apparent that the relative values of the peaks depend mostly on the difference in means and the number of data points on each segment. In the *z*-values curve for our pseudohelicorder (filtered data) counts data we see some of the features identified in the curves for synthetic data. The pseudohelicorder counts data shows a *z*-values curve with a "regional" maxima that happens before the DFE but we also observe that this maxima is double-peaked, indicating that there were some step-wise changes in earthquake rates at the volcano.

From the analysis of the located events at MW, on the other hand, we learned that the seismicity may have dropped after a few days following the DFE. We see this in Figures 5.8 and 5.9. By separating LP events from VT events we infer that both types of events may have decreased in rates, but because the low number of VT events available it makes it statistically difficult to prove.

The results of tests with synthetic data suggest that unless the rates of seismicity are fairly uniform before and after the perturbation, it is difficult to use the *z*-values to pinpoint exactly the *time* of change. This does not mean the plot is not useful, because the *z*-values curve does indicate the presence of one or several important changes in rates within the data set under scrutiny.

We also simulated a time series in which an 80% drop in rate is followed by a recovery to the original rates (Figure 5.7). In this case we observed that the *z*-values curve has two peaks, one positive and one negative. We designed this synthetic data set based on some features of our located earthquakes counts data in which a drop of about 80% in seismicity is followed by an apparent recovery after five months of lower-than-normal rates (Figure 5.8 and 5.9). Because we do not see the negative peak in the *z*-values curve of our real data,

we infer that the seismicity at MW did not recover fully to pre-DFE rates, at least until the end of the time period analyzed (June 30, 2003).

Although seismicity rates at volcanoes vary in the absence of evident external factors, the coincidence of the decrease with the time of the DFE suggests that the drop in seismicity at MW was not the result of chance. The total duration of the catalog of located earthquakes, including those with M < 0.9, is 957 days, or roughly 32 months; we see in this time period (Figure 5.8) three noticeable drops in reported seismicity (one of them following the DFE, the other two are artificial) and the average duration of these three periods of low seismicity is ~ 3 months. Thus there are about 11 3-month-long periods during which we may or may not find a decrease. In the context of a binomial distribution, we have n=32/3= 11 trials and three successes (decreases). The probability p of success in a given binomial trial is p=3/11=0.27. This means that the probability of not finding an anomalously low-seismicity period is q = 1- p = 0.73, thus about 73% of the time we find that the seismicity is at background rates.

If we consider a more homogeneous catalog, with magnitudes $\geq$ 0.9, and only during March 1, 2002-March 18, 2004 (after data acquisition with Earthworm began) the number of available months and 3-month trials gets reduced to 25 and 8, respectively, and the probability of finding a decrease rises to p=0.38, making it a more common fact. But this may be a biased test, because we know that the two latest decreases are man-made. In our view, a more balanced test would only include the period March 1, 2002 – June 30, 2003 (dotted box in Figure 5.8). In this case there are 487 days or roughly 16 months, which means we have only n=16/5≈3 trials. The probability p of finding a decrease is p=1/3=0.33, thus q=0.67. This means that about 70% of the time we would find the seismicity to be at background rates.

Because the only large earthquakes along the Denali fault during the time period March 1, 2002 – June 30, 2003, were associated with the DFE sequence and because the decrease in seismicity began rather close in time to the DFE, we infer that it was not a chance occurrence but that the cause was a perturbation of the volcanic plumbing system caused by either the dynamic shaking or the sudden drop in pressure around the volcano (Sánchez and McNutt, 2005). A spatial mapping of the β-statistic (Figure 5.10) shows a general decrease in seismicity around MW with some patches of larger change located south, north and west of the vent and an area of little to no change southwest of the vent. The mapping should be interpreted with caution because the locations of earthquakes at MW are preliminary.

5.7. Conclusions

A decrease in volcanic seismicity occurred at MW following the Denali fault earthquake sequence that began with the Mw 6.7 Nenana Mt. Earthquake and culminated with the nucleation of the Mw 7.9 Denali earthquake on November 3, 2002. Our data indicate that the volcanic seismicity dropped by as much as 80% during the five months that followed the DFE sequence. Our tests with synthetic data showed that unless the seismicity rates are fairly constant during the pre and post-perturbation periods, we cannot use the z-values curve to pinpoint exactly the time of change. The presence of a broad peak, however, indicates a significant change in the rates and that is what we see in the data. Because of the time coincidence of the decrease in the seismicity rate with the time of the DFE sequence we think this is not a chance occurrence, but an effect attributable to the DFE sequence. A comparison of our data of located earthquakes at MW with a synthetic data set reveals that the seismicity at Wrangell during the period November 4, 2002 – June 30, 2003 did not recover

to the pre-DFE levels. The mapping of the β-statistic indicates that the decrease in seismicity occurred around the general MW area, with some patches showing a stronger change than others.

5.8. Acknowledgements

The authors wish to thank J. Grasso, E. Brodsky, K. Felzer and C. Benson for useful comments and discussion. Many thanks to S. Stihler and J. Dixon for their hard work in the location of earthquakes at Alaskan Volcanoes. This work was supported by the Alaska Volcano Observatory and the U.S. Geological Survey (USGS), as part of their Volcano Hazards Program, and by additional funds by the State of Alaska.

5.9. Figures

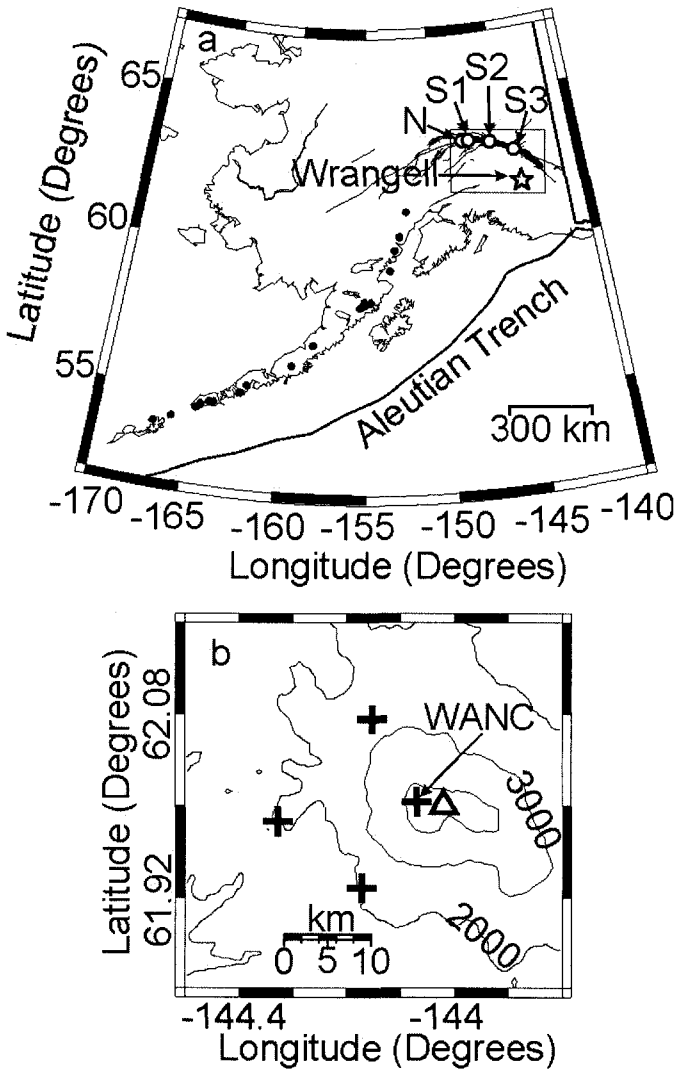

Figure 5.1. Location maps for MW. (a) Map of Alaska showing the surface rupture from the DFE (thick solid line) and the epicenters of the October 23, 2002 Nenana Mountain earthquake (N) and the three main sub-events of the November 3, 2002 Denali fault earthquake (S1, S2, S3) (Surface rupture from Eberhart-Phillips et. al., 2003, epicenters of N and S1-S3 are from AEIC, 2003); Mt. Wrangell volcano(star); other volcanoes seismically monitored by AVO (dots); and main faults and tectonic structures (thin black lines). The rectangle encloses the area of Figure 5.2. (b) Map of MW with topographic contours every 1000m. Crosses mark the seismograph stations. The triangle marks the vent.

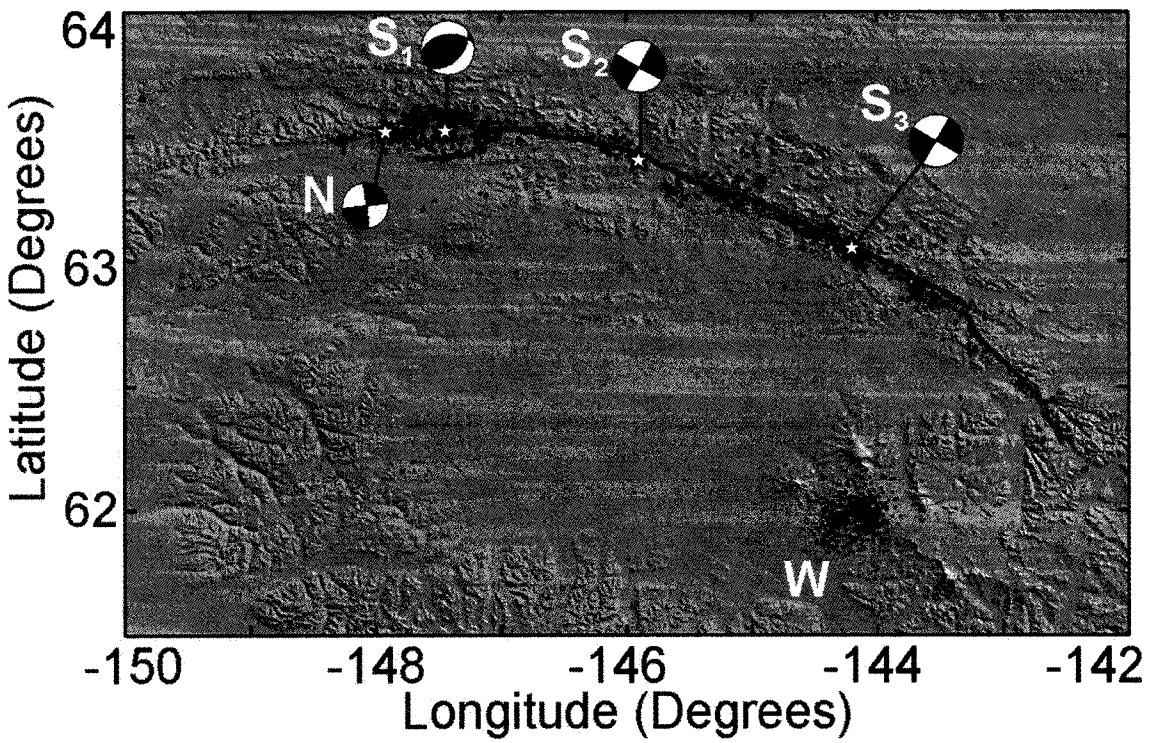

Figure 5.2. Tectonic and volcanic seismicity. Detail of rectangular area shown in Figure 5.1. Red thick line: surface rupture from the DFE; fault-plane solutions shown for the DFE sequence earthquakes in lower hemisphere projections with compressional areas in black and dilatational areas in white; green dots: Some of the earthquakes located by AEIC between October 23, 2002 and October 23, 2003, with depths above 30 km and Magnitude 3 and above. (895 epicenters are shown); magenta dots: volcanic earthquakes (LP and VT) at Mt. Wrangell located by AVO between August 5, 2001 and March 18, 2004. Other conventions as in Figure 5.1. Topography: SRTM data courtesy of NASA/JPL.

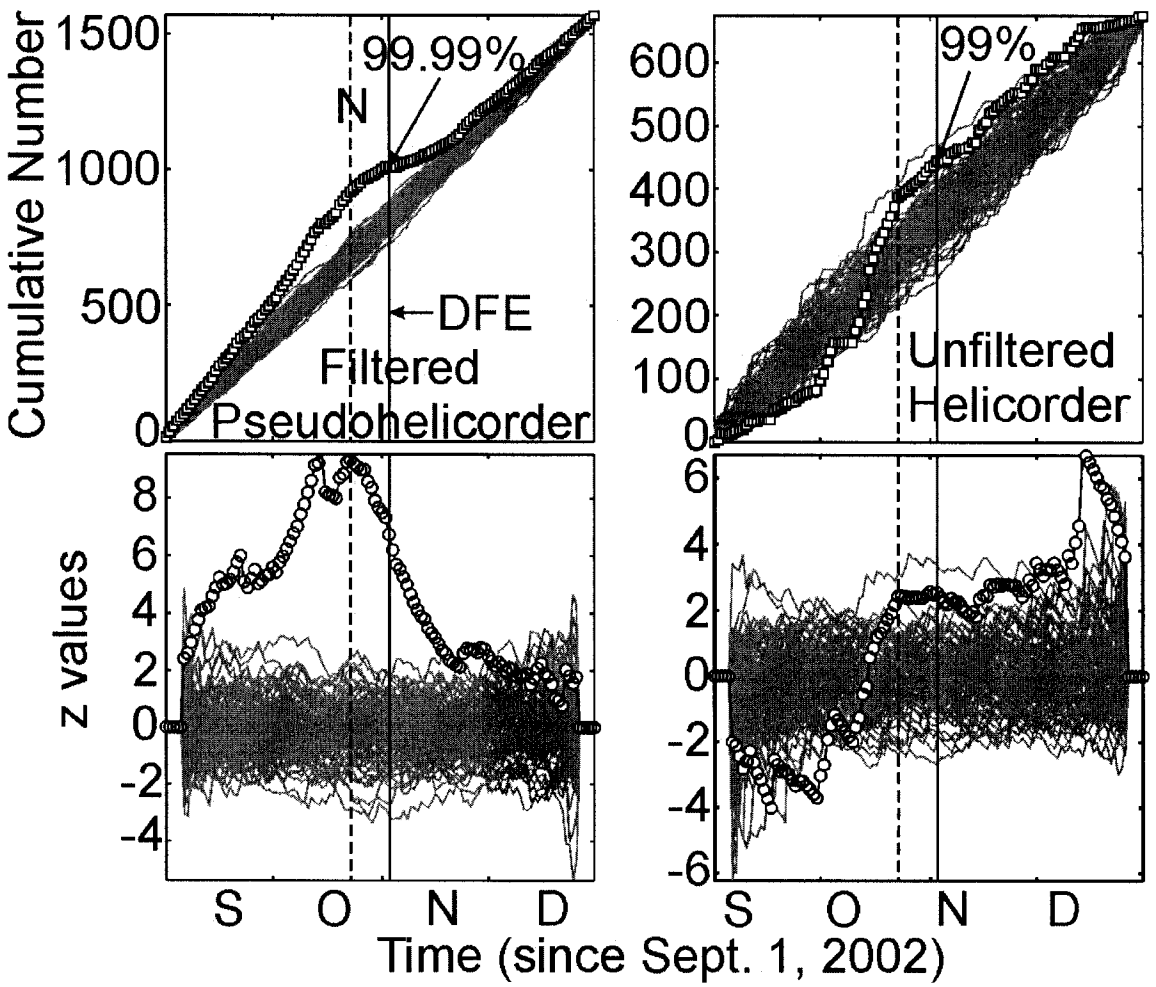

Figure 5.3. Pseudohelicorder counts and *z*-values at MW. Seismicity rates and *z*-values estimated from earthquake counts on Pseudohelicorder and helicorder records from station WANC on MW, between September 1, 2002 and December 31, 2002. Top: Cumulative number of volcanic earthquakes versus time; bottom: plot of *z*-values versus time. Squares and circles represent the cumulative sum and *z*-values curves, respectively, for actual data; gray lines represent the result of 100 random permutations of the data in each plot. Vertical dashed and solid lines mark the dates of the Nenana Mountain earthquake (10/23/2002) and the DFE (11/3/2002), respectively. Percentages indicate the confidence levels at which the two means, before and after the DFE, are different as evaluated by the *z*-test.

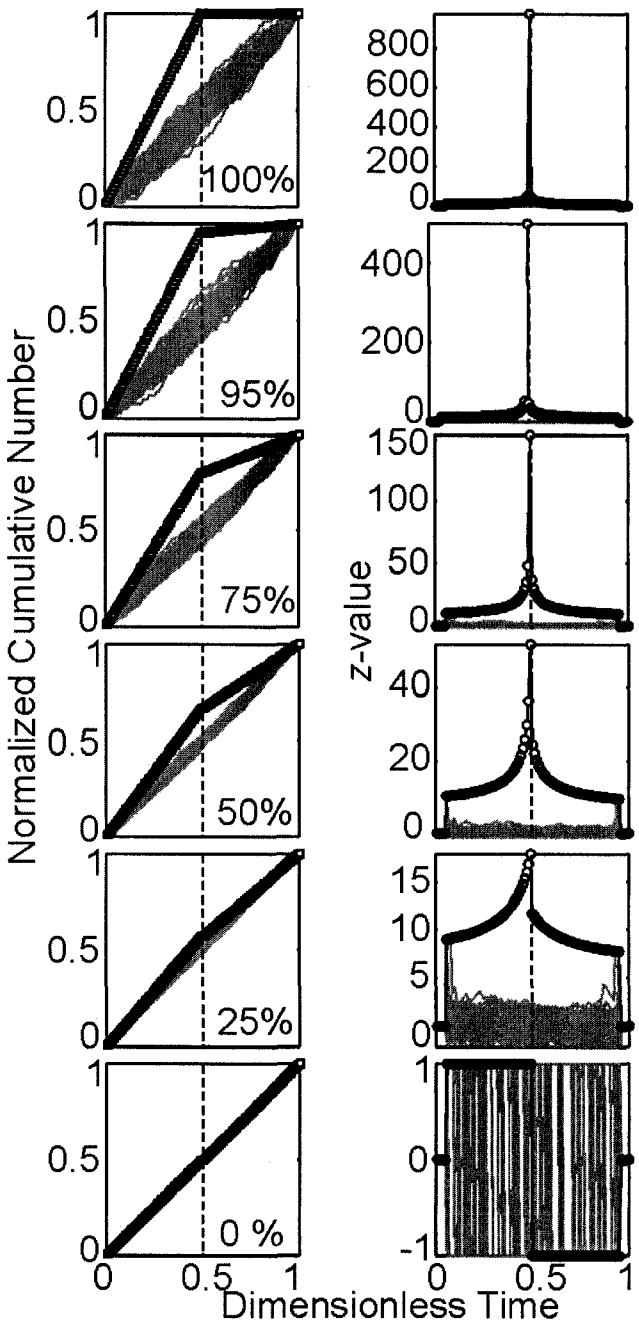

Figure 5.4. Simulation of variable rates decreases. Cumulative sum (left panels) and *z*-values (right panels) plots for six synthetic data sets with one break point in the middle and varying amounts of rate decrease. A vertical dashed line marks the time of the change, in which a value of zero in the counts has been assigned, simulating an unusable record. The top plot of *z*-values, for a drop in seismicity of 100%, has been cut off at z≈1000 because the peak value is at infinity. Other conventions as in Figure 5.3.

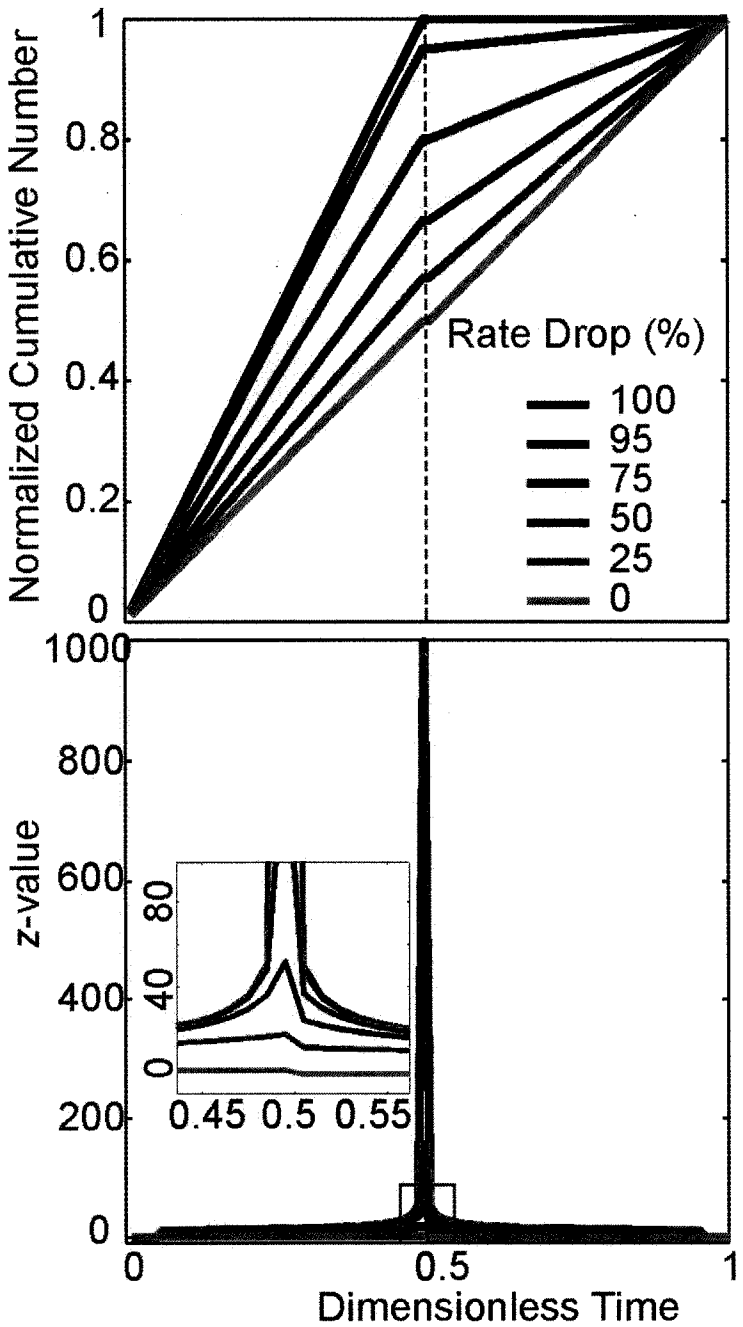

Figure 5.5. Comparison of synthetic data sets. The data sets used in Figure 5.4, plotted at the same scale to allow comparison of the *z*-values curves. The inset is an enhanced view of the rectangle at the base of the *z*-values plot. Other conventions as in Figure 5.4.

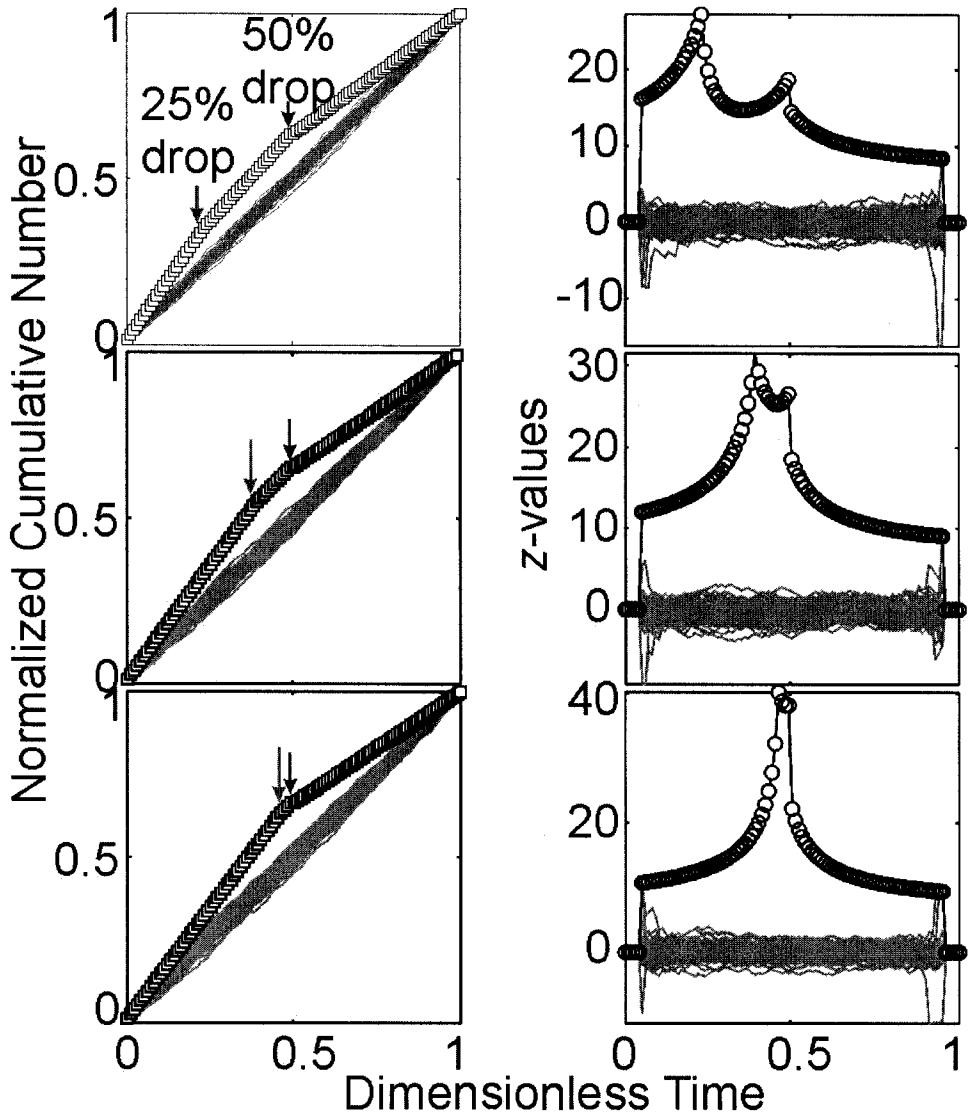

Figure 5.6. Simulation of a two-step decrease in rate. Cumulative number and *z*-values plots for synthetic data with two break points representing an initial drop in rate by 25% followed after some time by a larger drop of 50%. Vertical arrows mark the time of the drops. The start time of the first (and smaller) drop varies, while the start time of the larger drop is constant. Other conventions as in Figure 5.3.

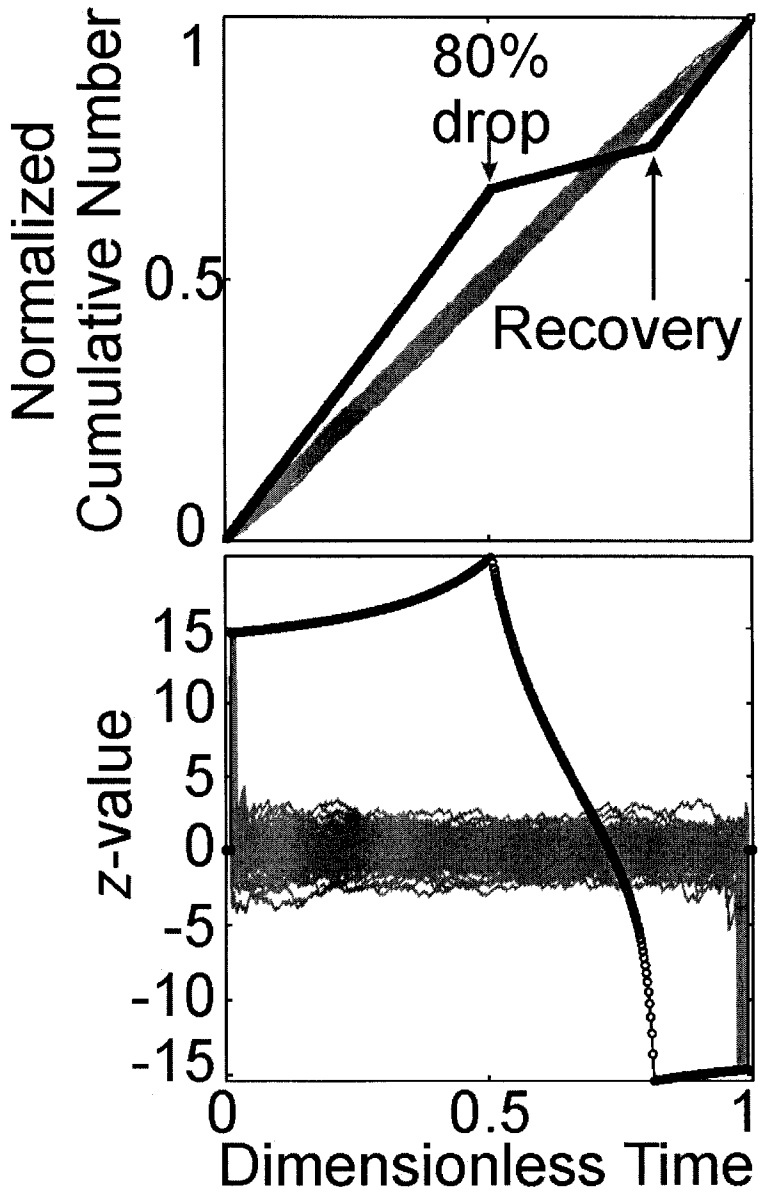

Figure 5.7. Simulation of a drop-recovery sequence. Cumulative sum and *z*-values versus time for synthetic data that simulates a recovery to pre-perturbation rates following a drop in seismicity by 80%. Vertical gray and black arrows mark the start times of the drop in rate and recovery, respectively. Other conventions as in Figure 5.3.

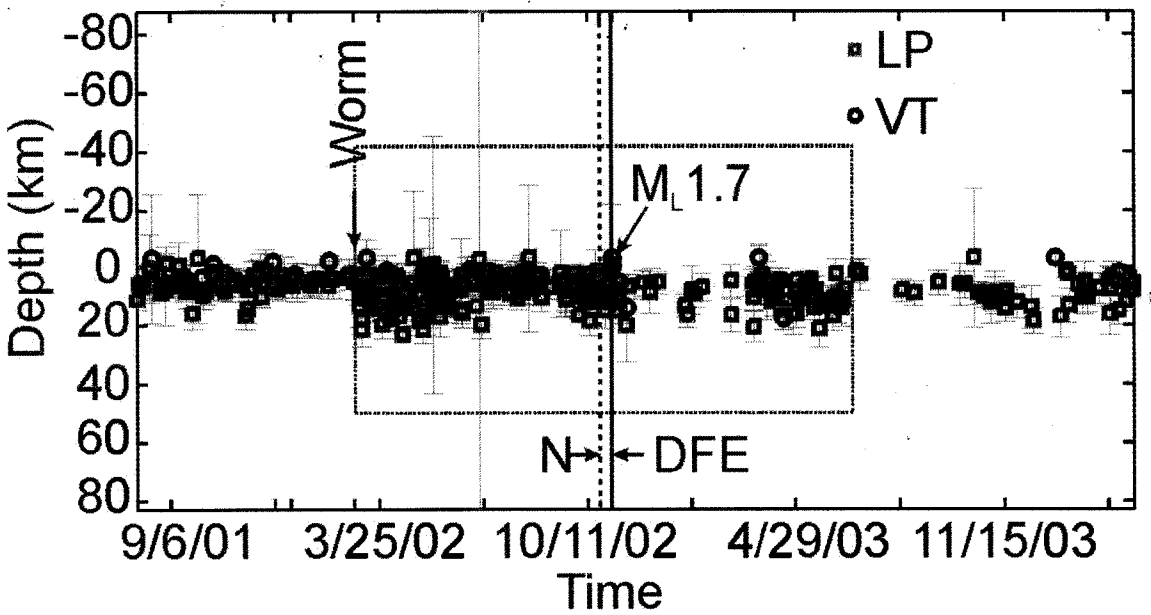

Figure 5.8. Seismicity versus time at MW. Depth-time plot for located earthquakes at MW between August 5, 2001 and March 18, 2004. Red squares and blue circles with gray error bars mark LP and VT earthquakes, respectively. Only earthquakes with magnitude $\geq$ 0.9 are shown. The time of change from IASPEI to EARTHWORM acquisition system is labeled as "Worm". A dotted rectangle encloses the most homogeneous part of the catalog, between March 1, 2002 and June 30, 2003 that is used for all analysis of located earthquakes. Other conventions as in Figure 5.3.

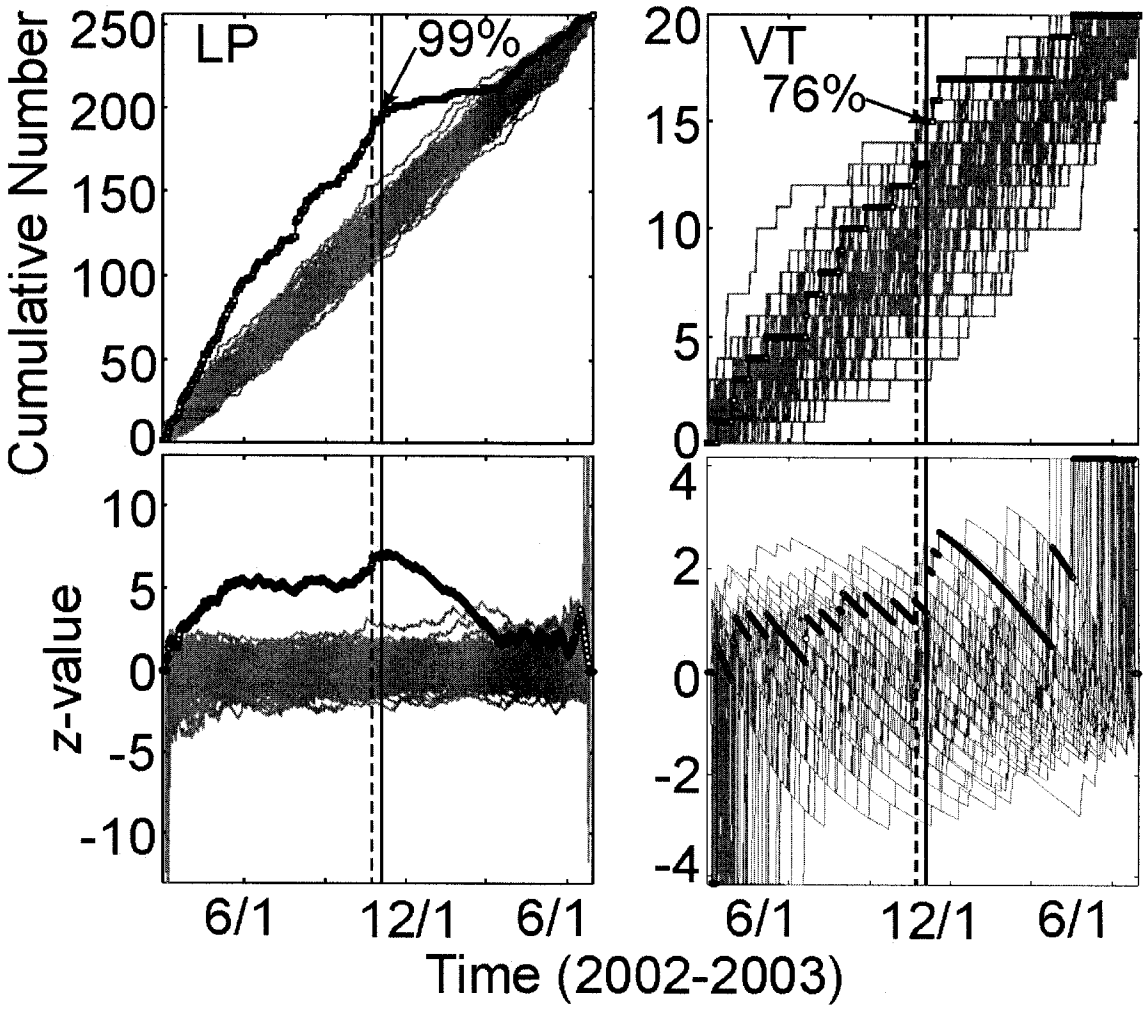

Figure 5.9. Located LP and VT earthquakes at MW. Cumulative sum and *z*-values versus time plots for earthquake counts based on located events between March 1, 2002 and June 30, 2003 (dotted rectangle in Figure 5.8). Left: plots for LP seismic events. Right: Plots for VT earthquakes. Conventions as in Figure 5.3.

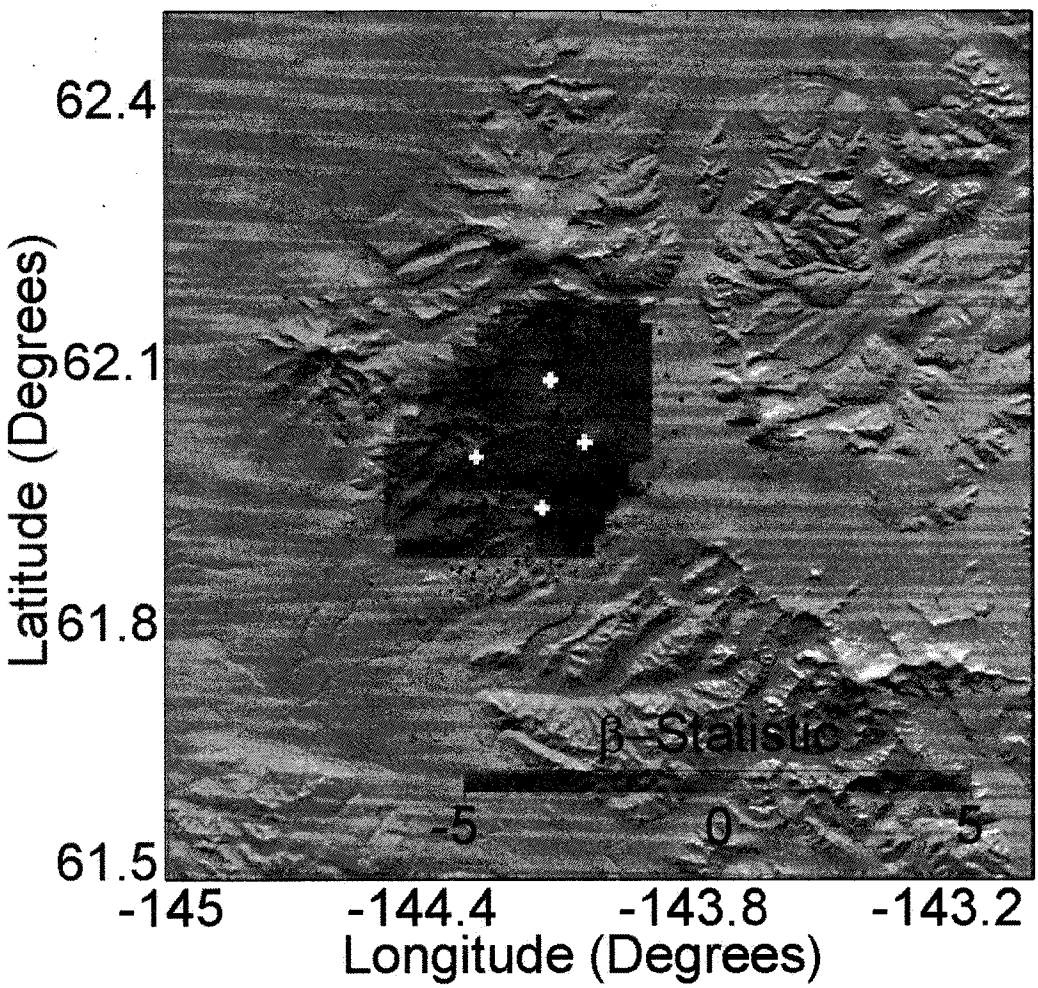

Figure 5.10. Map of β-statistic. Map of MW showing the seismicity rate changes, as evaluated by the β-statistic. The two time periods being compared are: Pre-DFE: March 1, 2002 to November 3, 2002; post-DFE: November 3, 2002 to June 30, 2003. The node spacing used for mapping was 3 km. Blue colors indicate rate decreases. Crosses: Seismograph stations (WANC is the station close to the center of the map). Green and magenta dots mark the epicentral locations during the pre-DFE and post-DFE periods, respectively. Topography: SRTM data courtesy of NASA/JPL.

5.10. References

AEIC-Alaska Earthquake Information Center (2003): "Earthquakes in Alaska, periodic publications, 12 issues/year", 1991-2003.

Alvarado, G. E., M. Fernandez, R. Barquero, H. Flores and G. J. Soto (1992): "Aborted eruptions triggered by earthquakes?". *EOS*, **73**, 194.

Dixon, J. P., S. D. Stihler, J. A. Power, G. Tytgat, S. C. Moran, J. Sánchez, S. Estes, S. R. McNutt and J. Paskievitch (2003a). Catalog of earthquake hypocenters at Alaskan volcanoes: January 1 through December 31, 2002, U. S. Geol. Sur. Open-File Rept. 03-267, 58 pp.

Dixon, J. P., J. A. Power and S. D. Stihler (2003b): "Seismic monitoring of Alaska's volcanoes: A comparison of event detection with IASPEI and Earthworm acquisition systems". *EOS* **84**-46.

Dixon, J. P., S. D. Stihler, J. A. Power, G. Tytgat, S. C. Moran, J. Sánchez, S. R. McNutt, S. Estes, and J. Paskievitch (2004). Catalog of earthquake hypocenters at Alaskan volcanoes: January 1 through December 31, 2003, U. S. Geol. Sur. Open-File Rept. 2004-1234, 69 pp.

Eberhart-Phillips, D., P. Haeussler, J. T. Freymueller, A. D. Frankel, C. M. Rubin, P. Craw, N. A. Ratchkovski, G. Anderson, G. A. Carver, A. J. Crone, T. E. Dawson, H. Fletcher, R. Hansen, E. L. Harp, R. A. Harris, D. P. Hill, S. Hreinsdóttir, R. W. Jibson, L. M. Jones, R. Kayen, D. K. Keefer, C. F. Larsen, S. C. Moran, S. F. Personius, G. Plafker, B. Sherrod, K. Sieh, N. Sitar, W. K. Wallace (2003): "The 2002 Denali fault earthquake, Alaska: a large magnitude, slip-partitioned event". *Science* **300**, 5622, 1113-1118.

Gerlach, D. C., F. A. Frey., H. Moreno and L. López-Escobar (1988): "Recent volcanism in the Puyehue-Cordon Caulle region, southern Andes, Chile (40.5°S): Petrogenesis of evolved lavas". Journal of Petrology, **29**, 2, 333-382.

Gomberg, J., P. Bodin and P. A. Reasenberg (2003): "Observing earthquakes triggered in the near field by dynamic deformations". *Bulletin of the Seismological Society of America*, **93**, 1, 118-138.

Habermann, R. E. (1987): "Man-made changes of seismicity rates". *Bulletin of the Seismological. Society of America,* **77,** 141-159.

Hill, D., F. Pollitz and C. Newhall (2002): "Earthquake-volcano interactions". *Physics Today*, **55**, 11, 41-47.

Johnson, C. E., A. Bittenbinder, B. Bogaert, L. Dietz and W. Kohler (1995): "EARTHWORM: A flexible approach to seismic network processing, *Incorporated Research Institutions for Seismology Newsletter*". **4**, 2, 1-4.

McNutt, S. R., and J. J. Sánchez (2002): "Intermediate-term declines in seismicity at two volcanoes in Alaska following the Mw 7.9 Denali fault earthquake". *EOS* **83**, 47.

Matthews, M. and P. Reasenberg (1988): "Statistical methods for investigating quiescence and other temporal seismicity patterns". *PAGEOPH*, **126**, 2-4, 357-372.

Minakami, T. (1974): "Seismology of volcanoes in Japan". In: Civetta, L., P. Gasparini, G. Luongo and A. Rapolla (Editors), *Physical Volcanology*, Elsevier, Amsterdam-New York, pp. 1-27.

Ratchkovski, N. A., R. A. Hansen, J. C. Stachnik, T. Cox, O. Fox, L. Rao, E. Clark, M. Lafevers, S. Estes, J. B. MacCormack, and T. Williams (2003): "Aftershock sequence of the Mw 7.9 Denali fault, Alaska, earthquake of 3 November 2002 from regional seismic network data. *Seismological Research Letters*. **74**,6, 743-752.

Sánchez, J. J. and S. R. McNutt (2005): "Intermediate-term declines in seismicity at Mt. Wrangell and Mt. Veniaminof volcanoes, Alaska, following the November 3, 2002, Mw 7.9 Denali Fault Earthquake", *Bulletin of the Seismological Society of America*, Vol 94, No 6B, pp S1-S14.

Tilling R. I., R. Y. Koyanagi, P. W. Lipman, J.P. Lockwood, J.G. Moore and D. A. Swanson (1976): "Earthquake and related catastrophic events, island of Hawaii, November 29, 1975: A preliminary report". U.S. Geol. Surv. Circular **740**: 33 pp.

Toda, S. and R. Stein (2002): "Response of the San Andreas fault to the 1983 Coalinga-Nuñez earthquakes: An application of interaction-based probabilities for Parkfield". *Journal of Geophysical Research*, **107**, B6, doi:10.1029/2001JB000172.

Wiemer, S. (2001): "A software package to analyze seismicity: ZMAP". *Seismological Research Letters*. **72**,2, 374-383.

Chapter 6. A Velocity Model for Mt. Veniaminof, Alaska: Volcano-Tectonic Seismicity and Implications for an Active Magmatic System[1]

6.1. Abstract

A minimum one-dimensional velocity model with station corrections for Mt. Veniaminof, Alaska, was derived based on 93 volcano-tectonic earthquakes with magnitudes between 0.3 and 3.0 and occupying a volume of 140 km x 70 km x 40 km. The model consists of 8 layers over a half space with P velocities that range from 4.82 ± 0.13 km/s in the upper layer to 8.30 ± 0.37 km/s in the half space, and a V_p/V_s ratio ranging from 1.61 ± 0.07 at the surface to 1.83 ± 0.13 at depth. Lateral variations in V_p/V_s are also apparent. Relocation of seismicity suggests that epicenters are stable and locate preferentially outside the caldera. Hypocenters could be constrained to within a few km and, in the upper 20 km, they cluster into two regions diverging from the vent and surrounding a mostly aseismic volume.

Fault-plane solutions for a subset of relocated earthquakes are mostly consistent with oblique thrust and normal faulting. We tested the hypothesis that the fault-plane solutions could be explained by regional tectonics, and found significant spatial variations in stress around and beneath Mt. Veniaminof. Temporal variations in stress may have occurred, but cannot be well resolved with the available data. Modeling of Coulomb stresses due to expansion of dikes in an elastic half space indicates that strike-slip and thrust faults are favored. We suggest that the active magma system beneath the volcano

[1] Sánchez, J.J. A Velocity Model for Mt. Veniaminof, Alaska: Volcano-Tectonic Seismicity and Implications for an Active Magmatic System. Manuscript submitted to *Journal of Volcanology and Geothermal Research.*

consists of a dike or system of radial dikes whose pressure variations change stresses in the crust and cause movement along pre-existing faults.

6.2. Introduction

Mt. Veniaminof (MV) volcano is a large stratovolcano on the Alaska Peninsula (56.2°N, 159.4° W, elevation: 2507 m; Figure 6.1a), 35 km wide at the base and truncated by a summit caldera 8x11 km in diameter, with an intracaldera cone with a summit height of 2156 m (Miller et al., 1998). Historical eruptions probably all originated from the intracaldera cone and date back to 1830 (Simkin and Siebert, 1994). Quaternary cones in the MV area (Detterman et al., 1981a, b) are roughly aligned in a SE-NW-trending direction with an average strike of 145° from north (Nakamura et al., 1977) (Figure 6.1b).

In the summer of 2001 the Alaska Volcano Observatory (AVO) deployed a seismograph network on MV. The network is composed of 8 stations equipped with Mark Products L4-C vertical component seismometers with a natural period of 1 sec. (Figure 6.1b.) Archiving and processing of data from these stations began in February 2002 and since then, a variety of local and non-local signals have been recorded. Among the detected local signals are volcano-tectonic (VT) and long-period (LP) events. VT events are no different from the earthquakes that occur along faults such as the Denali fault in Alaska. Some of these VT earthquakes seem to locate close to the volcano, within the perimeter of the volcanic pile, whereas some others locate in the surrounding area (Figure 6.1b). For sources below a few kilometers depth, VT earthquakes have sharp, high-frequency P and S arrivals with peak frequencies above 5 Hz and very short codas (Lahr et al., 1994). VT earthquakes are assumed to be caused by brittle failure in response to stress changes associated with magmatic activity.

The background seismic activity of MV is characterized by low rates of VT earthquakes, and periods of enhanced seismicity and mild eruptions from late September 2002 to March 2003 and February 2004 to present have been characterized by the occurrence of many LP events and episodes of tremor. These seismic signals will be described in a separate chapter (chapter 7).

The routine location procedure for earthquakes at MV is based on the computer program HYPOELLIPSE (Lahr, 1999) assuming a regional velocity model consisting of 8 layers over a half space, with velocities increasing with depth and using a constant Vp/Vs ratio of 1.78 for all layers (Fogleman et al., 1993; Dixon et al., 2003). This generalized model is used at volcanoes for which specific models have not yet been devised (Table 6.1). Because the location of earthquakes is known to be highly dependent on the velocity model, we wish to develop a one-dimensional velocity model that minimizes the location errors of a set of VT earthquakes recorded by the seismograph network, thus allowing us to study the volcano in greater detail. Because we constrain the locations and velocity model, we can compute Fault-Plane Solutions (FPS) for selected earthquakes and study the stress regime around and beneath MV.

6.3. Data

We selected a total of 93 locatable VT earthquakes recorded between late August 2002 and mid September 2004 (Figure 6.1b). We first examined all their waveforms and re-picked phase arrivals and whenever possible, reliable first-motion polarities. We used only arrivals at the MV seismograph network because we wanted to construct a velocity model based on earthquakes whose ray paths sampled mostly the volcano.

As error estimates, the program HYPOELLIPSE computes for each earthquake the orientation and dimensions for the semi-major principal axis of the 68% confidence ellipsoid. The vertical semi-axis of the confidence ellipsoid is termed SEZ. The surface projection of the hypocentral confidence *ellipsoid* is called the epicentral *ellipse*, and the larger of its two semi-axes is termed SEH (Lahr, 1999). For our data set of preliminary locations the length of SEH varied between 0.3 and 4 km, with an average of 1.1 km; SEZ varied between 0.4 and 16 km, with an average of 8.5 km. The root mean square of travel time residuals (RMS) for the 93 earthquakes ranged from 0.02 to 0.99 s, with an average of 0.31 s. The earthquakes in this initial data set had magnitudes in the range 0 – 3.0, and depths ranging between -3.0 and 30.0 km (depths referred to sea level, with negative depths corresponding to locations above sea level).

6.4. Methods

6.4.1. Search for a Minimum Velocity Model

Generally speaking, neither the spatial locations of the earthquakes nor the velocity distribution in the study area are known. The only information we have available are the arrival times of earthquakes to a set of seismograph stations, thus we need to make an initial guess about the unknown parameters (origin time, coordinates of hypocenter, and velocity model). If we use an initial velocity model, it is possible to trace the ray paths from the initial suggested locations to the seismometers and calculate a theoretical arrival time. Obviously there will be a difference between our observed arrival times and the theoretical ones. This difference is termed the travel time residual and it is a function of the differences between the estimated and true hypocentral locations and velocity parameters. Some adjustments to our initial guess for locations and velocity distribution are needed to make the residuals as small as possible. The

dependence of both the hypocentral and the velocity model parameters on the observed travel times is non-linear, but a linear approximation can be expressed in terms of adjustments and the partial derivatives of travel times with respect to all these parameters. The calculation of travel times and the partial derivatives is called the forward problem and the calculation of the adjustments needed is called the inverse problem. Also because neither the hypocentral parameters for the group of earthquakes nor the velocity parameters are known, the problem of estimating them based on a set of arrival times is called the coupled hypocenter-velocity-parameter problem (Kissling, 1988).

We used the computer program VELEST (Ellsworth, 1977; Roecker, 1981; Kradolfer, 1989) which uses a set of preliminary earthquake locations, station locations, and a starting velocity model to solve the coupled problem through an iterative process. VELEST also finds the station corrections that minimize the RMS of travel times for the entire set of earthquakes. To develop a one-dimensional velocity model for MV we use a suite of initial velocity models with varying configurations in velocity distribution and geometry, and follow a trial-and-error approach in which each initial model is used to find a final model that minimizes the average RMS, and an optimal model is chosen from the set of final models.

With our preliminary locations of 93 shocks and a set of 39 different starting velocity models (Figure 6.2) we performed repetitive VELEST runs. All of our starting models represent several layers over a half space, with velocity increasing with depth. The top of all velocity models was set to 2.5 km above sea level (highest elevation of MV) and the depth to the top of the underlying half space changed among models. Ideally all models should give similar final results –as long as the number and configuration of layers are the same. Thus

we also introduced variations in geometry by changing the number and thickness of layers. The number of layers of our starting models varied from 2 layers, simulating a simple earth structure, to 34 layers, simulating a more complex gradient-like geometry. The thickness of individual layers varied from 0.2 km, for models that simulated the velocity structure of the volcanic pile overlying a complex multi-layered crust and the Moho, to 33 km for simpler models that only included one layer for the volcanic pile overlying a single-layered crust and the Moho. With this we test the stability of locations of earthquakes and their origin times with respect to variability in velocity structure. The velocities of P-waves in our starting models varied from 2.07 km/s for shallow layers to 9.45 km/s at the Moho. The velocities of S-waves were obtained by specifying Vp/Vs ratios that ranged from 1.72 to 1.81.

Some of the starting models used were developed for other volcanoes in Alaska (Dixon et. al., 2003) and we also used modified versions of these models. The basic idea was to test a wide range of geometries and velocity distributions and to include somewhat extreme values of P and S-velocities to investigate the variability in earthquake locations and their errors. Additionally we investigated the dependence of the "best" one-dimensional model on both the starting values of velocities and the starting set of earthquakes.

6.4.2. Constraining the depths of earthquakes

To help constrain further the locations of earthquakes at MV, we computed model-independent estimates of the ratio of P- to S-wave velocity (V_p/V_s), origin time (t_o), and focal depth (Z). To do this, we used Wadati and Riznichenko diagrams (Wadati et al., 1933; Riznichenko, 1958). The Wadati diagram is based on a linear relationship between the difference in arrivals of P and S ($t_s - t_p$) and the arrival time of P (t_p):

$$t_p - t_o = T_p, \quad t_s - t_o = T_s. \qquad (1)$$

$$T_{p\text{-}s} = t_s - t_p = T_s - T_p \qquad (2)$$

where t_o is the origin time at the focus, t_p, and T_p are the arrival time and travel time of P-wave, respectively, t_s and T_s are the arrival time and travel time of S-wave, respectively, and $T_{p\text{-}s}$ is the difference in arrival between P and S-waves. If the velocities of P and S-waves, V_p and V_s, satisfy the following relation:

$$V_p/V_s = K \text{ (constant)} \qquad (3)$$

in the Earth's crust, then

$$T_s/T_p = V_p/V_s = K \qquad (4)$$

$$(T_{p\text{-}s})/T_p = (V_p/V_s) - 1 = K - 1 \qquad (5)$$

$$T_{p\text{-}s} = (K - 1)(t_p - t_o) \qquad (6)$$

Thus as long as V_p/V_s remains constant, $T_{p\text{-}s}$ is a linear function of t_p. By plotting $T_{p\text{-}s}$ versus t_p of a single earthquake measured at several stations, a good fit to a straight line is generally possible. The intercept of the best fitting line to the data with the abscissa gives $t_p(0) = t_o$, the origin time of the earthquake, and the slope is a function of the V_p/V_s ratio

$$\text{Slope} = K - 1 = V_p/V_s - 1 \qquad (7)$$

A typical Wadati diagram for an earthquake recorded at the MV seismograph network is shown in Figure 6.3a. In this manner we estimated V_p/V_s ratios from our 93 earthquakes.

The Riznichenko diagram is based on a linear relationship between the square of the travel time (T^2) and the square of epicentral distance (Δ^2) that is appropriate for close distances and relatively shallow focal depths (Nicholson and Simpson, 1985; Deichmann, 1987)

$$T^2 = \Delta^2/V_{av}^2 + H^2/V_{av}^2 \qquad (8)$$

where T is travel time (of P or S- waves, or the travel time measured for the separation between P and S waves), Δ is epicentral distance in km, H is focal depth, and V_{av} is the average half-space velocity of P or S-waves. A plot of T^2 versus Δ^2 can be fitted by a line whose slope is a function of V_{av}

$$\text{Slope} = 1/V_{av}^2 \qquad (9)$$

and an intercept that is a function of the vertical travel time of P or S -waves

$$t_z = H/V_{av} \qquad (10)$$

To compute travel times of P, S, and the velocity of separation of S-P waves, we use the origin times estimated from the Wadati diagram and use the epicentral distances to the stations that are computed during our best routine locations, which are usually considered reliable (Deichmann, 1987). In actuality, we used the epicentral distances for the earthquakes after relocation with the best velocity model found. The average horizontal error in the relocated earthquakes is 0.20 km (error in Δ), which results into typical error estimates of

H, $V_{av(P)}$ and $V_{av(S)}$ of H_{error}=±0.20 km, $V_{av(P)error}$=±0.015 km/s, and $V_{av(S)error}$=±0.009 km/s, respectively. Figure 6.3b shows a typical Riznichenko diagram for one earthquake at MV. If we include travel time information about S waves or S-P in the Riznichenko diagrams (instead of information about P-waves) we can obtain three different (not necessarily independent) estimates of focal depths to further constrain the locations of our group of earthquakes. The three values of focal depths and velocities for each earthquake obtained by using P, S, and S-P travel times in Riznichenko diagrams should in general be similar and provide an estimate of uncertainty in the parameters computed (Nicholson and Simpson, 1985).

6.4.3. Computation of Fault-Plane Solutions

We computed fault-plane solutions (FPS) for a group of 17 earthquakes with at least six first motion readings using the computer program FPFIT (Reasenberg and Oppenheimer, 1985). FPFIT performs a grid search over all possible values in strike, dip, and rake in the focal sphere to find the nodal planes that best explain the observed first motions polarities. As a measure of the distribution of observations over the focal sphere, FPFIT computes a quantity called Station Distribution Ratio (STDR), with values of STDR > 0.5 indicating relatively good coverage of the observations around the epicenter. The quality of a solution is also rated by the number of discrepant observations as well as the estimated spread in orientation of the nodal planes.

6.4.4. Changes in Stress Detected with the Cumulative Misfit Method

Our number of FPS available is low, and we cannot subdivide this dataset further and invert for stress tensor. Thus, we estimated changes in stress at MV indirectly, by cumulative misfit analysis. In this method the slip directions

estimated from a group of FPS are compared with the theoretical slip from a reference stress tensor (Wyss and Lu, 1995). The individual misfit of a FPS is the amount of rotation, around any arbitrary axis, that would be required to make the observed slip equal the predicted slip. A plot of cumulative misfit versus earthquake number sorted in space or time is then produced and changes in the slope could indicate changes in stress, provided that statistical significance is met. The statistical significance is evaluated in terms of the standard *t*-test, because of our small sample of FPS. The method initially applied to tectonic areas (e.g. Lu and Wyss, 1996) has more recently been applied to find spatial variations in stress at Mount St. Helens (Musumeci et al., 2000) and temporal-spatial changes in stress at Redoubt volcano, Alaska, (Sánchez et al., 2004).

6.4.5. Modeling of Coulomb Stress Changes Caused by Expansion of Vertical Dikes

The alignment of many quaternary cones at MV has been suggested as the surface expression of a dike or dike system that is elongated in the direction of maximum tectonic stress and opened in the direction of minimum compressive stress (Nakamura et al., 1977). With this framework model in mind, we modeled the region beneath MV as an isotropic, elastic half-space in which one or several buried vertical expanding dikes cause stress changes. The stress changes are computed by implementing the dislocation formulation of Okada (1992) and boundary element formulation of Crouch and Starfield (1983).

We varied the geometry of the problem by simulating expansion on a single vertical dike, a system of radial dikes that intersect at the vent, and a system of vertical dikes with various orientations. The lengths and widths of hypothetical dikes varied between 5 and 16 km, and between 6.5 and 12.5 km, respectively,

and all dikes were allowed to expand between 0.5m and 1m. The target depth for all calculations was set at 8.5 km (mid depth of relocated earthquakes). We incorporated typical values for Poisson's ratio (PR=0.25), Young's modulus ($E1$=8x10^5 bars), and apparent friction coefficient (μ'=0.4) in our calculations. We assumed a regional tectonic stress with maximum compression, σ_1, oriented 145° from north and dipping 10°, and uniform value of 100 bars from surface to target depth. The changes in Coulomb stress were calculated using the computer program Coulomb 2.**5** (Toda and Stein, 2002) and projected onto optimally oriented strike-slip, thrust, and normal faults.

6.5. Results

6.5.1. Velocity Model

We used 39 different starting velocity models and the same set of earthquakes in each case and ran VELEST inversions until convergence to a minimum average RMS was found. Figure 6.4 shows the final velocity models computed. During our VELEST searches for an optimal velocity model, a minimum RMS was usually found after a number of trials that varied between 10 and 55. The inset in Figure 6.4 shows an example of how convergence to a minimum RMS value is achieved after a certain number of trials. We found that several velocity models would also yield a low RMS value of 0.24 s, but only a modified version of the generalized model would minimize the RMS, GAP, ERH, and ERZ error estimates and produce the fastest convergence towards these values, thus minimizing the computational time. Tables 6.2 and 6.3 list the parameters of the minimum velocity model and the stations corrections, respectively.

The values of P and S corrections (Table 6.2) correlate well with the geology beneath the sites (Detterman et al., 1980, 1981). In general, the travel time data require that stations located on old geological units (e.g. VNKR and VNSG) have negative corrections (because of "fast" velocities resulting in early arrivals) and stations located on younger rocks (e.g. VNFG, VNNF, VNSW, VNWF) need positive corrections ("slow" velocities that give late arrivals). Among stations with the same sign for the correction we found that the values agree well with the relative age of the surface units. For instance, stations VNFG and VNNF are on a cinder cone and a debris-flow deposit, respectively, and their values of corrections are comparable; and stations VNSW and VNWF are located on andesite and dacite lava flows of the same age respectively, and their correction values agree and are smaller that those of stations VNSW and VNNF. The exception is station VNHG, which is located on young geological units but requires a negative P-correction. Further, the signs of P and S-corrections are different. Station VNSS is located on a cinder cone, but no correction was computed because it was chosen as the reference station. From our results, however, we anticipate that station VNSS may require a positive value similar to VNNF or VNFG, in the range 0.25 - 0.44 s. Thus if the value of the VNSS correction is biased, all origin times will be biased by the magnitude of the VNNS bias.

To investigate how the final velocity model varied with the initial set of preliminary locations, we created ten subsets of 70 earthquakes each by bootstrap resampling of our original data set and ran VELEST inversions for optimal velocities keeping the starting model fixed. Figure 6.5 shows the results. The computed final velocities changed as the earthquake data set varied. We found that the final velocity distributions computed from several initial earthquake groups varied depending on depth and that the effect of using a

particular subset of earthquakes (instead of the entire data set) accounts for as much as 10% of the variability in velocity.

Because for each starting model a number of VELEST trials are required to achieve the smallest RMS (each trial represents a different velocity model tested), a total of 3287 different velocity models were tested during our procedure. Finally, the earthquakes were relocated using the new model with station corrections. Figure 6.6a shows the map and cross-section of relocated earthquakes. The formally computed average horizontal and vertical errors are 0.2 and 0.4 km, respectively. These are significant improvements over the starting values of 1.1 km and 8.4 km. Some of this improvement, however, may mean that the location errors are somewhat scaled by misfit, resulting from increasing the number of parameters in our modeling with VELEST. To check the effect of the stations corrections alone, we relocated the earthquakes using the original model and the new station corrections. In this case we found that the average horizontal and vertical errors in locations were 1.1 km and 9.3 km, respectively. We suggest that the relative absence of seismicity to the south and southeast of MV is not an artifact caused by stations on the south being used less often in the locations. Figure 6.6b shows a bar plot of the number of P and S arrivals used in the location of our earthquake dataset.

6.5.2. Focal Depths of Earthquakes

Our analysis of focal depths using Wadati-Riznichenko diagrams showed no important differences from the depths obtained with the new velocity model although the earthquakes appear slightly more distributed in depth. Because we have made the simplifying assumptions of a constant V_p/V_s ratio and constant V_p velocity in the crust, the focal depths estimated by this method could be overestimated by a few km. (Deichmann, 1987). We estimate that the average

uncertainty in depths is ~1.8 km. Nevertheless this method is useful to verify our model-dependent locations and to contribute to the reliability of the results.

6.5.3. First-order vertical and lateral variations of V_p/V_s

The new velocity model found in our VELEST inversions and the estimates of hypocentral depths (from Riznichenko diagrams) and V_p/V_s (from Wadati plots) allow us to illuminate some features otherwise hidden in the preliminary locations. Figure 6.7 shows plots of V_p/V_s versus depth with values derived from Wadati-Riznichenko diagrams and suggested by the minimum 1D velocity model from VELEST inversions. The line plot may represent an averaged or smoothed version of the somewhat noisier Wadati-Riznichenko values (scatter plot) and allows a simpler appreciation of the changes. The V_p/V_s ratio initially increases from 1.73 to 1.88 between 0 and 4 km depth, then decreases to a minimum value of 1.38 at 10 km, increases again to 1.65 at 15 km depth and roughly stabilizes down to a depth of 20 km. Below 20 km the trends in both plots are opposite, and the number of earthquakes is too small to derive conclusions. The average values of V_p/V_s found by the two methods indicate that our new velocity model may underestimate the average V_p/V_s ratio. Our data was not suitable for a reliable mapping of lateral variations of V_p/V_s.

6.5.4. Fault-Plane Solutions

The computed FPS by FPFIT are shown in Figure 6.8, and the relevant parameters of each solution are listed in Table 6.4. We found mostly oblique thrust motions (12 events), three cases of oblique normal faulting, and two cases of nearly pure strike-slip. The orientation of P and T-axes show noticeable variation as well.

6.5.5 Spatial Variations in Stress Found with the Cumulative Misfit Method

We suggest that the apparent variety of FPS could indicate variations in stress as a function of space. In this context, we compared the FPS with a hypothetical stress tensor that we assume to be similar to the tectonic stress, with a maximum compressive stress, σ_1, being sub-horizontal (plunge=10°), and with an azimuth of 145° (Nakamura et al., 1977). Figure 6.9a shows the plots of cumulative misfit versus earthquake number ordered by depth, latitude and longitude.

For events ordered by depth, from shallow to deep, there is a change in stress significant at the 99% level at earthquake number 4 (depth=2.2 km) after which the cumulative misfit increases at a constant rate. We note that the Vp/Vs ratio estimated for shallow earthquakes appear to differ from deeper earthquakes, in the range 2.5-10 km (Figure 6.7). Another change in cumulative misfit is apparent at earthquake number 15 (depth=9.2 m), but the number of deeper earthquakes is too small to resolve changes.

For events ordered by latitude (from south to north) we found changes in stress at earthquakes numbers 4 (latitude=56.12°), 8 (latitude=56.23°), and 12 (latitude=56.33°). These changes in slope on the cumulative misfit curve are significant at the 99% level in the first two cases and at the 90% level for the northernmost segment.

For events sorted by longitude (from west to east) we found two changes in stress at earthquakes numbers 8 (longitude= -159.51°) and 14 (longitude= -159.12°). These changes are significant at the 95% and 90% levels, respectively.

To test the dependence of the suggested changes in slope of the cumulative misfit curves with respect to the reference tensor chosen, we repeated the misfit calculations using 8 different reference stress tensors in which the orientation of σ_1 varied between 110° and 180°, stepping 10° each time. We found the same changes in slope in the cumulative misfit curves (Figure 6.9b).

6.5.6. Modeling of Coulomb Stress Changes

Figures 6.10a, b and c, show contour maps of change in Coulomb Failure Criterion (ΔCFC) predicted by a expanding single vertical dike. In all cases large positive and negative changes in stress are predicted in the immediate vicinity, and in particular, at the tips of the dike. This is because we make the unrealistic assumption of uniform expansion. The values of ΔCFC decay quickly to ±2 bars within a few tens of kilometers from the stress source.

The model predicts that strike-slip faulting is favored on the lobe-shaped areas radiating from the tips of the dike and that the positive changes in stress are elongated in the direction of regional stress (Figure 6.10a). Strike-slip is not favored off to the sides of the dike, with lobes of negative stress change elongated in the direction roughly perpendicular to tectonic stress. Only three of our FPS with strike-slip component of motion are located on regions of positive ΔCFC, and seven FPS with some strike-slip component fall in regions of negative stress change.

For thrust faults, slip is favored everywhere except on the regions of negative ΔCFC at the tips and along the dike (Figure 6.10b). Six of our FPS indicative of thrust faulting are located in a region of positive stress change, and

seven FPS indicative of thrust faulting fall within regions of negative stress change.

For normal faults the model predicts that slip is favored in regions of similar shape and location to those for strike-slip faults, but the regions of negative ΔCFC are non symmetric and larger on the SW quadrant (Figure 6.10c). Two of our normal FPS fall in a positive region for stress changes and they may be well constrained. Two of our FPS indicative of normal motion, however, fall in a negative region for stress changes, and these earthquakes are located inside the caldera and close to the active vent. This negative result may indicate a complex local stress field, or alternatively, that the caldera and vent regions are anomalous and make it difficult to correctly assess the first motion polarities.

Finally, we also modeled the changes in stress caused by a system of one large dike connected to smaller radial dikes intersecting at the vent and obtained similar spatial patterns of stress changes.

6.6. Discussion

We followed a trial-and-error approach to devise a preliminary one-dimensional velocity model with station corrections for MV, based on a group of VT earthquakes, and investigated how their locations varied with different velocity models. We found that the new velocity model and station corrections minimize the RMS of travel times and the average horizontal and vertical errors. Because the epicentral locations showed stability with respect to a variety of velocity models tested, we suggest that they are reasonably well constrained.

By using Wadati and Riznicenko diagrams the depths of earthquakes have been constrained to within a few kilometers or less. We note that the main difference between the hypocenters constrained with the new velocity model and the depths constrained with the Wadati-Riznichenko diagrams are the uncertainty estimates, which are larger in the latter case. At the same time we derived model-independent estimates of the Vp/Vs ratio. For the best constrained focal depths in the range 0 to 20 km, we found that Vp/Vs decreases with depth and is in good agreement with the Vp/Vs found in the VELEST inversions. Decreases in Vp/Vs ratio with depth have been reported in other regions (see for example Nicholson and Simpson, 1985) and may indicate first-order variations in velocity structure.

We applied the Cumulative Misfit method to a group of 17 FPS computed with FPFIT and found spatial stress changes beneath and around MV. The significant changes in slope of cumulative misfit curves indicate that the stress regime in the area delimited by latitudes 56.12° and 56.33° and between longitudes -159.51° and -159.12° (Figures 6.9, 6.10, and 6.11) is different from the surrounding region when a particular set of reference stress tensors, with σ_1 oriented in the direction of principal tectonic stress, are used. The region of different stress behavior includes the caldera of MV plus some adjacent areas to the north and east. We also found differences in stress with depth, with shallow events above 2.2 km being different from those shocks down to a depth of 9.2 km (Figure 6.9). This correlates well with apparent difference in Vp/Vs ratio from shallow to deeper events (Figure 6.7).

We modeled the source of local stress at MV as magma system composed of a uniformly expanding dike or group of radial dikes with various orientations, sizes, and amounts of opening and found that not all of our FPS fall in the appropriate regions of positive ΔCFC. We thus infer that our model may not be

completely appropriate to explain the observed FPS data. On the other hand, the lack of information on horizontal components of ground motion and the small number of first motion readings available to compute FPS implies that we cannot constrain the faulting style with desirable confidence. This situation can be improved in the future with the deployment of more appropriate instrumentation (three component seismometers). We think that stress sources represented by inflating dike or system of radial dikes are realistic in light of tectonic considerations (Nakamura et al., 1977). Additionally we found that the regions of greatest ΔCFC are included in the anomalous stress area found with the Cumulative Misfit method.

We observe that the earthquakes are uncommon within the caldera and occur mostly off to the sides of the alignment of Quaternary cones in the SE-NW direction (Figure 6.6). The relative absence of seismicity within the caldera is not explained by any of the following factors: 1) Configuration of the seismograph network, 2) Certain stations being less used in the location of earthquakes, or 3) Artifacts of the velocity model. The Alaska Volcano Observatory operates 140 to 160 permanent seismograph stations, distributed into 19 sub networks most of which have similar geometry and numbers of stations (Dixon et al., 2003). We plotted the preliminary locations of earthquakes at all seismically monitored volcanoes in Alaska for the period August 2002 to September 2004 and observed that MV is one of three volcanoes (the others are Aniakchak and Kanaga volcanoes), with a network of four or more stations around the summit, which shows low occurrence of volcano-tectonic seismicity close to the active vent. Because this may be translated into a probability of $p \sim 0.19$ of a volcano having relative absence of seismicity close to the vent, we infer that this represents a rare situation and suggest that the distribution of seismicity at MV is not an artifact of network configuration. We used a total of 934 P and S-phase arrivals in our VELEST

search for velocity models, and stations VNKR and VNSG were used as much as stations in the other flanks (Figure 6.6b). Thus we think that the spatial distribution of seismicity is not caused by lack of phase picks at certain stations. Also, because the epicenters did not switch significantly in position among many velocity models tested, we infer that the locations are well constrained and their spatial distribution is not an artifact of the velocity model.

Because the earthquakes locate preferably off to the sides of the area of quaternary cones that includes the active vent, we suggest that the seismicity at MV is mostly driven by stress changes caused by activity beneath the volcano. Perhaps magma intrudes in a dike or dike system that opens perpendicularly to the direction of plate convergence, increases stresses in the surrounding areas and causes faults to move (Figure 6.11). Finally we note that MV has had effusive eruptions as recent as 1995 and is undergoing continuous explosive activity at the time of this writing (October 2004).

6.7. Conclusions

A new velocity model with station corrections was derived for MV. The new velocity model is composed of 8 layers over a half space and Vp/Vs ratio that varies with depth. The epicenters of a group of 93 volcano-tectonic earthquakes were found to be reasonably stable when located with many models. The focal depths of earthquakes at MV are constrained to within one kilometer or less with the use of Wadati-Riznichenko diagrams. We found that the earthquakes are uncommon near the active cone and within the caldera and persistently locate off to the sides of the alignment of quaternary cones. Our results from relocations of VT earthquakes, computation of Vp/Vs, Cumulative Misfit of FPS, and Coulomb stress changes due to a uniformly opening dike or system of radial dikes all indicate that the caldera region exhibits variable behavior in

many respects. We suggest that the magmatic system beneath MV may be composed of a dike or system of radial dikes whose pressure variations drive the seismicity in the surrounding area by imposing stress on pre-existing faults.

6.8. Acknowledgements

The author wish to thank E. Kissling and S. Husen for help with the computer program VELEST. S. McNutt, J. Caplan-Auerbach, J. Power, E. Brodsky, Steve Estes, D. Christensen, J. Freymueller provided valuable discussion, comments and suggestions to improve the manuscript. J. Horrillo and C. Searcy greatly helped with MATLAB and PERL scripting. S. DeAngelis helped in the preparation of some figures. This work was supported by the Alaska Volcano Observatory and the U.S. Geological Survey (USGS), as part of their Volcano Hazards Program, and by additional funds by the State of Alaska.

6.9. Figures

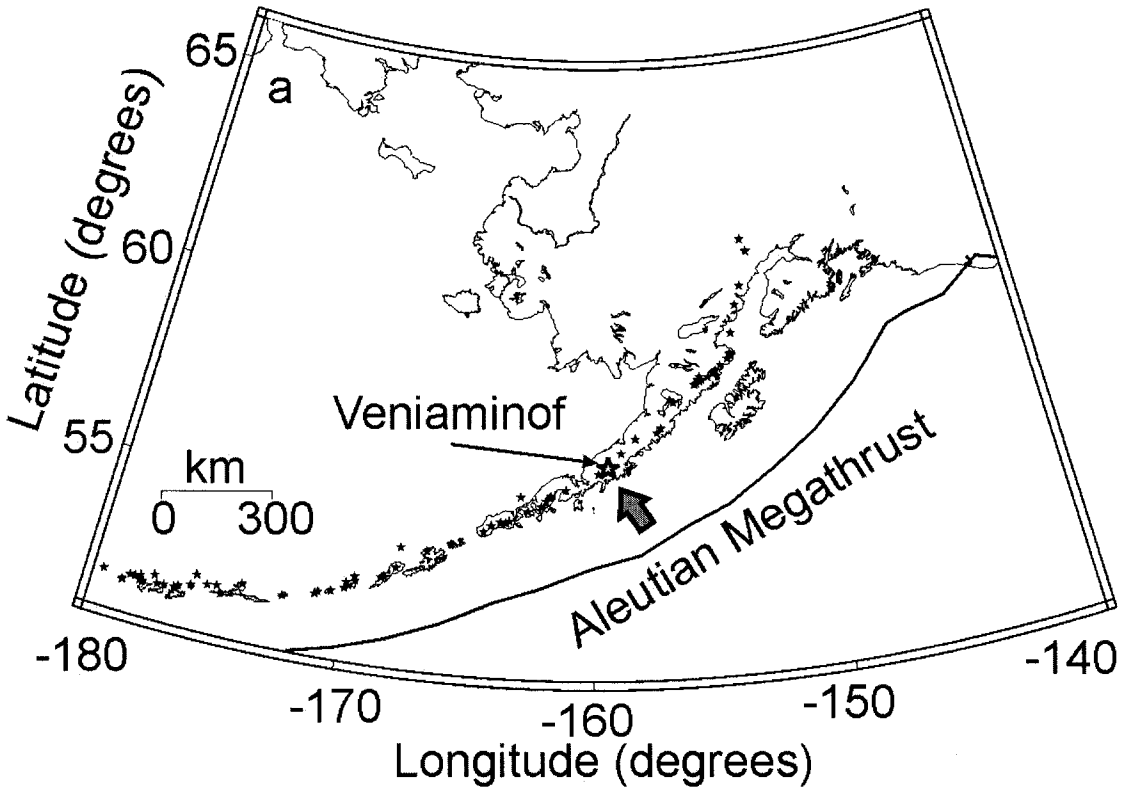

Figure 6.1a. Location map for MV. Map of Alaska showing the location of MV (big white star) and other volcanoes in Alaska (small black stars). The gray arrow indicates the direction of tectonic stress (from Nakamura et al., 1977).

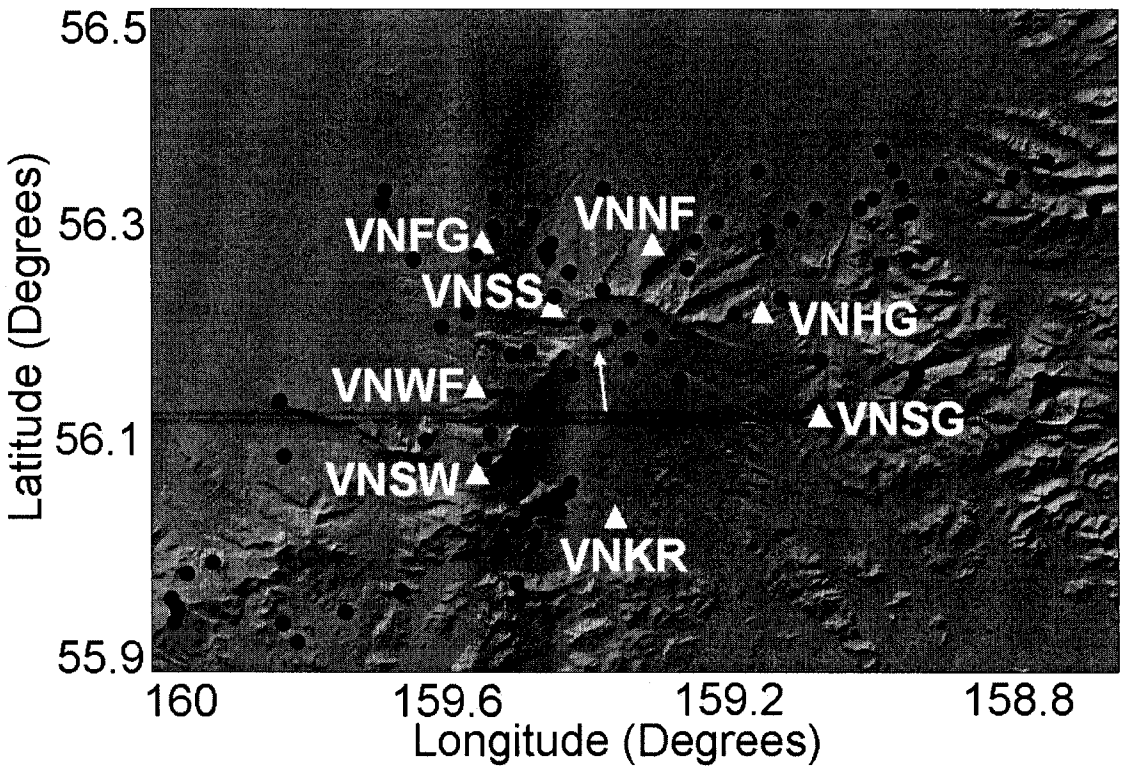

Figure 6.1b. Map of seismograph stations at MV. Shaded-relief image of MV showing the topography (Courtesy of NASA/JPL). The arrow points to the active vent. Note the alignment of cinder cones in the southeast-northwest direction, a feature that has been suggested to represent the surface expression of a dike or system of dikes, elongated in the direction of maximum tectonic stress and an opening in the direction of minimum tectonic stress (Nakamura et al., 1977). Triangles mark the locations of seismograph stations. Black circles mark the preliminary epicenters of earthquakes used in this study.

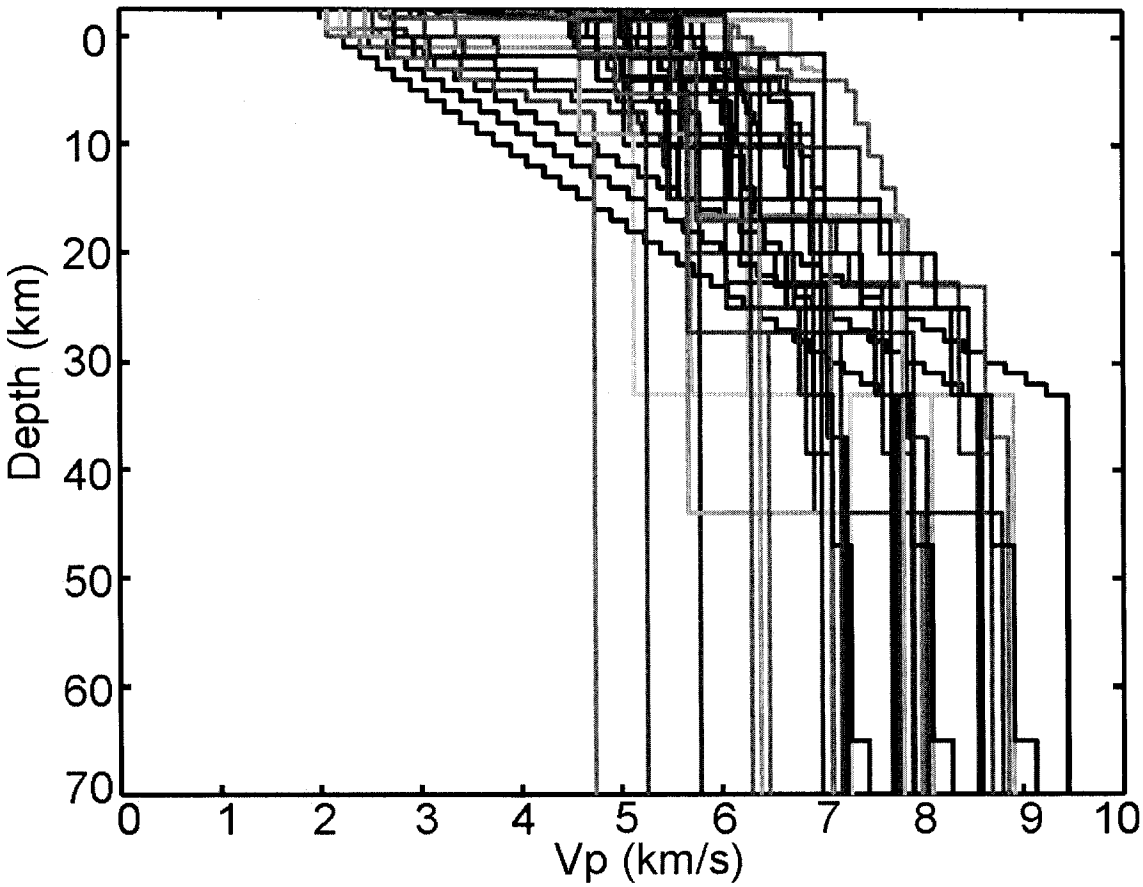

Figure 6.2. Initial velocity models. Plots of P-wave velocity versus depth showing the set of 39 initial velocity models. A basic set of 13 velocity models was formed with slightly modified versions of models used to locate earthquakes at Alaskan volcanoes. Additional velocity models were created by systematical decrease and increase of the velocities in each basic model by 10%, resulting in a set of 39 different starting models. See Dixon et al., (2003) for descriptions of the models.

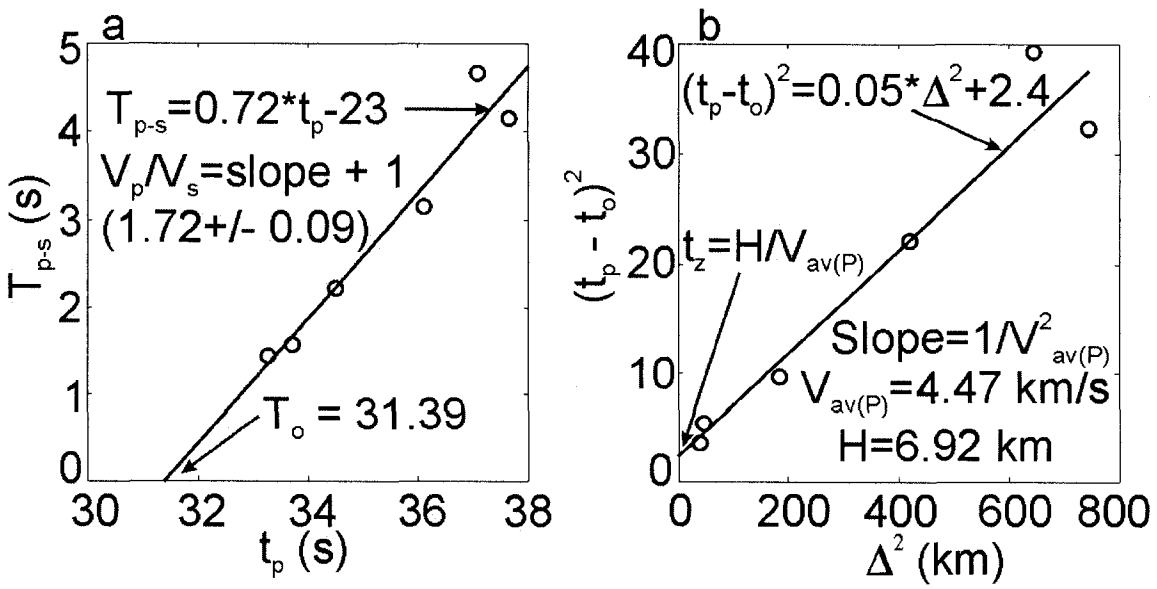

Figure 6.3. Typical Wadati and Riznichenko diagrams. (a) Wadati diagram for an earthquake recorded by the Mt. Veniaminof seismograph network. Hollow circles represent the values of Tp-s (seconds) versus tp (seconds) for the same event at six different stations. The solid line is the least squares best fit to the data, from which the Vp/Vs (slope) and To values (tp-intersect) can be estimated. (b) Riznichenko diagram for the same earthquake arrival time data plotted in (a). Hollow circles may represent the squares of travel times for P, S, or S-P (seconds) versus the square of the epicentral distance (km). The values of origin time and epicentral distances are obtained from Wadati diagrams, and from the best preliminary locations, respectively.

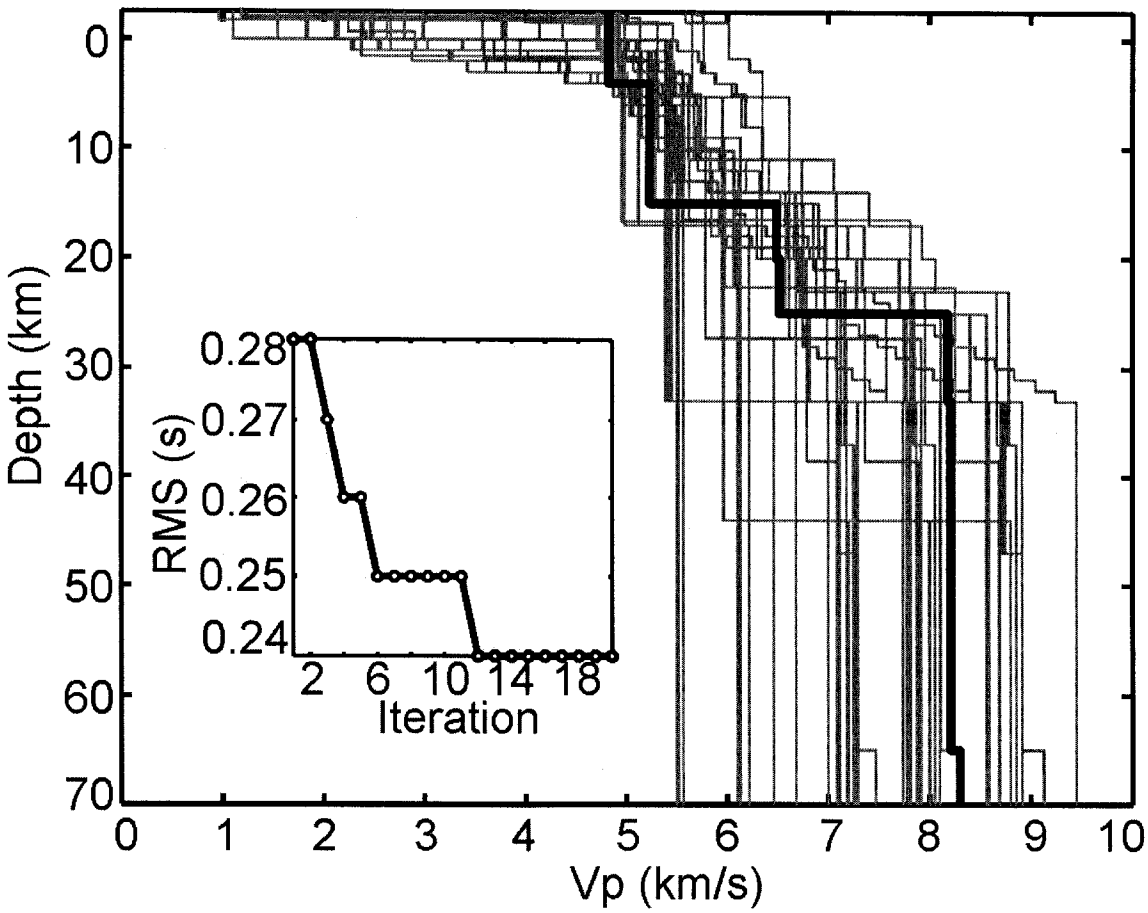

Figure 6.4. Final velocity models. Plots of P-wave velocity versus depth showing the final velocity distributions obtained by multiple VELEST runs. A thick black line represents the velocity model that minimizes the average RMS, ERH and ERZ for all 93 earthquakes. This minimum velocity model resulted from the generalized model as starting model. The inset shows a plot of average RMS versus iteration number for all the VELEST runs that resulted in our minimum model.

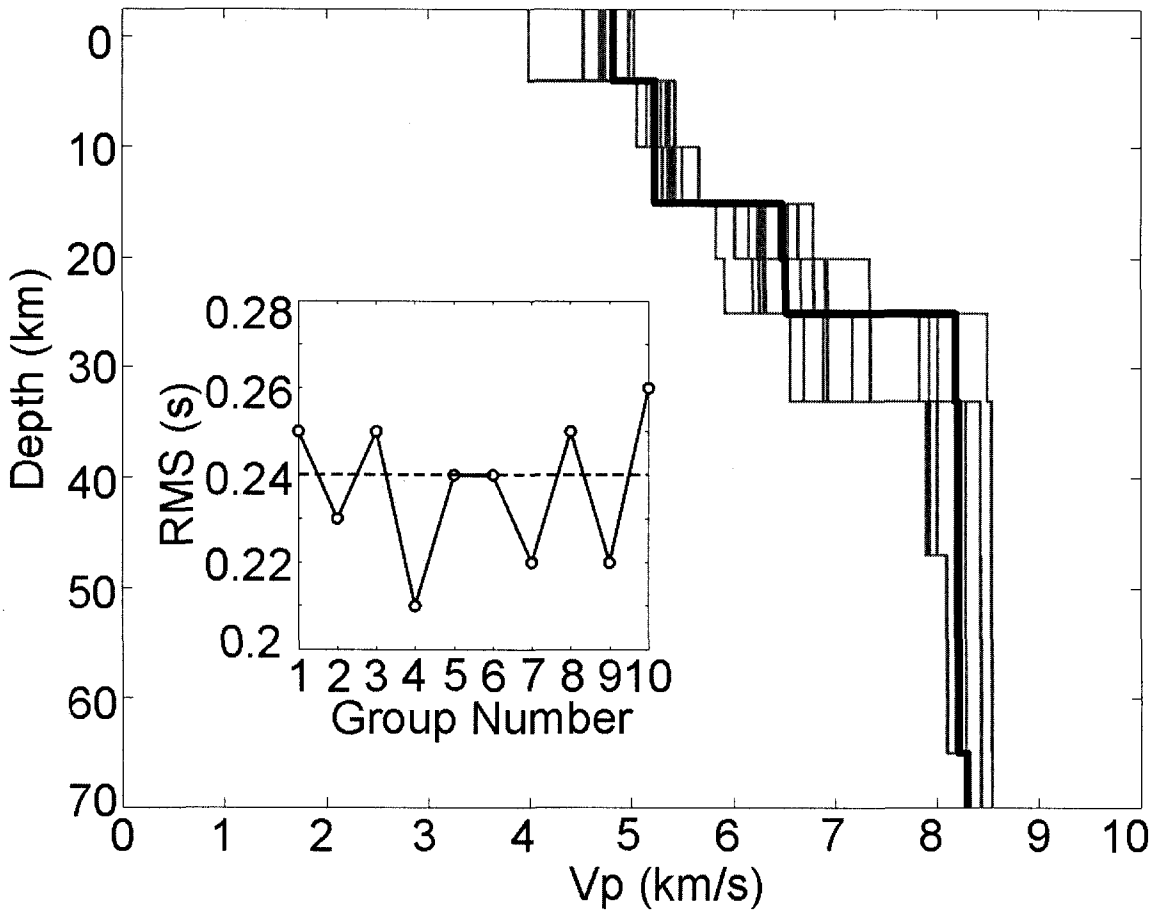

Figure 6.5. Tests with varying earthquake datasets. Final velocity models derived from multiple VELEST runs using 10 randomly selected groups of earthquakes and a fixed starting model. The groups of earthquakes were created by bootstrap resampling of the original data set. The generalized model was used as starting velocity model in all cases. Thin gray lines: results from the 10 random groups of earthquakes, thick solid line: optimal velocity model from the entire set of earthquakes. The inset shows a plot of average RMS versus random group number. Dashed horizontal line: average RMS from the optimal velocity model.

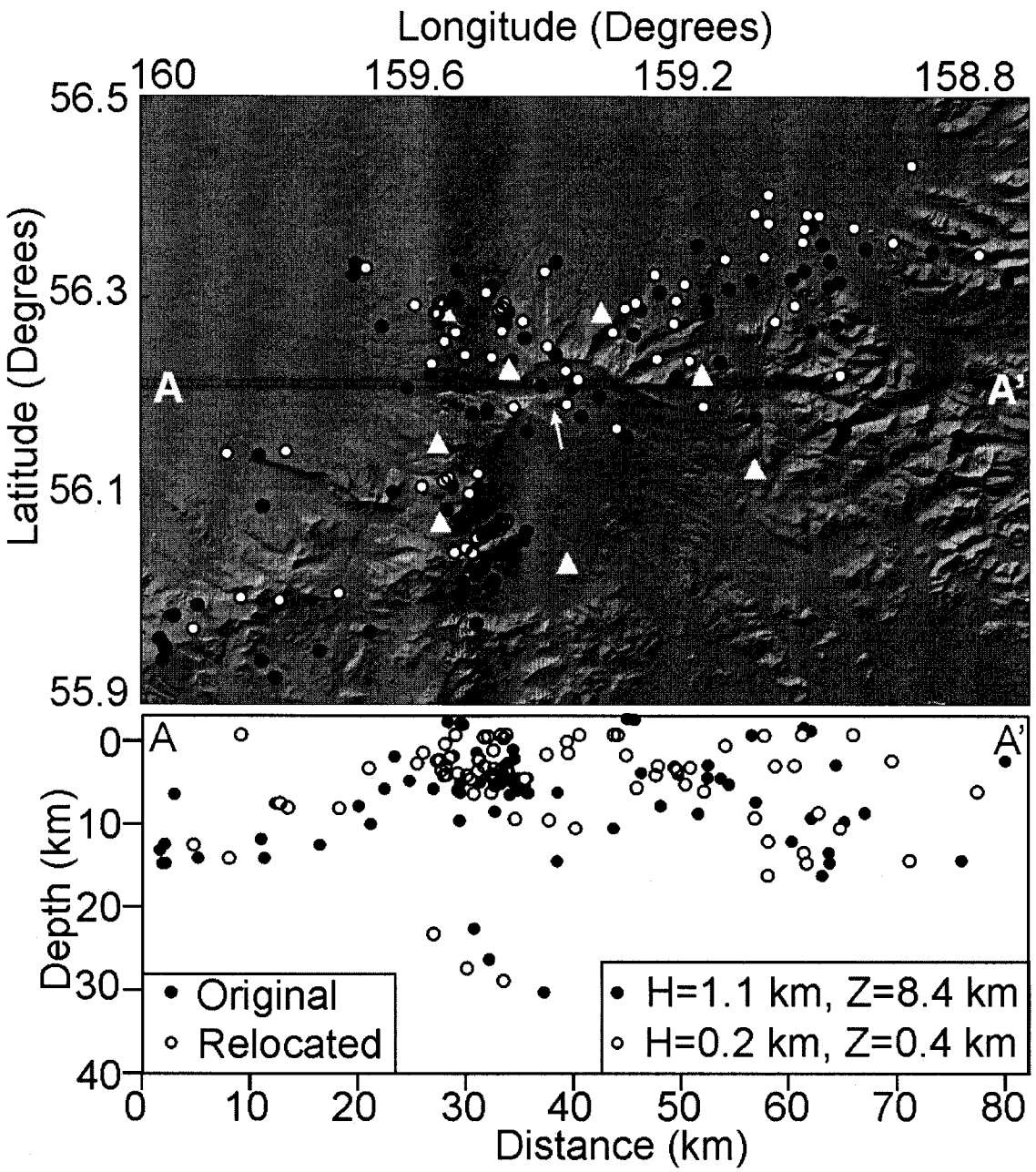

Figure 6.6a. Earthquake relocations at MV. Map (top) and cross-section A-A' (bottom) views of Mt. Veniaminof showing the locations of earthquakes obtained with the new velocity model (white circles) along with the original locations (black circles). H and Z indicate the average error estimates in the horizontal and vertical directions, respectively. Other conventions as in Figure 6.1b.

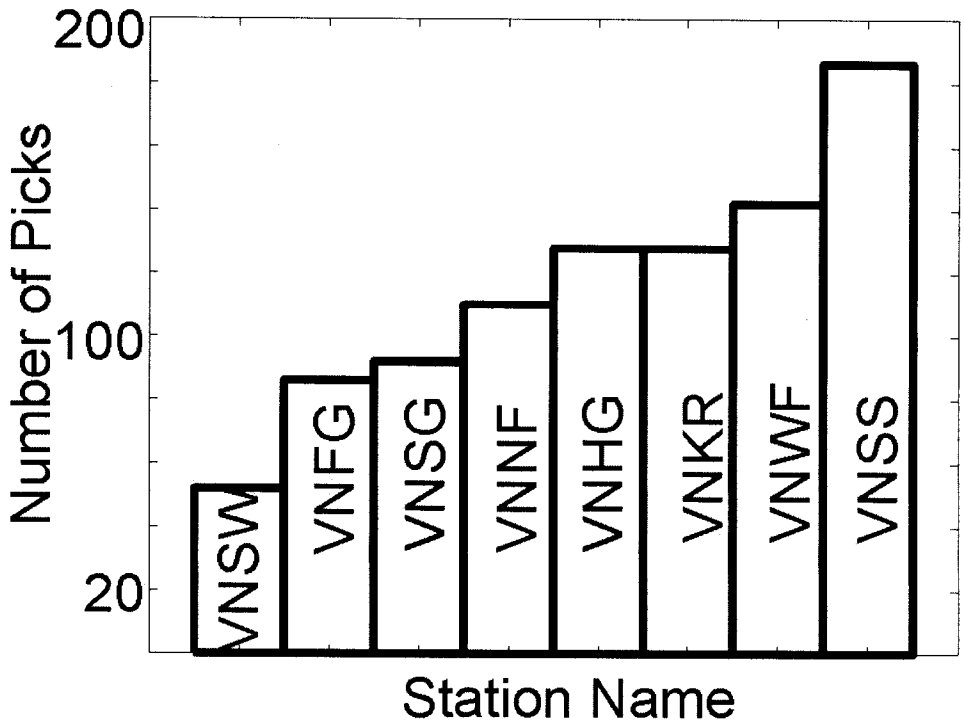

Figure 6.6b. Bar plot of number of picks per station. Bar plot of the total number of P and S-wave arrivals of earthquakes per station. A total of 934 phase arrivals were used.

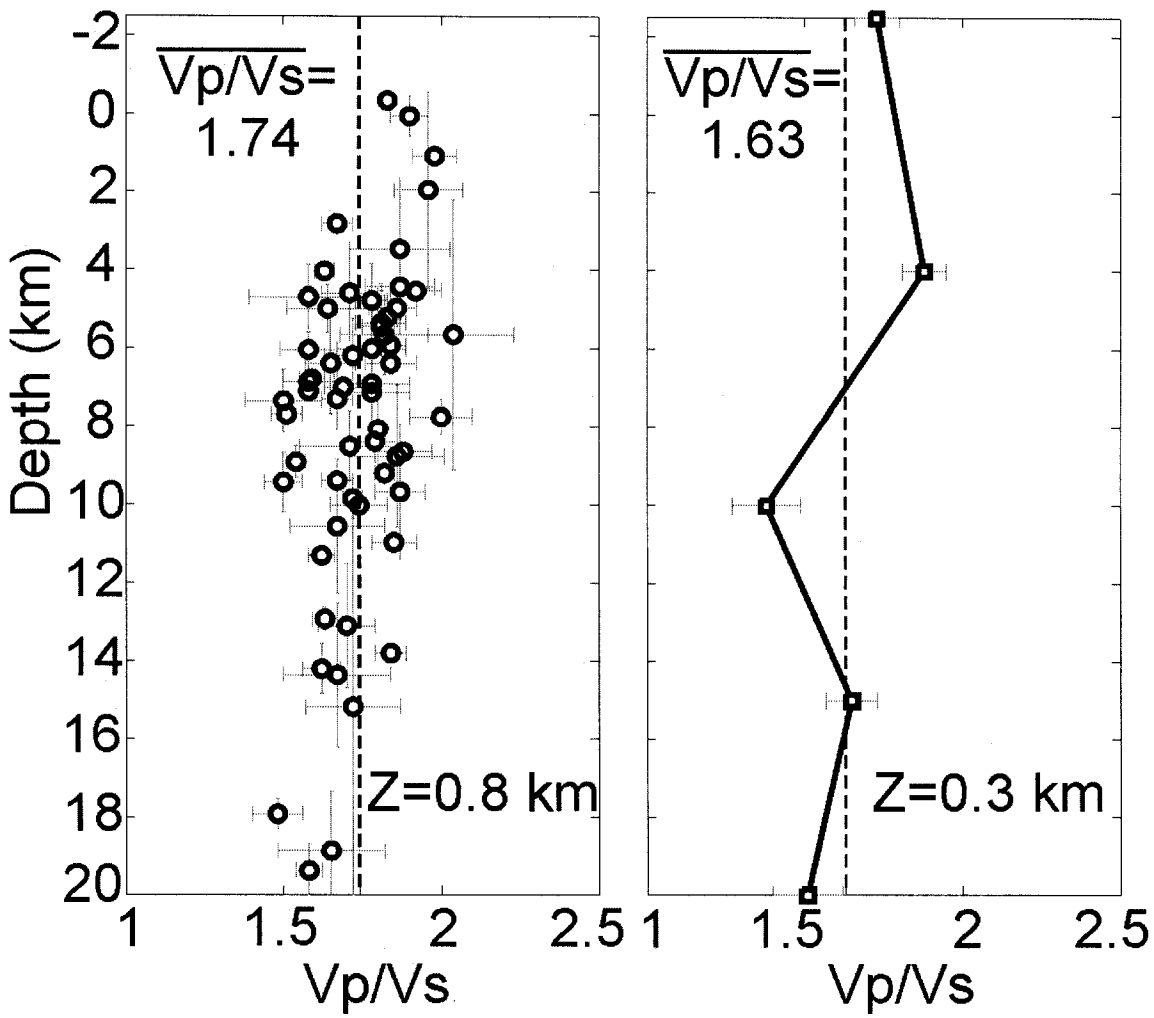

Figure 6.7. Vp/Vs versus depth at MV. Plots of Vp/Vs versus depth for earthquakes with values estimated from Wadati-Riznichenko diagrams (left) and from the new velocity model (right). A vertical dashed line indicates the average Vp/Vs values in each case. Other conventions as in Figure 6.6a.

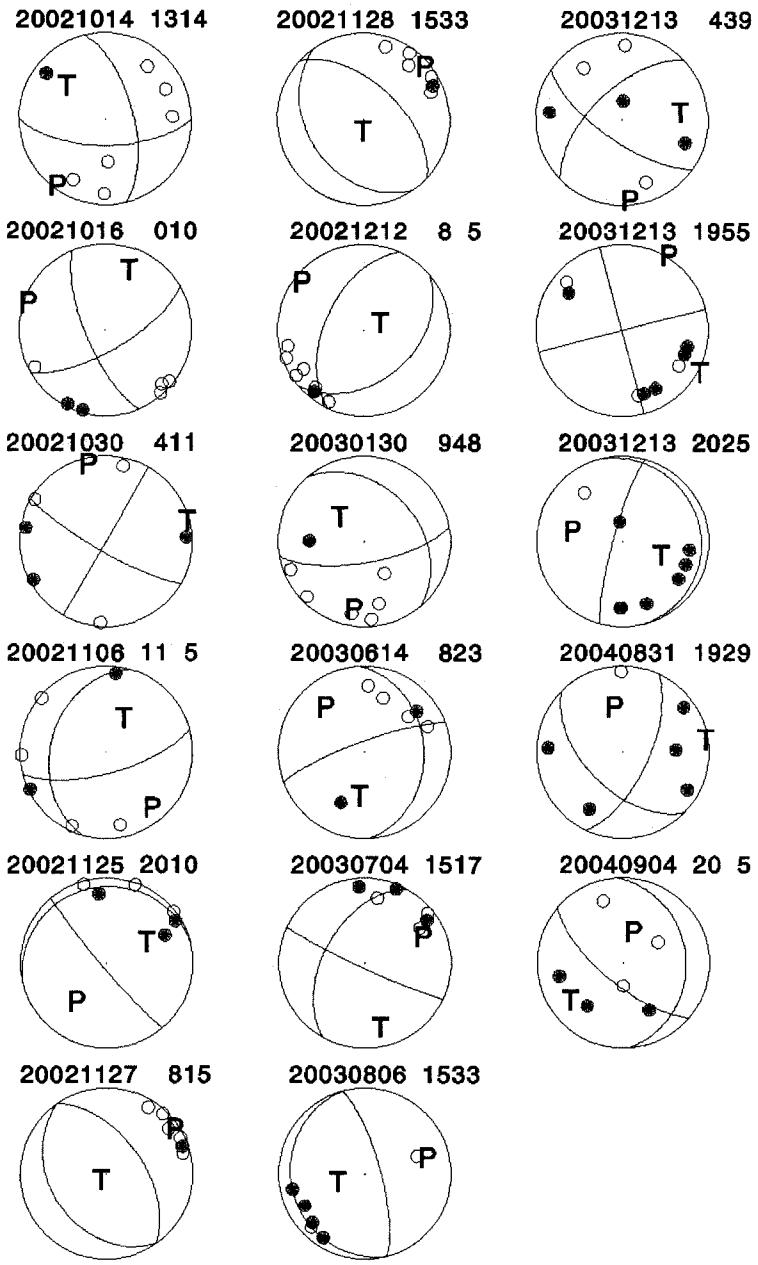

Figure 6.8. Fault-plane solutions at MV. Lower hemisphere projections of FPS computed with FPFIT. White and black solid circles represent dilatations and compressions, respectively. P=pressure axis, T=tension axis. The date and time (YYMMDD HH:MM) of the earthquake are indicated on top of each pair of solutions. See table 6.3 for a listing of the relevant parameters in each solution.

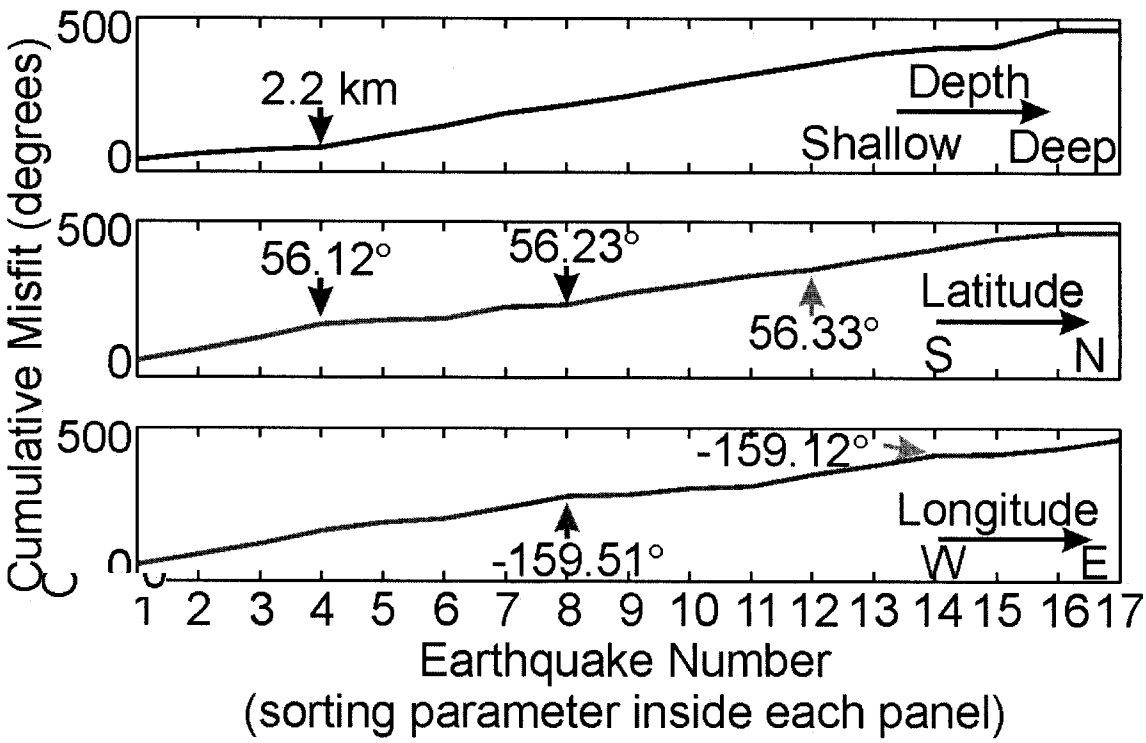

Figure 6.9a. Results of misfit analysis. Plots of cumulative misfit versus earthquake number, sorted by depth (top), latitude (middle), and longitude (bottom). Arrows mark the point where a significant change in slope is detected. Black, dark gray, and light gray arrows indicate stress changes detected at the 99%, 95%, and 90% confidence level, respectively, as evaluated by the *t*-test.

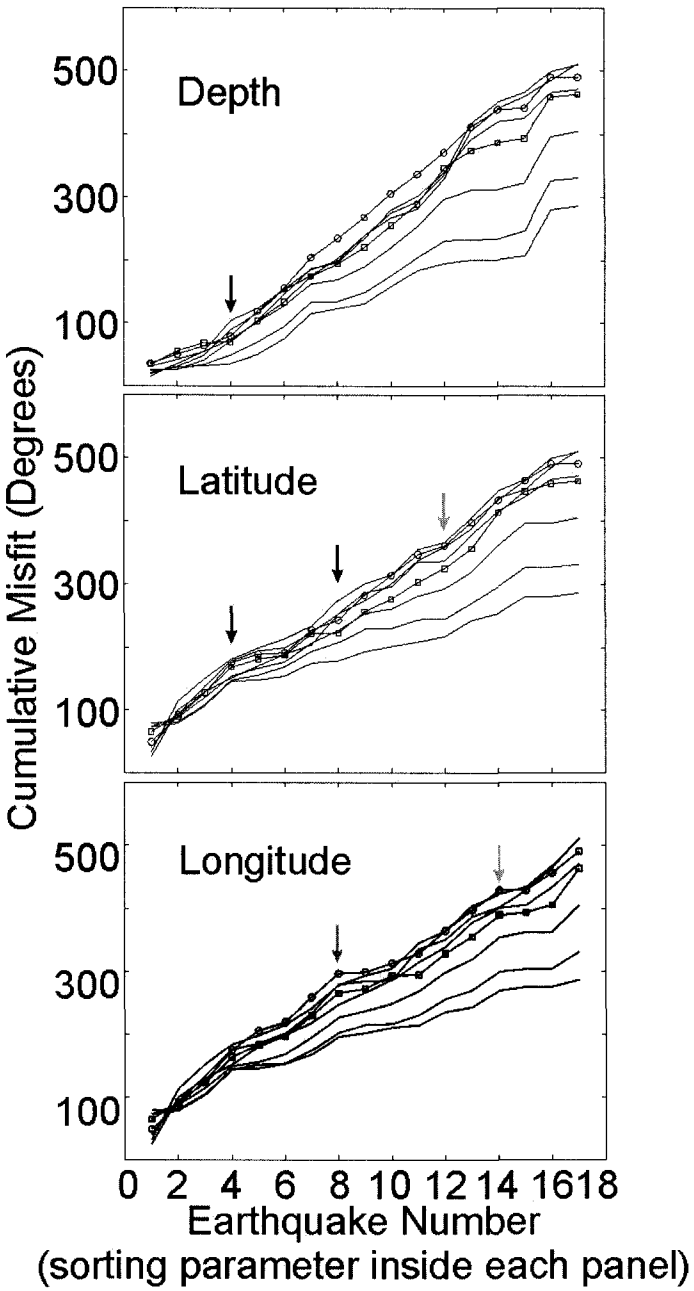

Figure 6.9b. Stress changes and reference tensors. Plots of cumulative misfit versus earthquake number, sorted by the parameter indicated inside each panel, for a set of eight reference tensors with azimuth of σ_1 varying between 110°-180°. Circles and squares indicate the results for azimuths of 140° and 150°. In general, the cumulative misfit decreases as the azimuth of σ_1 departs from the suggested orientation of 145° (Nakamura et al., 1977). Conventions as in Figure 6.9a.

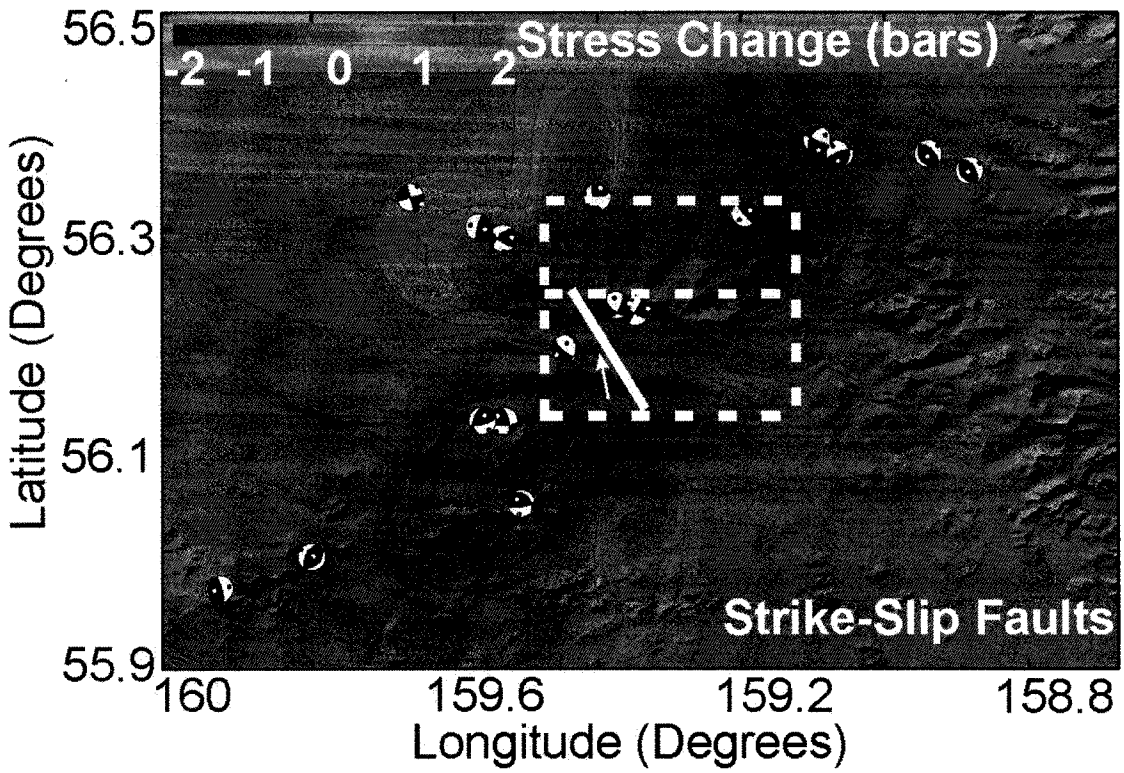

Figure 6.10a. Stress changes projected on strike-slip faults. Map view of stress changes caused by expansion of a dike (solid white line) embedded In an elastic half-space. Color gradients indicate the change In Coulomb stress (ΔCFC, negative values=discouraging failure, positive values=facilitating failure) at a depth of 8.5 km projected on optimally oriented strike-slip faults. Calculations were performed using Coulomb 2.5 (Toda and Stein, 2002), assuming regional stress compression of 100 bars oriented 145° clockwise from north. Assumed values for Earth parameters are: Poisson's ratio (*PR*)=0.25, Young's modulus (*E*) =$8x10^5$ bars, shear modulus (*G*)=*E*/(2(1+*PR*))=$3.2x10^5$ bars, and apparent friction coefficient (μ'=0.4). The fault-plane solutions are those shown in Figure 6.8 (red quadrants=compression, white quadrants=dilatation). Other conventions as in Figures 6.1b, and 6.7b. Parameters of hypothetical dike are: length=16 km, width=12.5 km, (top of dike is at sea level). Topography: SRTM data courtesy of NASA/JPL.

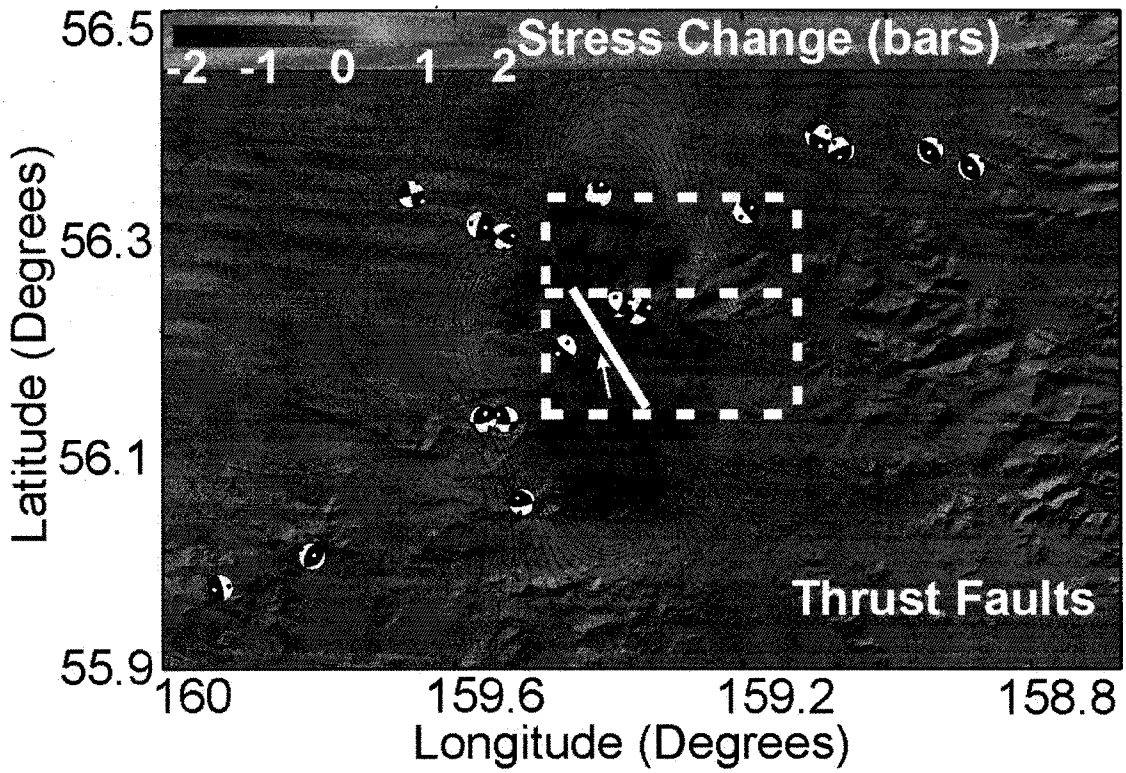

Figure 6.10b. Stress changes projected on thrust faults. Same as Figure 6.10a for stress changes projected on optimally oriented thrust faults. Conventions as in Figure 6.10a. Topography: SRTM data courtesy of NASA/JPL.

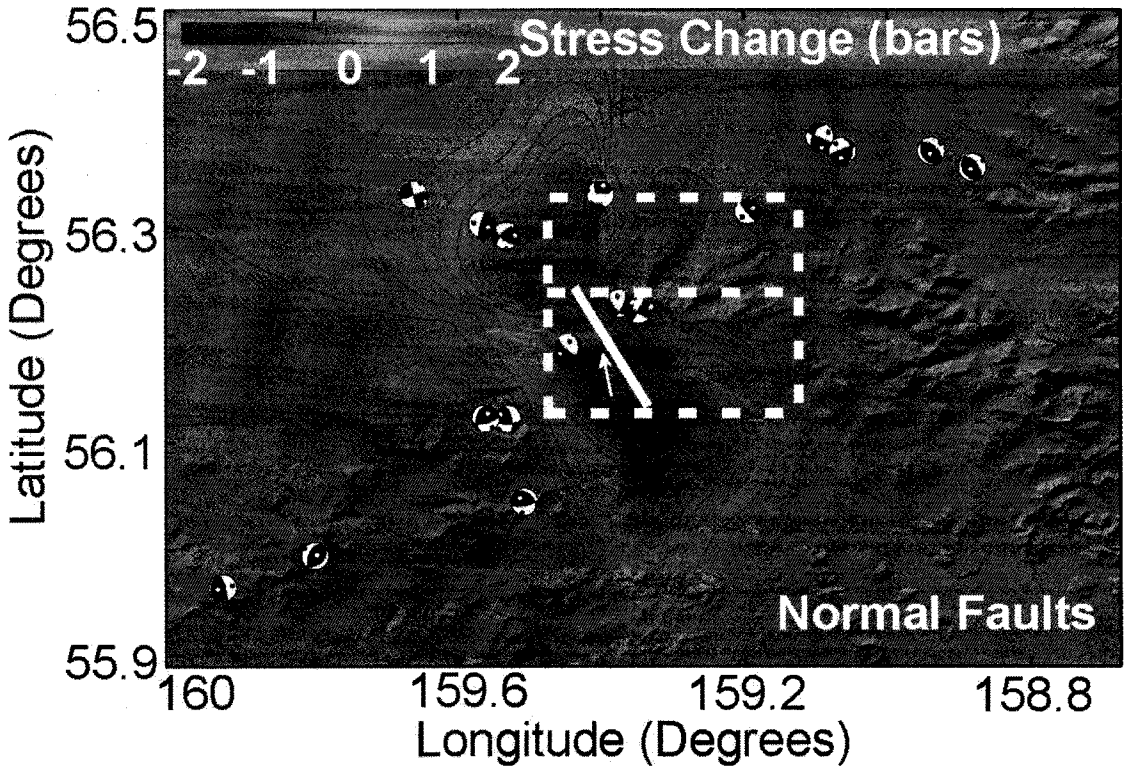

Figure 6.10c. Stress changes projected on normal faults. Same as Figure 6.10a for stress changes projected on optimally oriented normal faults. Conventions as in Figure 6.10a. Topography: SRTM data courtesy of NASA/JPL.

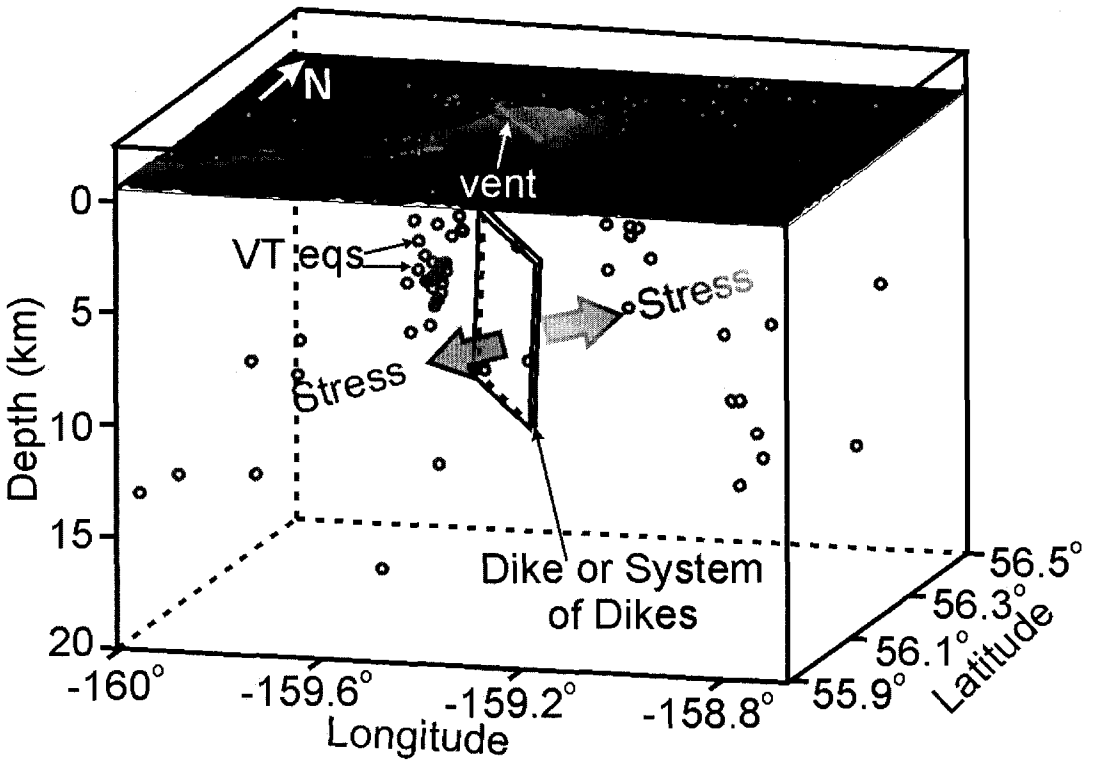

Figure 6.11. Conceptual model for VT seismicity at MV. Schematic view of a vertical dike whose opening imposes stress in the adjacent regions and causes faults to move. Circles mark earthquakes hypocenters (projected on the surface as dots). Large gray arrows indicate the direction of dike opening. The surface projection of the dike is marked by a thick purple line under the active vent.

6.10. Tables

Table 6.1. Generalized Velocity Model (Fogleman et. al., 1993)

Depth of Top of Layer (km)	Vp (km/s)	Vp/Vs
-3.0	5.3	1.78
4.0	5.6	1.78
10.0	6.2	1.78
15.0	6.9	1.78
20.0	7.4	1.78
25.0	7.7	1.78
33.0	7.9	1.78
45.0	8.1	1.78
65.0	8.3	1.78

*Depths referred to sea level, negative depths are elevations above sea level.

Table 6.2. Minimum 1D Velocity model for Mt. Veniaminof

Depth of Top of Layer (km)	Vp (km/s)	Vp/Vs
-2.5	4.82±0.29	1.73±0.07
4.0	5.23±0.12	1.88±0.07
10.0	5.23±0.14	1.38±0.11
15.0	6.49±0.29	1.65±0.08
20.0	6.52±0.44	1.51±0.11
25.0	8.18±0.65	1.89±0.31
33.0	8.21±0.23	1.90±0.22
47.0	8.21±0.16	1.80±0.16
65.0	8.30±0.08	1.78±0.13

*Depths referred to sea level, negative depths are elevations above sea level.

Table 6.3. Station corrections

Station	P-Correction (s)	S-Correction (s)
VNFG	0.44±0.10	1.10±0.15
VNHG	-0.19±0.10	0.03±0.17
VNKR	-0.61±0.10	-0.74±0.20
VNNF	0.25±0.06	0.69±0.17
VNSG	-0.64±0.12	-0.85±0.21
VNSS	0.00±0.00	0.00±0.00
VNSW	0.09±0.10	0.17±0.21
VNWF	0.11±0.05	0.45±0.16

Table 6.4. Parameters for computed fault-plane solutions

Date	strike	Dip	Rake	FM	STDR
2001014 1314	90	65	30	7	0.75
2001016 0 10	60	70	160	6	0.75
20021030 4 11	120	80	-180	6	0.75
200211 6 11 5	75	70	120	6	0.49
20021125 2010	140	85	100	6	0.44
20021127 815	145	35	90	6	0.96
20021128 1533	145	35	100	6	0.95
20021212 8 5	50	40	110	7	0.31
2003 130 948	80	70	60	7	0.76
2003 614 823	250	80	120	6	0.44
2003 7 4 1517	115	85	-40	6	0.63
2003 8 6 1533	345	75	90	6	0.35
20031213 439	125	70	150	6	0.72
20031213 1955	75	90	0	8	0.71
20031213 2055	345	10	60	8	0.58
2004 831 1929	25	65	-40	6	0.73
2004 9 9 20 5	130	70	-110	6	0.66

FM=Number of first-motion polarities.

STDR=Station Distribution Ratio.

6.11. References

Crouch, S.L., Starfield, A.M., 1983. Boundary element methods in solid mechanics. Allen Unwin, London, 322 p.

Deichmann, N., 1987. Focal depths of earthquakes in northern Switzerland. Ann. Geophys. 5B, 395-402.

Detterman, R.L., Miller, T.P., Yount, M.E., Wilson, F.H., 1981a. Geologic map of the Chignik and Sutwik Island quadrangles, Alaska. Map I-1229, USGS.

Detterman, R.L., Miller, T.P., Yount, M.E., Wilson, F.H., 1981b. Quaternary geologic map of the Chignik and Sutwik Island quadrangles, Alaska. Map I-1292, USGS.

Dixon, J.P., Stihler, S.D., Power, J.A., Tytgat, G., Moran, S.C., Sánchez, J.J., McNutt, S.R., Estes, S., Paskievitch, J., 2003. Catalog of earthquake hypocenters at Alaskan volcanoes: January 1 through December 31, 2003. 2004-1234, USGS.

Ellsworth, W.L., 1977. Three-dimensional structure of the crust and mantle beneath the island of Hawaii. Ph.D. thesis, Mass. Inst. of Technol., Cambridge.

Fogleman, K.A., Lahr, J.C., Stephens, C.D., Page, R.A., 1993. Earthquake locations determined by the southern Alaska seismograph network for October 1971 through May 1989. 93-309, USGS.

Kissling, E., 1988. Geotomography with local earthquake data. Rev. Geophys. 26, 659-698.

Kradolfer, U., 1989. Seismische tomographie in der Schweiz mittels lokaler Erdbeben. Ph.D. thesis, Eidg. Techn. Hochschule (ETH), Zürich.

Lahr, J.C., Chouet, B.A., Stephens, C.D., Power, J.A., Page, R.A., 1994. Earthquake classification, location and, error analysis in a volcanic environment: implications for the magmatic system of the 1989-1990 eruptions of Redoubt volcano, Alaska. J. Volcanol. Geotherm. Res. 62, 137-151.

Lahr, J.C., 1999. HYPOELLIPSE: A computer program for determining local earthquake hypocentral parameters, magnitude, and first-motion pattern, (Y2K compliant version). 99-23, USGS.

Lu, Z., Wyss, M., 1996. Segmentation of the Aleutian plate boundary derived from stress direction estimates based on fault plane solutions. J. Geophys. Res. 101, 803-816.

Miller, T.M., McGimsey, R.G., Richter, D.H., Riehle, J.R., Nye, C.J., Yount, M.E., Dumoulin, J.A., 1998. Catalog of the historically active volcanoes of Alaska. 98-582, USGS.

Musumeci, C., Malone, S.D., Giampiccolo, E., Gresta, E., 2000. Stress tensor computations at Mount St. Helens (1995-1998). Ann. Geofis. 43, 889-904.

Nakamura, K., Jacob, K.H., Davies, J.N., 1977. Volcanoes as possible indicators of tectonic stress orientation – Aleutians and Alaska. PAGEOPH 115, 87-112.

Nicholson, C., Simpson, D.W., 1985. Changes in Vp/Vs with depth: implications for appropriate velocity models, improved earthquake locations, and material properties of the upper crust. Bull. Seismol. Soc. Am. 75, 1105-1123.

Okada, Y., 1992. Internal deformation due to shear and tensile faults in a half-space. Bull. Seismol. Soc. Am. 82, 1018-1040.

Reasenberg, P.A., Oppenheimer, D., 1985. FPFIT, FPPLOT, and FPPAGE: FORTRAN computer programs for calculating and displaying earthquake fault-plane solutions. 85-739, USGS.

Riznichenko, Y., 1958. The mass determination of the coordinates of local earthquakes and of the velocities of seismic waves in the source areas. Izv. Geophys. Ser. 425-437.

Roecker, S.W., 1981. Seismicity and tectonics of the Pamir-Hindu Kush region in central Asia. Ph.D. thesis, Mass. Inst. of Technol. Cambridge.

Simkin, T., Siebert, L., 1994. Volcanoes of the world (2nd edition). Geoscience Press, Tucson.

Sánchez, J.J., Wyss, M., McNutt, S.R., 2004. Temporal-spatial variations of stress at Redoubt volcano, Alaska, inferred from inversion of fault plane solutions. J. Volcanol. Geotherm. Res. 130, 1-30.

Toda, S., Stein, R.S., 2002. Response of the San Andreas fault to the 1983 Coalinga-Nuñez earthquakes: an application of interaction-based probabilities for Parkfield. J. Geophys. Res.107, 10.1029/2001JB000172.

Toth, T., Kisslinger, C, 1984. Revised focal depths and velocity model for focal earthquakes in the Adak seismic zone. Bull. Sesimol. Soc. Am. 74, 1349-1360.

Wadati, K., Sagisaka, K., Masuda, K., 1933. On the travel time of earthquake waves (part II). Geophys. Mag. 7, 101-111.

Wyss, M., Lu, Z., 1995. Plate boundary segmentation by stress directions: Southern San Andreas fault, California. Geophys. Res. Lett. 22, 547-550.

Chapter 7. Temporal Variations in the Complex Frequencies of Long-Period Seismic Events at Mt. Veniaminof, Alaska[1]

7.1. Abstract

The temporal evolution of the complex frequencies of 50 long-period seismic events at Mt. Veniaminof, Alaska, recorded during 2002-2004, have been analyzed using the Sompi method. We observed short-term temporal variations in complex frequencies during 2002-2004 as well as an overall increase in frequency in 2004. Data during 2002-2004 shows five ramp-like cycles of simultaneous increase in frequency and decrease in Q and one period of simultaneous decrease in frequency and increase in Q during July 2004. The average values of frequency=1.44 Hz and Q=29 during the earlier 2002-2003 period are smaller than their values of frequency=1.93 Hz and Q=35 during 2004. During the later 2004 period there is a progressive increase in the frequency of the dominant spectral peaks from 1.38 Hz to 1.92 Hz. We suggest that the short-term changes in complex frequencies during 2002-2004 may be associated with repetitive heating-drying of cavities beneath the vent caused by pulses of hot gas released from magma at depth. The overall change in complex frequencies between 2002-2003 and 2004 correlates with the observed change in surface activity, from mostly release of steam during the earlier period to mostly ash eruptions in 2004. We suggest that the temporal variations in complex frequencies can be used to track variations in volcanic activity with time and thus be used as an effective monitoring tool.

[1] Sánchez, J.J., McNutt, S.R., Kumagai, H., Gil-Cruz, F., Londoño, J.M. The Complex Frequencies of Long-Period Seismic Events at Mt. Veniaminof, Alaska. Manuscript submitted to *Journal of Volcanology and Geothermal Research*.

7.2. Introduction

Long-period (LP) events are frequently associated with volcanic unrest and eruptions. The waveforms of LP events often have emergent P-wave arrivals and unclear S-waves that are followed by a superposition of simple decaying sinusoids. The spectral frequencies of LP events are usually in the band 0.5 - 5 Hz. The source of LP events has been extensively studied and most models suggest that LP events are the signals resulting from oscillations of a resonating fluid-filled cavity in relation to magmatic or hydrothermal activity (e.g., Chouet, 1996).

A variety of models for the generation of LP events have been suggested, including excitation of magma-filled cracks by tip extension (Aki et al., 1977; Chouet, 1988), oscillations excited by bubble collapse (Chouet, 1992), resonance of a steam-filled crack by choked flow (Chouet et al., 1994; Morrisey and Chouet, 1997), resonance of a magma pipe or a spherical magma reservoir (Chouet, 1985; Crosson and Bame, 1985), and, oscillations of a bottle-shaped gas-filled cavity (Seidl and Hellweg, 2003).

The source properties of LP events can be determined from the complex frequencies of decaying oscillations in the tail of the seismogram. To this end, a recently developed method of high-resolution spectral analysis for harmonic signals named Sompi (Hori et al., 1989; Kumazawa et al., 1990) can be used to quantify the frequency (f) and Q (a measure of attenuation) at the source of LP events. The method is based on a homogeneous autoregressive (AR) difference equation to compute the frequencies and decay characteristics of signals in the complex frequency domain. Initially the Sompi method was successfully applied to study such diverse phenomena as the free oscillations in the Earth (Hori et al., 1989) and nuclear magnetic resonances (Matsuura et al.,

1990). More recently, however, Sompi has been applied to the study of LP events at volcanoes around the world (Nakano et al., 1998; Kumagai and Chouet, 1999; Kumagai et al., 2002; Molina et al., 2004).

Mt. Veniaminof (MV) is a stratovolcano in the Alaska Peninsula (56.2°N, 159.4° W, elevation: 2507 m), 35 km wide at the base and truncated by a summit caldera ~8 km in diameter (Figure 7.1). An intracaldera cone with a summit height of 2156 m has been the source of all recent eruptions (Miller et al., 1998; Simkin and Siebert, 1994; Global Volcanism Network, 2005).

In this paper we describe the waveform characteristics and temporal evolution in the complex frequencies of LP events at MV. LP events are characteristic of enhanced periods of activity during 2002-2004. During late 2002-early 2003 an intense swarm of LP events was recorded, but confirmation of eruptive activity was elusive. The seismicity rates during this early period peaked at several thousands of LP events per day and the similarities in waveforms are indicative of a common, non-destructive source. Seismic unrest resumed in 2004 and this time, vigorous steaming and frequent mild eruptive activity in the form of ash bursts were confirmed by ground and pilot reports, satellite imagery, and still photos from an internet camera installed in the town of Perryville. We incorporate our observations into a conceptual model for the magmatic-hydrothermal system of MV.

7.3. Data

The seismograph network on MV is composed of 8 stations equipped with Mark Products L4-C vertical component short-period (T=1 sec) seismometers (Figure 7.1b.) Data are telemetered in analog form to Port Heiden and retransmitted via phone lines to Anchorage and Fairbanks and digitized at 100

samples/s. Archiving and processing of data from these stations began in February 2002 and since then, a variety of signals have been recorded, including LP events and volcano-tectonic (VT) earthquakes. VT earthquakes are high-frequency signals associated with brittle failure or slip on pre-existing faults in response to stress from magmatic activity. These signals form the background seismicity at MV (Chapter 6) and are not the focus of this chapter.

We selected 50 LP digital waveforms recorded at the closest station (VNSS, distance ~ 5.4 km NW of the vent), which provided continuous data during 2002-2004. Data from station VNSS have the best signal-to-noise ratio among any MV stations. LP events were selected more or less regularly spaced in time (approximately 1 event/week) to allow detection of any short-term changes in complex frequencies occurring during the long-lasting swarms.

Data from more distant stations in the network were not used. The emergent arrivals and sometimes low signal-to-noise ratio make it difficult to locate the source of the LP events. From the characteristics of arrivals and amplitudes observed a various stations, and also from confirmation of surface activity, we assume that the source of LP events at MV is located at shallow depth beneath the active vent. Table 7.1 lists the relevant parameters for the signals used, and Figure 7.2 shows examples of various LP waveforms.

7.4. Method

To motivate the use of the Sompi method, we first give an example of a LP spectrum computed using the more familiar Fast Fourier Transform (FFT) algorithm of Cooley and Tukey (1965). Figure 7.3 shows the amplitude spectrum and spectrogram for one of the LP events shown in Figure 7.2. The spectral amplitude represented by the peak height in Figure 7.3a is difficult to

interpret, because the instantaneous spectral amplitude depends on time (Figure 3b). The power density within a particular time segment of the LP event could be defined for each of the spectral peaks, but the peaks cannot always be well resolved by this usual spectral representation on a real frequency axis.

In the Sompi method the time series under consideration is deconvolved into a linear combination of coherent sinusoids with amplitudes exponentially decaying (or growing) with time (Hori et al., 1989; Kumazawa et al., 1990). In this manner the coherent signals present in the time series are represented by "wave elements". Each element is represented by complex and real parameters. Let z be a complex parameter that represents a given wave element:

$$z=\exp(\gamma + i\omega) \qquad (1)$$

where γ and ω are the imaginary and real parts of the complex angular frequency. Because the amplitude of a wave element can either decay or grow exponentially with time, γ can be negative or positive. The real frequency is defined by

$$f=\omega/2\pi \qquad (2)$$

and g, where

$$g = \gamma/2\pi \qquad (3)$$

is a quantity called growth rate (Hori et al., 1989). A dissipation factor Q can then be defined as

$$Q^{-1} = -2g/f \qquad (4)$$

and represents the loss of elastic energy in each oscillation cycle at a frequency *f*. Smaller *Q* means stronger attenuation (Kumagai and Chouet, 1999).

To compute the complex frequencies (*f* and *Q*) in the waveform data we only use Sompi on the tail of the seismogram. A higher resolution in frequency is achieved by applying a narrow bandpass filtering alias-folding technique (Hori et al., 1989; Kumazawa et al., 1990). Because Sompi relies on autoregressive (AR) modeling, a number of AR orders are tested during the procedure. The Akaike information criterion (AIC) is used to determine the number of wave elements and the optimum AR order.

7.5. Results

The visual representation of a set of complex frequencies is usually done by plotting the wave elements on a 2D plane with *f* and *g* axes. This is usually known as an *f-g* diagram. The results of Sompi analysis for the waveforms in Figure 7.2 are shown in Figure 7.4, along with the amplitude spectra calculated with FFT. We find variability in *f* and *Q* for LP events. In particular, events in the earlier period (2002-2003) show values of *f* between 1.12 and 1.33 and *Q* values between 17 and 33; and LP events during 2004 have *f* values between 1.4 and 2.0 and *Q* values between 40 and 48. From the amplitude spectra and *f-g* diagrams we see that several modes of oscillation are present as peaks and clusters of wave elements, respectively, but we only use the wave elements of the largest peaks to track the values of complex frequencies of LP seismicity through time.

Our dataset of LP events covers the period September 2002 – August 2004. The results of Sompi analysis for all events are shown in Figure 7.5. The

average values of *f* and *Q* during 2002-2003 are *f*=1.44 Hz and *Q*=29, and are lower than the average values of *f*=1.93 Hz and *Q*=35 during 2004. The difference in average *f* from one period to the other is statistically significant, but the same is not true for the average *Q* values. Thus we suggest that overall, the average *f* increased and the *Q* values were relatively stable from one period to the other.

A closer look to the plot in Figure 7.5, however, reveals that short-term changes occurred. We identify six periods, all lasting for roughly a month, during which *f* and *Q* show an inverse relation. These periods of rapid change in complex frequencies are labeled "I" through "VI" in Figure 7.5. Periods I to V show simultaneous increase in *f* and decrease in *Q* with time. Period VI shows decrease in *f* and increase in *Q* with time. The time periods in between are of variable duration and they show mostly a weak positive relation (simultaneous increase or simultaneous decrease in *f* and *Q* with time). During 2004 there is a general increase with time in the values of *f* with values oscillating between 1.38 and 1.92 Hz. There is a larger scatter in both *f* and *Q* during 2004.

7.6. Discussion

We analyzed the waveforms of LP events at MV and observed variety in decay characteristics in the tail of the seismograms (Figure 7.2). Because varying decay characteristics may indicate changes in complex frequencies at the source of the LP events (Kumagai et al., 2002), we applied the Sompi method to analyze the tails of the seismograms and determine the complex frequencies (*f* and *Q*) in each waveform.

A first observation in variable characteristics of LP events is that the spectral content in the tail of the seismograms changes from mostly single-peaked

spectra in 2002-2003 to mostly multiple-peaked spectra in 2004 (Figure 7.4). One of the smaller spectral peaks in 2004 has the same frequency as the strongest single peak in 2002-2003. This means that the largest peak among spectra is not always the same mode. We prefer to use the largest peak, however, because no modeling has been done for the geometry of resonator, or resonators, at the source of LP events at MV.

We also found that, overall, *f* increased and *Q* was stable. Detailed inspection of the plots of *f* and *Q* versus time revealed that six periods of rapid changes in complex frequencies occurred during 2002 – 2004 (Figure 7.5). Most of the rapid changes correspond to simultaneous increase in *f* and decrease in *Q*, with complicated periods in between. Similar polarity of changes in complex frequencies were observed for LP events at Kusatsu-Shirane volcano (Kumagai et al., 2002) although the duration of the changes and absolute values in *f* and *Q* differ from those documented here. The trends in *f* and *Q* at Kusatsu-Shirane have been modeled using geometry of a crack for the resonator (Chouet 1986; 1988; 1992) with a composition for the fluids inside containing some mixture of liquid and gas. The liquid is thought to be water and the gas could be a mixture of H_2O gas (steam), and CO_2 gas. Such a combination of composition and phases is called a *misty gas*. The increase in *f* and decrease in *Q* have been associated to a drying process occurring at the source of LP events. In general, the source starts off fairly wet (lots of water, little % of gas) and gradually dries until it is completely dry (no water, 100% gas). A simple interpretation for this is the heating of the hydrothermal system in response to thermal input from below (Kumagai et al., 2002).

The period of rapid change in f and Q toward the end of our data set (July 2004) shows simultaneous decrease in *f* and increase in *Q*, over a period of roughly one month. This same behavior in complex frequencies of LP events,

over a shorter time scale of one week, was observed at Tungurahua volcano in 2001 and the changes were attributed to injections of ash-laden gas into a crack in the conduit as a preparatory phase preceding eruptions (Molina et al., 2004). This process could be happening at MV as well. Our data sampling of one event per week, however, is not suitable to resolve these changes in a scale of days.

The computed values of Q~30 at MV could also be explained by other types of fluids such as gas-gas mixture, ash-gas mixture, and basalt-gas mixture (e.g., Kumagai and Chouet, 2000). Thus the interpretation for the observed values of Q is manifold based on the results of the crack model. At MV, however, we infer a water-gas mixture as a possible fluid at the source of LP events because of the proxy information from observations of surface activity (Table 7.2).

The LP events at MV have not been located, nor have the modelings of the geometry of the resonator and likely composition of the fluids inside been performed. Observational evidence, however, indicates that during 2002 - 2003 the volcano showed variable behavior, in the form of surface activity characterized mostly by a prolific white plume (steam), with occasional reports of dark plumes and darkened snow, indicative of mild ash puffing (Figure 7.5 and Table 7.2). These reports, together with our observations of rapid changes in f and Q, could indicate repetitive heating-drying taking place at the source of the LP events.

Overall, the surface activity at MV during 2002 - 2003 was mostly characterized by a prolific steam plume and confirmation of frequent ash bursting was elusive. During 2004, thermal anomalies were detected in satellite imagery and frequent ash puffing through the active vent was confirmed by

ground and pilot reports, satellite imagery, and near-real-time images from an internet camera installed in Perryville after April 2004 (Figure 7.5). Most of the LP events during 2004 could be associated with small ash eruptions that typically rose up to 1 km above the active cone (~ 3 km above sea level) (Figure 7.6). Our observations of complex frequencies of LP events during 2004 indicate that the average f=1.93 Hz is higher than f during 2002-2003, and that both f and Q show larger scatter in their values. Also f shows a tendency to increase between February and August 2004. Ash bursts and strombolian activity continued until the time of this writing (February 2005).

We infer that a progressive heating in the hydrothermal system beneath MV may have occurred from 2002 to 2004. We speculate that the source of heat could be hot gases from magma intruding through a dike or system of dikes (Chapter 6). This progressive heating would produce a drying in the cavities containing a mixture of water and gas at shallow depth beneath the vent. The ash may be the result of fragmentation of the magma. Further, it is likely that during 2002-2004 the heating-drying of cavities occurred in pulses, because of the ramp-like behavior in the f and Q values (Figure 7.5).

Based on the analysis of VT earthquakes (Chapter 6), together with the observations of temporal evolution in complex frequencies of LP events and the observations of surface activity, we envision the magmatic-hydrothermal system of MV to be composed of a dike or system of dikes whose pressure variations cause stress on pre-existing faults producing the background VT activity. The magma in this system of dikes releases hot gases that interact with the shallow cavities in the hydrothermal system beneath the vent, generating the rich swarms of LP events (Figure 7.7). The heat from below may have occurred in pulses during 2002 - 2004 and also increased by 2004 producing the drying of the water inside the oscillating cavities. We note that at the time of this writing

(February 2005) an increase in heat at the surface of MV is evident from stronger strombolian eruptions that are detected by satellite imagery and seen as incandescence from Perryville.

7.7. Conclusions

We used the Sompi method to analyze the complex frequencies of LP events at MV. During 2003-2004 various ramp-like changes in *f* and *Q* occurred in the time scale of several weeks. These changes may be associated with pulses of hot gas released at depth that interacted with the shallow hydrothermal system, generating the LP events and initiating a drying of the water-and-steam-filled cavities. During 2004, the higher average value of *f*, and the general tendency of *f* to increase with time, indicates that the heating resumed in a mostly steady manner, producing further drying inside the cavities that oscillate and produce the LP seismicity. We conclude that the complex frequencies of LP events are useful in tracking temporal changes beneath the volcano and help in the monitoring and assessment of surface activity.

7.8. Acknowledgements

We thank J. Paskievitch, T. Plucinsky, and G. Tytgat for their work in the installation and maintenance of the seismograph network on MV. K. Wallace, J. Caplan-Auerbach, S, Moran, T. Petersen, M. Hellweg, B. Chouet, I. Molina, M. Nakano, S. DeAngelis, and M. West provided valuable suggestions and discussions. Special thanks to the town of Perryville, Alaska, for the multiple eyewitness reports. C. Neal helped in the compilation and interpretation of the visual observations of surface activity at Veniaminof. This work was supported by the Alaska Volcano Observatory and the U.S. Geological Survey (USGS), as

part of their Volcano Hazards Program, and by additional funds by the State of Alaska.

7.9. Figures

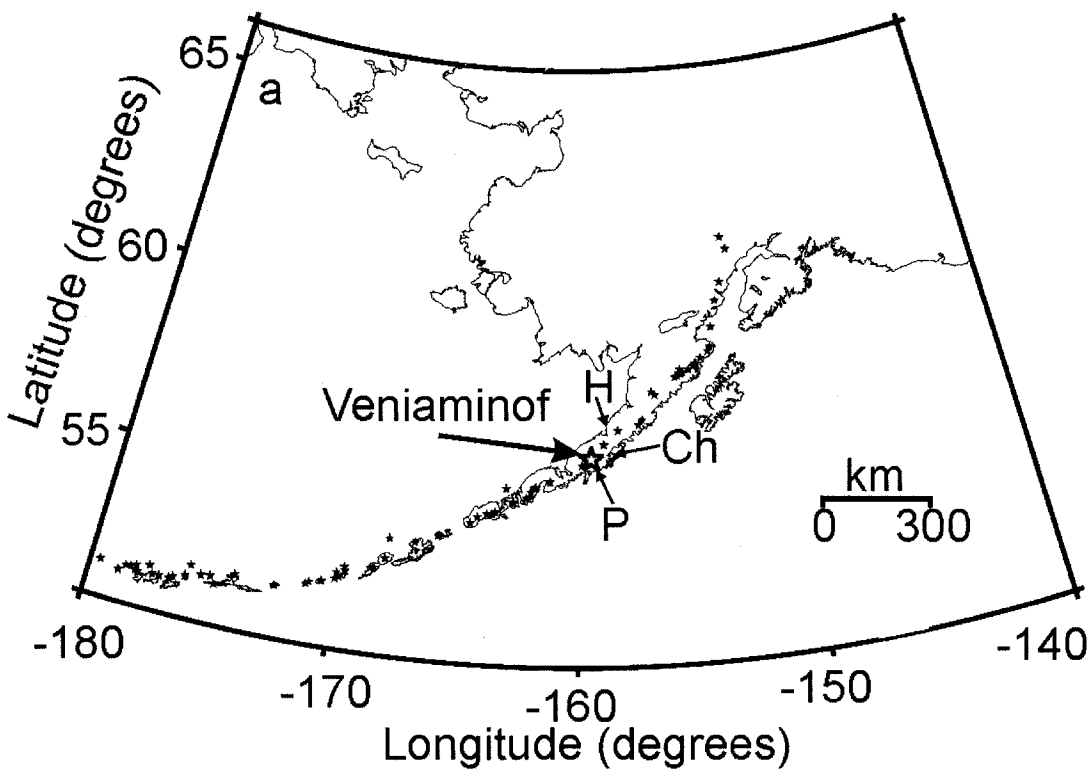

Figure 7.1a. Location map of MV. Map of Alaska showing the location of MV (large star), and other volcanoes (small black stars). Locations of three towns referred to in the text are indicated as follows: P (Perryville), Ch (Chignik), and H (Port Heiden).

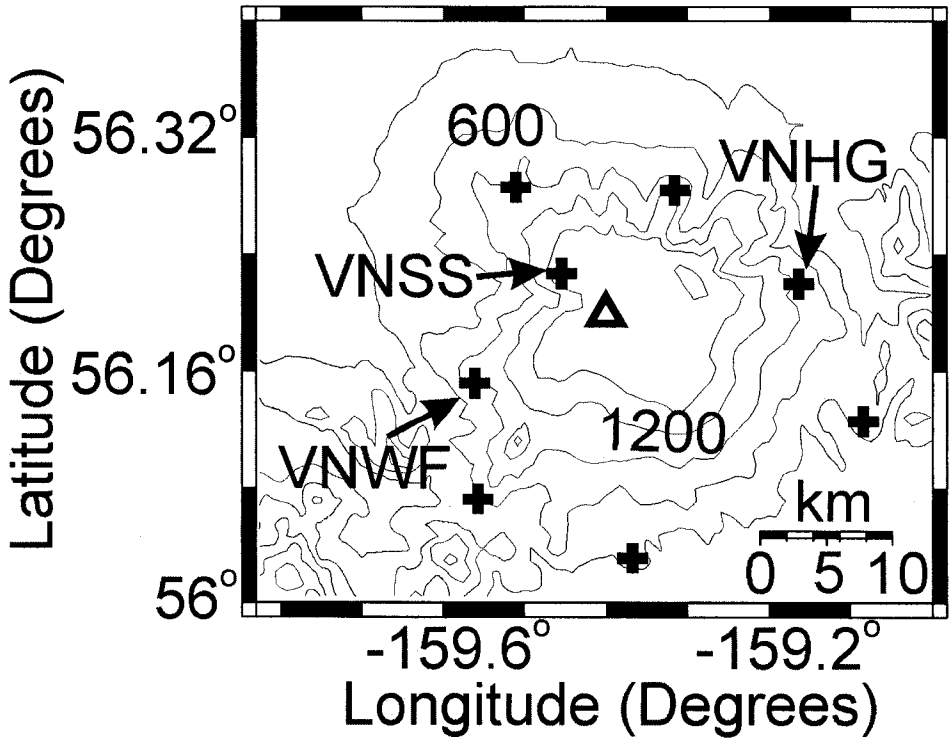

Figure 7.1b. Map of stations at MV. (b) Local map of Mt. Veniaminof with topographic contours every 300 m. Crosses mark the locations of seismograph stations (only stations mentioned in the text are labeled). The Triangle marks the active vent.

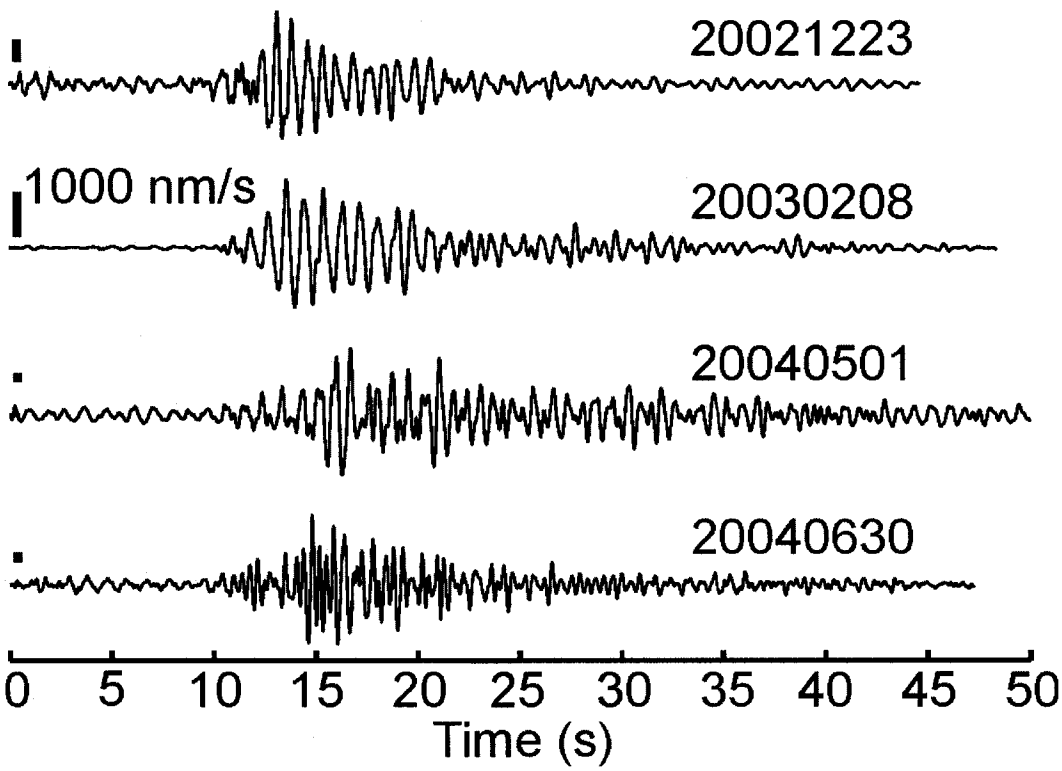

Figure 7.2. Waveforms of LP events at MV. Examples of four waveforms of LP events at MV recorded at station VNSS. The amplitude units are nm/s and are referenced to the largest amplitude. The date (YYYYMMDD) of each event is indicated above the waveforms.

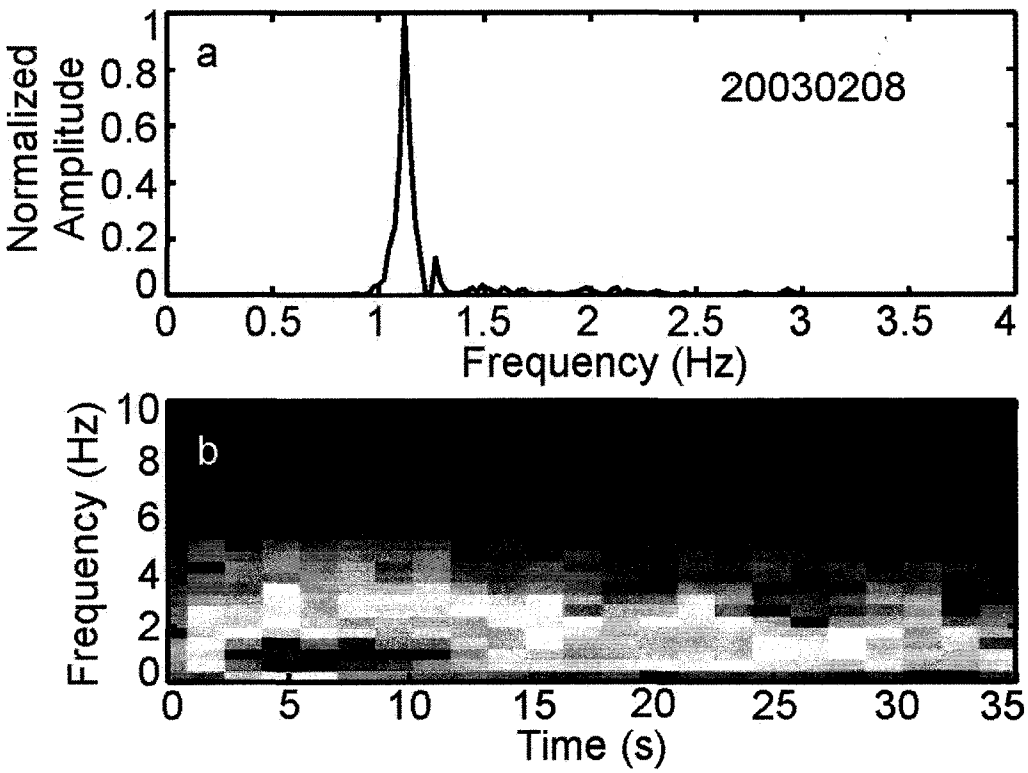

Figure 7.3. Spectra computed with FFT. (a) Amplitude spectrum for one of the LP events shown in Figure 7.2. (b) Spectrogram for the same event. Hotter colors indicate stronger signal. Other conventions as in Figure 7.2.

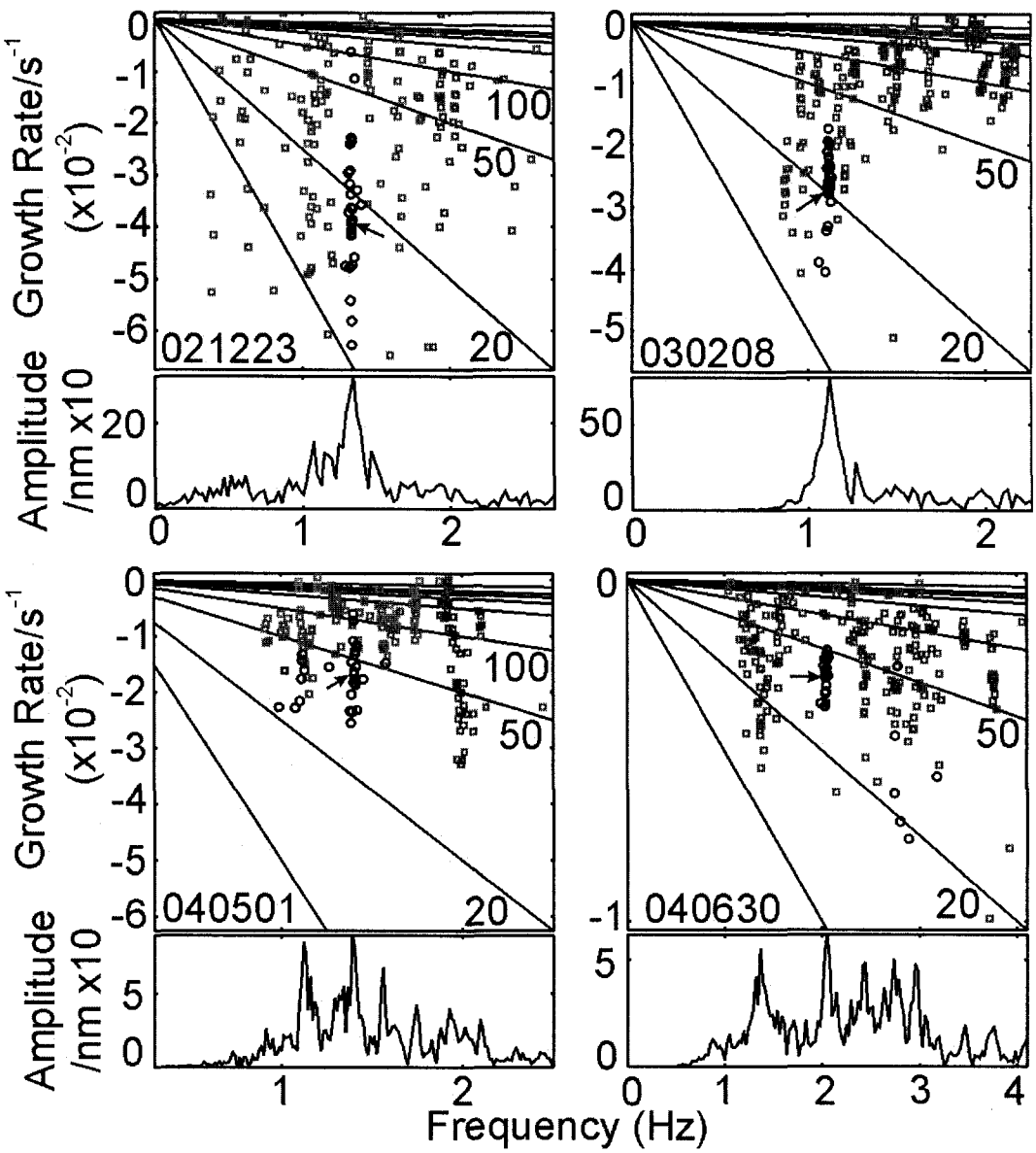

Figure 7.4. Results of Sompi analysis. Top panels: Plots of complex frequencies of individual wave elements for all the trial AR orders (4 - 60) computed for the waveforms in Figure 7.2. Black circles represent wave elements in dominant modes of oscillation, gray squares represent minor modes. Clusters of wave elements represent clear signal, and scattered elements come from incoherent noise. Solid lines represent lines of constant *Q*, (only a few lines labeled for clarity). Clusters of wave elements marked with arrows were used to quantify the temporal changes in *f* and *Q*. Dates (YYMMDD) are indicated near the lower left of each *f-g* plot. Bottom panels: FFT amplitude spectra.

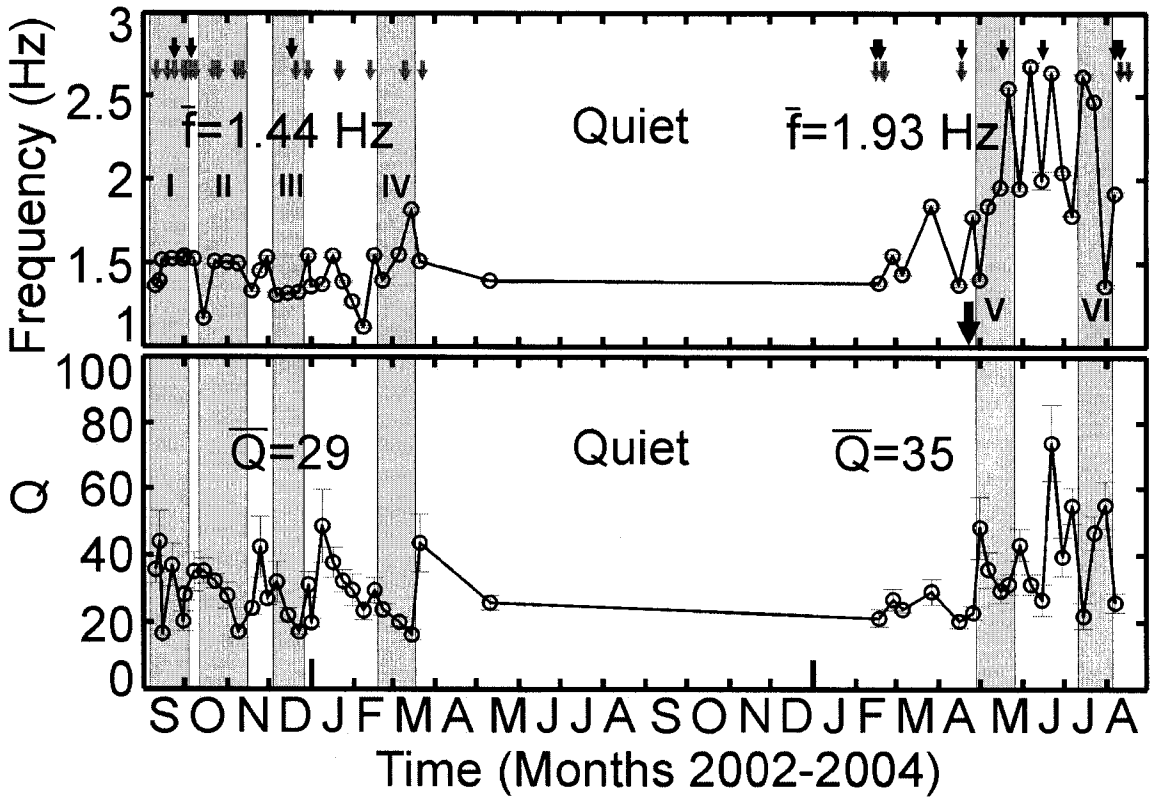

Figure 7.5. Temporal changes in complex frequencies. Plots of *f* (top) and *Q* (bottom) versus time, showing the results of Sompi analysis on all 50 LP events. During 2002-2004 the six ramp-like periods of rapid change in complex frequencies are enclosed in gray areas and labeled "I" through "VI". The average *f* and *Q* values (values with an overline) during 2002 – 2003 and during 2004 are indicated. Gray and black arrows mark the dates when eyewitnesses' reports or photographic images were consistent with white steaming or ash puffing, respectively, through the active vent. The large arrow marks the date April 23, 2004 when a real-time internet camera was installed in Perryville, allowing confirmation of frequent ash puffing associated with LP events. During the intermittent period in mid 2003 - early 2004 (labeled "Quiet") no significant LP activity was recorded.

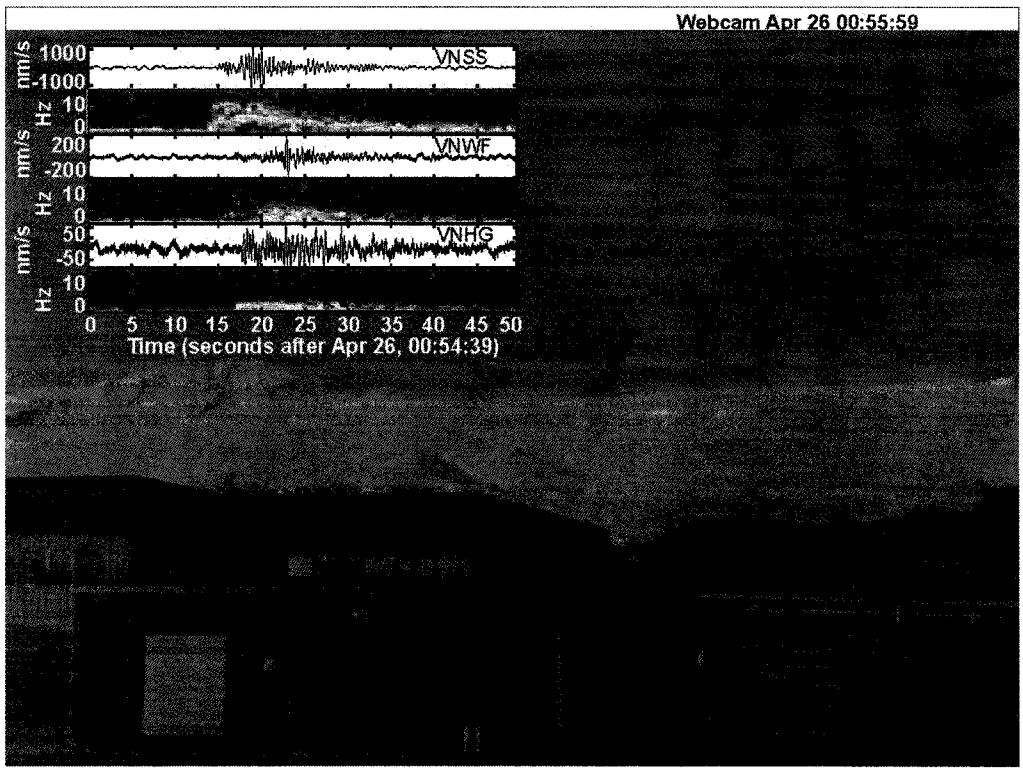

Figure 7.6. Ash burst and LP event. . Photograph taken on April 26, 2004 by the internet camera located in Perryville, showing an ash burst rising ~ 900 m above the vent. The inset shows the waveforms and spectrograms of the associated LP event recorded at three seismograph stations. Times are in Universal Time (UT). Conventions as in Figures 7.2 and 7.3.

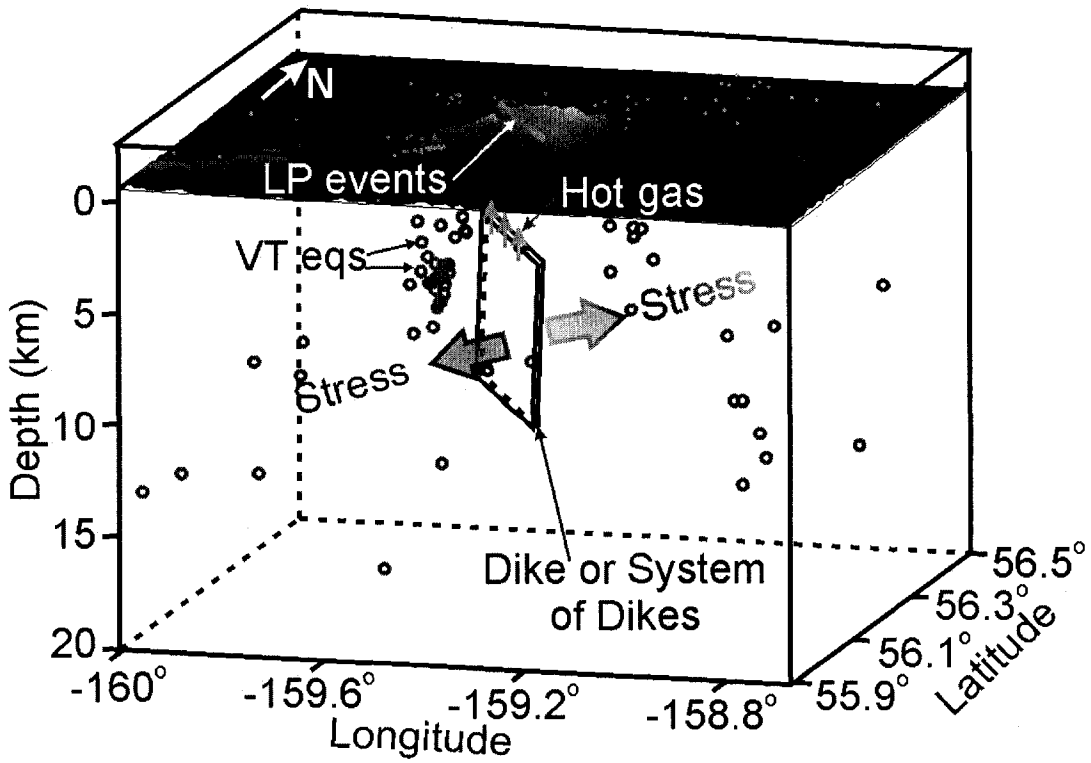

Figure 7.7. Conceptual model for seismicity at MV. Schematic view of a dike whose opening imposes stress in the adjacent regions and causes faults to move, resulting in VT seismicity (circles=hypocenters, dots=epicenters). Large gray arrows indicate the direction of dike opening. The hot gases (vertical gray arrows) released from the magma interact with the shallow hydrothermal system beneath the vent and generate the LP seismicity (Modified from Chapter 6).

7.10. Tables

Table 7.1. Parameters of LP events analyzed

Date	Time	f	σ_f	Q	σ_Q	G	σ_G
20020910	23:38	1.36	0.02	35.57	3.95	-0.019	0.002
20020913	0:25	1.39	0.00	43.97	9.09	-0.017	0.004
20020915	8:15	1.52	0.02	16.61	0.64	-0.046	0.002
20020922	22:31	1.52	0.01	36.90	6.37	-0.021	0.004
20020930	0:23	1.52	0.02	20.25	3.01	-0.038	0.006
20021001	12:35	1.54	0.01	28.23	1.77	-0.027	0.002
20021008	5:48	1.52	0.02	35.01	5.86	-0.022	0.004
20021015	9:43	1.17	0.00	35.19	3.83	-0.017	0.002
20021023	8:57	1.51	0.01	32.11	2.10	-0.024	0.002
20021101	4:35	1.50	0.02	27.84	3.92	-0.028	0.004
20021109	13:22	1.50	0.01	17.11	1.88	-0.044	0.005
20021119	6:55	1.34	0.01	24.15	1.95	-0.028	0.002
20021125	0:47	1.45	0.01	42.31	9.13	-0.018	0.004
20021130	18:17	1.53	0.01	27.02	1.99	-0.029	0.002
20021207	2:02	1.31	0.02	31.94	6.01	-0.021	0.004
20021215	0:24	1.32	0.01	22.03	2.08	-0.030	0.003
20021223	21:35	1.33	0.01	17.16	0.82	-0.039	0.002
20021230	18:38	1.54	0.01	31.09	3.94	-0.025	0.003
20030101	8:06	1.36	0.01	19.81	1.38	-0.034	0.002
20030109	3:39	1.37	0.01	48.58	10.96	-0.015	0.003
20030117	0:03	1.54	0.02	37.69	4.40	-0.021	0.002
20030124	2:13	1.39	0.00	32.20	3.27	-0.022	0.002
20030131	11:43	1.27	0.02	29.54	4.66	-0.022	0.003
20030208	0:25	1.12	0.01	23.46	2.68	-0.024	0.003
20030216	14:50	1.55	0.01	29.48	3.80	-0.027	0.004
20030222	17:13	1.40	0.01	23.76	1.69	-0.030	0.002
20030306	0:08	1.55	0.00	20.07	1.39	-0.039	0.003
20030315	3:39	1.82	0.01	16.27	1.42	-0.056	0.004
20030321	6:31	1.51	0.01	43.57	8.64	-0.018	0.003
20030511	10:18	1.40	0.01	25.84	2.18	-0.027	0.002
20040218	6:39	1.38	0.01	21.25	2.64	-0.033	0.004
20040228	15:02	1.55	0.01	26.76	3.18	-0.029	0.004
20040306	12:08	1.44	0.01	23.86	0.86	-0.030	0.001
20040327	6:56	1.84	0.01	29.14	3.82	-0.032	0.004
20040416	0:06	1.37	0.01	20.30	2.02	-0.034	0.003
20040426	7:52	1.78	0.02	22.89	2.03	-0.039	0.003
20040501	3:34	1.41	0.01	48.24	9.32	-0.015	0.003
20040507	16:38	1.84	0.01	35.74	5.34	-0.026	0.004
20040516	19:41	1.95	0.01	29.43	3.55	-0.034	0.004
20040522	2:42	2.55	0.01	31.35	3.11	-0.041	0.004
20040530	6:41	1.95	0.01	43.03	4.75	-0.023	0.003
20040607	5:44	2.68	0.02	31.33	3.10	-0.043	0.004
20040615	8:05	2.00	0.05	26.72	4.69	-0.038	0.007
20040622	0:27	2.64	0.01	73.96	11.64	-0.018	0.003
20040630	4:07	2.05	0.01	39.59	5.73	-0.026	0.004
20040707	12:54	1.79	0.00	54.81	5.48	-0.016	0.002
20040715	16:34	2.62	0.02	21.89	3.87	-0.061	0.010
20040723	23:12	2.47	0.02	46.73	5.03	-0.027	0.003
20040731	0:36	1.37	0.01	55.02	7.17	-0.013	0.002
20040807	2:22	1.92	0.01	25.86	2.90	-0.038	0.004

f=frequency.

G=growth rate.

σ=standard deviation.

Table 7.2. Reports of surface activity at MV

Date	Report	Reference
9/11/2002	No "smoke"	A. Karmakof, A. Strack, B. Wise, D. Hermelling.
9/19/2002	No "smoke"	A. Strack.
9/24/2002	Intermittent "*white and black*" puffing; "vigorous *solid white*" puffing; "shooting *black* smoke"	Perryville Native Council and Village Council.
10/1/2002	Confirmed reports of "plume of smoke"; one audible rumbling.	A. Strack.
10/2/2002	"Smoke" stopped.	A. Strack
10/2/2002	No obvious signs of activity, but possible ash deposit on snow.	PIREP, Arctic Circle Air; R. Kmlecik (PIREP*).
10/6/2002	Black ash and "smoke", explosions heard, ground shaking.	Sandy River Lodge.
10/9/2002	No visible activity of any kind.	R. Kmieclk (PIREP).
10/15/2002	Possible ash deposit on glacier.	A. Strack.
10/22/2002	No "smoke" or venting, but possible ash deposit on glacier (east flank).	A. Strack.
10/26/2002	Intermittent *white* "smoking"	A. Strack.
11/8/2002	No activity	A. Strack.
11/12/2002	Nothing unusual	C. Neal-report from Perryville.
12/18/2002	Black "smoke" from cone.	C. Odomin, USFWS.
12/21/2002	Intracaldera cone covered with ash, darkened snow; intermittent "smoking."	C. Odomin, USFWS.
12/30/2002	"About same amount of steam as usual."	C. Odomin
1/21/2003	No "smoke."	Perryville school.
1/22/2003	Only *white* "smoke."	A. Strack, M. Battaion (photo).
2/13/2003	"Not that much steam."	M. Battaion (photo).
3/12/2003	"No steaming or activity over the past few days."	Perryville school.
3/23/2003	White steam.	M. Battaion (photo by M. Kosbruk).

PIREP=Pilot's report.

7.11. References

Aki, K., Fehler, M., Das, S., 1977. Source mechanism of volcanic tremor: Fluid-driven crack models and their application to the 1963 Kilauea eruption. J. Volcanol. Geotherm. Res. 2, 259-287.

Chouet, B.A. 1985. Excitation of a buried magmatic pipe: A seismic source model for volcanic tremor, J. Geophys. Res. 90, 1881-1893.

Chouet, B.A., 1988. Resonance of a fluid-driven crack: Radiation properties and implications for the source of long-period events and harmonic tremor. J. Geophys. Res. 93, 4375-4400.

Chouet, B.A., 1992. A seismic model for the source of long-period events and harmonic tremor. In: Gasparini et al., (eds), Volcanic Seismology, IAVCEI Proceedings in Volcanology. Vol. 3, pp. 133-156. Springer-Verlag, New York.

Chouet, B.A., Page, R.A., Stephens, C.D., Lahr, Power, J.A., 1994. Precursory swarms of long-period events at Redoubt Volcano, Alaska: Their origin and use as a forecasting tool. J. Volcanol. Geotherm. Res. 62, 95-135.

Chouet, B.A., 1996. Long-period volcano seismicity: Its source and use in eruption forecasting. Nature, 380, 309-316.

Cooley, J.W., Tukey, J.W., 1965. An algorithm for the machine calculation of complex Fourier series. Math. Comput. 19, 297-301.

Crosson, R.S., Bame, D.A., 1985. A spherical source model for low-frequency volcanic earthquakes. J. Geophys. Res. 90, 10237-10247.

Global Volcanism Network., 2005. Volcanic activity reports Bulletin of the Global Volcanism Network, Smithsonian Institution, BGVN. 27-29.

Hori, S., Fukao, Y., Kumazawa, M., Furumoto, M., Yamamoto, A., 1989. A new method of spectral analysis and its applications to the Earth's free oscillations: The "Sompi" method. J. Geophys. Res. 94, 7535-7553.

Kumazawa, M., Imanishi, Y., Fukao, Y., Furumoto, M., Yamamoto, A., 1990. A theory of spectral analysis based on the characteristic property of a linear dynamic system. Geophys. J. Int. 101, 613-630.

Kumagai, H., Chouet, B.A., 1999. The complex frequencies of long-period seismic events as probes of fluid composition beneath volcanoes. Geophys. J. Int. 138, F7-F12.

Kumagai, H., Chouet, B. A., 2000. Acoustic properties of a crack containing magmatic or hydrothermal fluids. J. Geophys. Res. 105, 25,493-25,512.

Kumagai, H., Chouet, B.A., Nakano, M., 2002. Temporal evolution of a hydrothermal system in Kusatsu-Shirane Volcano, Japan, inferred from the complex frequencies of long-period events. J. Geophys. Res. 107, doi: 10.1029/2001JB000653.

Matsuura, T., Imanishi, Y., Imanari, M., Kumazawa, M., 1990. Application of a new method of high-resolution spectral analysis, "Sompi," for free induction decay of nuclear magnetic resonance. Appl. Spectrosc. 4, 618-626.

Miller, T.M., McGimsey, R.G., Richter, D.H., Riehle, J.R., Nye, C.J., Yount, M.E., Dumoulin, J.A., 1998. Catalog of the historically active volcanoes of Alaska. 98-582, USGS.

Molina, I., Kumagai, H., Yepes, H., 2004. Resonances of a volcanic conduit triggered by repetitive injections of an ash-laden gas. Geophys. Res. Lett. 31. doi: 10.1029/2003GL018934.

Morrisey, M.M., B.A. Chouet., 1997. A numerical investigation of choked flow dynamics and its application to the triggering mechanism of long-period events at Redoubt Volcano, Alaska. J. Geophys. Res. 102, 7965-7983.

Nakano, M., Kumagai, H., Kumazawa, M., Yamaoka, K., Chouet., B.A., 1998. The excitation and characteristic frequency of the long-period volcanic event: An approach based on an inhomogeneous autoregressive model of a linear dynamic system. J. Geophys. Res. 103, 10031-10046.

Sánchez, J. J. 2005. Volcano seismology from around the World: Case studies from Mount Pinatubo, Philippines, Galeras, Colombia, Mount Wrangell and Mount Veniaminof, Alaska, Ph.D. Thesis, University of Alaska, Fairbanks.

Seidl, D., Hellweg, M., 2003. Parameterization of multichromatic tornillo signals observed at Galeras Volcano (Colombia). J. Volcanol. Geotherm. Res. 125, 171-189.

Simkin, T., Siebert, L., 1994. Volcanoes of the world (2^{nd} edition). Geoscience Press, Tucson.

Chapter 8. Conclusions

We investigated different aspects of seismicity at volcanoes in Philippines, Colombia, and Alaska using a variety of techniques ranging from the statistical analysis of the spatial distribution of earthquake sizes to the high-resolution spectral analysis of digital waveforms. In all cases the data presented serious challenges that mainly resulted from the sparse seismograph networks used to detect the earthquakes. Because of this, many seismologists would have regarded the data as suitable for monitoring purposes only.

With the advent of new monitoring tools and precise instrumentation it is tempting to think of old data (or data currently being recorded in many regions worldwide) as non-useful for research. In a number of seismological observatories, however, it will be a long time before modern instrumentation can be obtained. Thus we raise the question: Are we stranded, or can we actually get science out of limited data?

With the papers presented in this thesis, we provide evidence that while acknowledging the limitations of the data, careful data selection and strong statistical analysis allow us to derive important conclusions on the magmatic/hydrothermal systems of volcanoes where the sparse configuration of the seismograph networks imposes challenges for research. Our results, of course, can be tested against findings from other studies, and the focus of our concluding remarks is precisely about suggestions for future research. We kindly refer the reader to the conclusions within each of the chapters for details regarding the specific studies.

8.1. Investigating the Spatiai Configuration of Magma Bodies and Conduit Systems of Voicanoes Using *b*-value Mapping

The mapping of *b*-values at Mount Pinatubo (Philippines) and Galeras volcano (Colombia) revealed two fundamentally different patterns of high *b*-value anomalies that are intuitively associated with a shallow temporary magma storage region and a deeper magma body (Pinatubo) and an elongated structure beneath the active crater that we suggest is associated with a conduit or the remains of crystallizing magma (Galeras). Recently Battagglia et al., (2004) relocated the seismicity following the June 15 eruption of Mt. Pinatubo using precise cross-correlation techniques. They concluded that the main cluster of seismicity can be attributed to an intrusive process from below the crater. An obvious suggestion for future research is to use this relocated dataset to map *b*-value anomalies and to study the spatial configuration of *b*-value anomalies in more detail. The determination of magnitudes for the newly relocated events could be challenging, however (J. Battaglia, Pers. Comm., 2004). At Galeras volcano some recent preliminary results from spatial mapping of Q (a measure of attenuation) indicate two anomalies located at 9 km and 4 km beneath the vent (Vargas et al., 2004). Thus we suggest studying the attenuation Q in more detail and further studying the internal configuration of the volcano using travel-time tomography.

8.2. Intermediate-Term Earthquake-Volcanoes Interactions

The unexpected response of Mt. Wrangell and Mt. Veniaminof volcanoes to the shaking or static stress changes from the Mw 7.9 Denali Fault Earthquake widened our view in terms of what to expect from a volcano following the passage of waves from a distant tectonic shock. One aspect that remains an open question is determining whether the static or dynamic effects can be of

more relevance in the subsequent behavior of the volcano. Also a research in the catalogs of seismicity at volcanoes around the world could reveal other cases of declines in local seismicity after large earthquakes. The Mw 7.7 Rat Islands Earthquake on November 17, 2003 occurred several hundred kilometers from the seismically active Gareloi volcano (AEIC, 2003), whose seismicity is mostly of the long-period type. Because the background seismicity at Gareloi was not well known in 2003, a response to the Rat Island events could not be firmly established.

8.3. Seismicity at Mt. Veniaminof, Alaska

Our analyses of volcano-tectonic and long-period seismicity at Mt. Veniaminof indicated that volcano-tectonic earthquakes occur preferably away from the active vent and caldera regions and that the complex frequencies of long-period events can be used to track changes in the surface activity at the volcano. We put forward the idea that the magma system of Mt. Veniaminof is composed of a dike or system of dikes whose hot gases interact with the shallow hydrothermal system. At the time of this writing (December 2004) the number of located volcano-tectonic events does not allow a study of the 3D velocity distribution. At the present rate of ~100 eqs/year we can expect to collect a fair number of phase arrivals in a few more years and use the 1D model derived in chapter 6 as a minimum model for 3D tomography. The distribution of volcano-tectonic earthquakes around Mt. Veniaminof is well suited for tomography studies. To be able to study the volcano in more detail, however, we recommend the installation of additional three-component stations. This would allow attempting the location of long-period events and modeling of their source mechanisms.

8.4. References

AEIC-Alaska Earthquake Information Center., 2004. Web page http://www.giseis.alaska.edu/html_docs/rat_islands_2003.html.

Battaglia, J., Thurber, C. H., Got, J-L., Rowe, C., White, R. A., 2004. Precise location of earthquakes following the 15 June 1991 eruption of Mount Pinatubo (Philippines). J. Geophys. Res. 109, doi:10.1029/2003JB002959.

Vargas, C. A., Duran, J. P., Moncayo, E., Montes, L. A., Castillo, L. A., Canela, A., 2004. Spatial and temporal changes of Coda Q in the Galeras volcano, Colombia. EOS Trans. AGU, 85, 47, abstract V11B-1432.

Appendix

A.1. Response of Wrangell Volcano, Alaska to the December 26, 2004 Mw 9.0 Sumatra-Andaman Islands, Indonesia, Earthquake

On December 26, 2004, an Mw 9.0 earthquake struck off of the coast of northern Sumatra, Indonesia at 00:58:53 UT time. The earthquake initiated a tsunami that caused widespread destruction across the Indian Ocean and the deaths of at least 220,272 people. The Sumatra-Andaman Islands earthquake (SAE) was the fourth largest earthquake in the world since 1900 and is the largest since the 1964 Prince William Sound, Alaska earthquake (NEIC, 2005; Chapman, 2005; Sorooshian, 2005, Park et al., 2005). Recent unpublished data suggest that the Sumatra-Andaman Islands Earthquake may be the second largest earthquake recorded ever, with a magnitude of Mw=9.3, as estimated from long-period vibrations (Stein and Okal, 2005). At 01:56:50, a short-lived flurry of local events was recorded at all seismograph stations on Mt. Wrangell, Alaska, during the passage of the surface waves from the SAE (Figure A.1).

Some of the local events had arrivals that could be used to obtain preliminary locations around the summit of Wrangell, with some scatter (Figure A.2). Some of the scatter in the locations may come from unclear arrival times. The variability in waveforms of the local events between 01:56 and 04:37, however, suggest that various seismogenic sources beneath Wrangell volcano may have responded to the dynamic strains from the SAE (Figure A.3).

The most striking feature of the triggered events at Wrangell is that they are regularly spaced in time, every ~31 s, occurring mostly in phase with either the downward or upward excursions of vertical displacement records (Figure A.4), suggesting that a local event was triggered at the volcano when the ground was

compressed. If these events were in fact triggered by the SAE, this is the farthest distance reported for cases of triggering of seismicity, because Wrangell volcano is located roughly 11,000 kilometers from the epicenter of the perturbing mainshock.

Because Wrangell volcano has a somewhat elevated level of seismicity (see chapters 4 and 5) it is not surprising to see groups of small events clustered in time. As a matter of fact, during the period December 24-27, 2004 (more precisely the 41 hours before and 43 hours following the arrival of the surface waves from the SAE) we observed 9 such clusters. What makes the proposed triggered events unique is the fact that they are regularly spaced in time. A maximum likelihood estimate of the probability of finding one cluster of five events, spaced every 31 s during the time span of 84 hours gives p=0.0028 (99% confidence intervals are 0.0000 and 0.0207). The likelihood of such regularly spaced events is very low, making the conclusion the these events were triggered the most probable conclusion. This result also raises the question of whether other changes might be triggered by dynamic stresses of the same magnitude. As the surface waves from the Sumatra-Andaman Islands Earthquake passed Alaska, the ground rose and fell a total of about 2 centimeters (M. West, Pers. Comm., 2005).

A.2. Figures

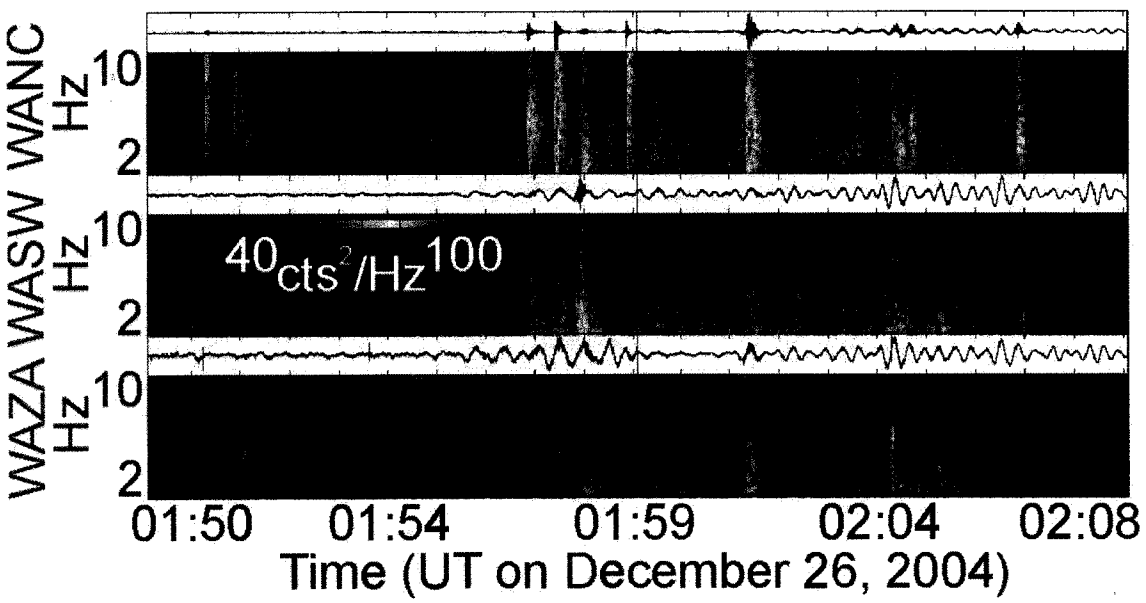

Figure A.1. Triggered local events at Wrangell. Waveforms (black traces) and spectrograms (color plots) showing the surface waves from the SAE and the small local events triggered at Wrangell volcano. Colors in the spectrogram indicate the strength of the signal. Only recordings from three stations are shown, because the vertical component of a fourth station, WACK (see Figure A.2 below), was experiencing telemetry problems.

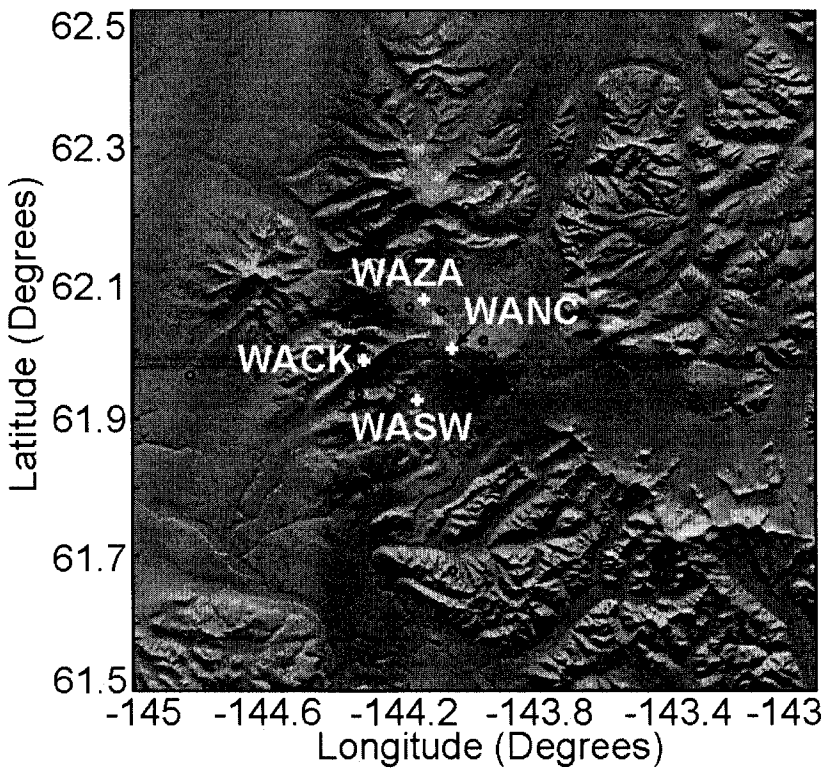

Figure A.2. Preliminary locations of triggered events at Wrangell. Shaded-relief image (courtesy of NASA/JPL) showing the topography in the Wrangell area and the preliminary epicentral locations of 16 events recorded between 01:56 and 04:37 UT on December 26, 2004. Circles mark the epicentral locations of local earthquakes and white crosses mark the locations of seismograph stations. Station WACK is equipped with a short-period three-component seismometer and only the horizontal components recorded the triggered events.

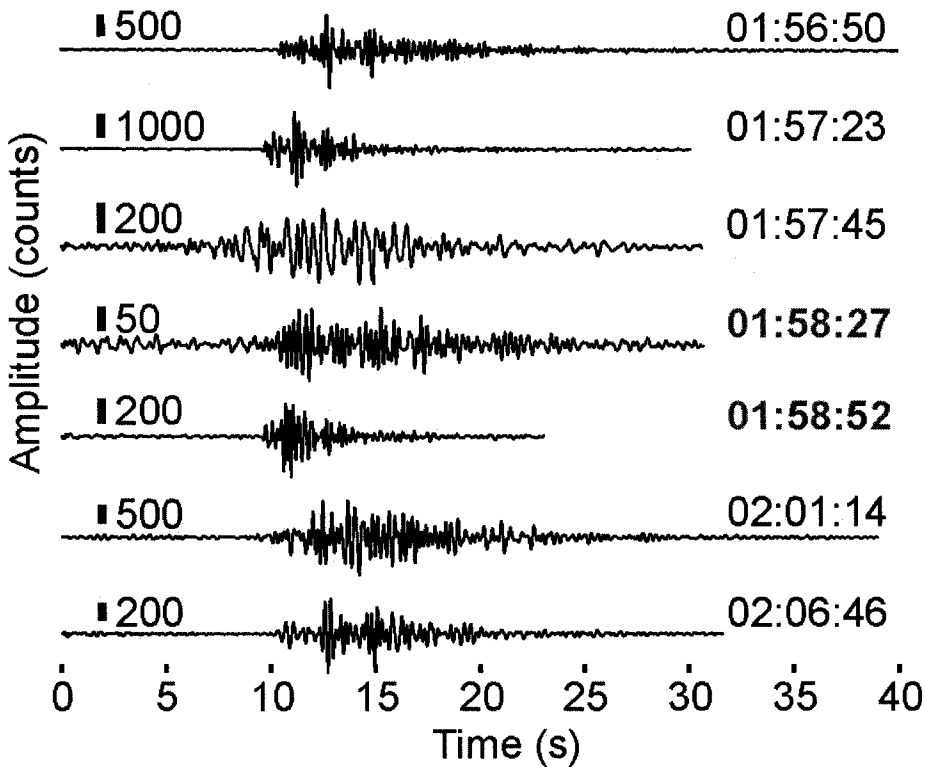

Figure A.3. Waveforms of local events. Band pass filtered 0.8-5 Hz Velocity waveforms for seven local events recorded at station WANC during the passage of the surface waves from the SAE. Thick vertical lines indicate amplitude in units of counts (values shown next to each line). The approximate UT origin times for located events are shown above each trace in bold letters. For non-located events the estimated origin times are given in gray letters.

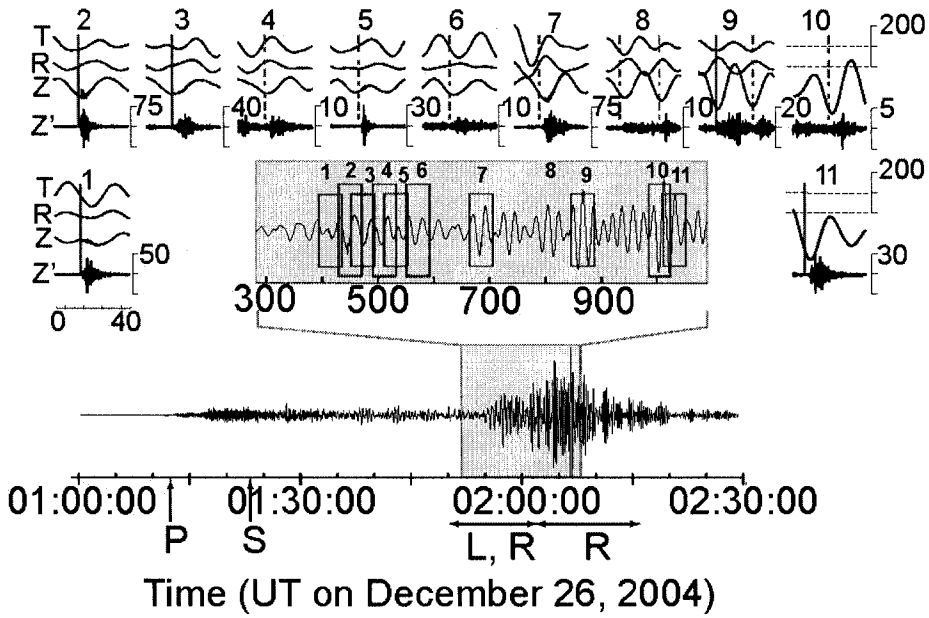

Figure A.4. Details of triggered events at Wrangell. Lower panel: High pass filtered 0.005 Hz displacement record of the SAE recorded at station WANC. Phase arrivals are labeled as P (P-waves), S (S-waves), L (Love waves), and R (Rayleigh waves). Center panel: Enhanced 15-min section of the time series showing the arrivals of Love and higher mode Rayleigh waves. Boxes numbered 1 through 11 enclose 40-s sections in which triggered events occur. Top and lateral panels: 40-s displacement time series (high pass filtered 0.005 Hz) of the horizontal components of station WACK (labeled T and R) and the vertical component of station WANC (labeled Z). Horizontal components have been rotated in the direction along the great circle path joining Wrangell volcano and the epicenter of the SAE. A band pass filtered 1-20 Hz time series for station WANC is also shown (labeled Z'). Vertical red lines indicate origin times for located events (solid line) and estimated origin times for non-located events (dashed line). Horizontal dashed lines indicate periods were no data were available. Figure kindly shared by M. West, and modified by J. Sánchez. Origin times of located events by J. Sánchez.

A.3. References

Chapman, C., 2005. The Asian tsunami in Sri Lanka: A personal experience. EOS, Vol 86, 2, pp. 13-14.

NEIC-National Earthquake Information Center World Data Center for Seismology., 2005. U.S. Geological Survey web page, *http://neic.usgs.gov/neis/bulletin/neic_slav.html.*

Park, J., Anderson, K., Lay, T., Simpson, D. 2005. Global seismographic network records the great Sumatra-Andaman Earthquake. EOS, 86, 6, pp 57.

Stein, S., Okal, E. 2005. Long period seismic moment of the 2004 Sumatra Earthquake and implications for the slip process and tsunami generation. http://www.earth.northwestern.edu/people/seth/research/sumatra2.html

Sorooshian, S., 2005. Meeting the challenges of Natural Hazards in the wake of the tsunami disaster. EOS, 86, 2, pp 14.